UC San Diego

UC San Diego Electronic Theses and Dissertations

Title

Application of Nanoscale Electrostatic Interaction, 3-D Nano-fabrication and Nano-metrology

Permalink

https://escholarship.org/uc/item/0sd6f5nk

Author

SUN, ZHELIN

Publication Date

2016

Peer reviewed|Thesis/dissertation

eScholarship.org Powered by the California Digital Library
University of California

UNIVERSTIY OF CALIFORNIA, SAN DIEGO

Application of Nanoscale Electrostatic Interaction, 3-D Nano-fabrication and Nano-metrology

A dissertation submitted in partial satisfaction of the requirements for the degree

Doctor of Philosophy

in

Electrical Engineering (Applied Physics)

by

Zhelin Sun

Committee in charge:

Professor Jie Xiang, Chair
Professor Prabhakar R. Bandaru
Professor Renkun Chen
Professor Yu-hwa Lo
Professor Yuan Taur

2016

Copyright

Zhelin Sun, 2016

All rights reserved

The Dissertation of Zhelin Sun is approved, and it is acceptable in quality and form for publication on microfilm and electronically:

_____

_____

_____

_____

_____

Chair

University of California, San Diego

2016

Dedication

To my beloved mother and father, and those all who support me till today.

- *To my mother Meizhao Liang, your everlasting love is the very reason for me to live so happily in this world.*
- *To my father Chutao Sun, your vision and dearest love always guide me, protect me, and support me through all my life and achievements.*
- *To my grandmother Fengzhen Wang, thank you for sparking my interest in studying abroad and encouraged me to enjoy the beauty of the entire world.*

Table of Contents

List of Figures

List of Abbreviations

Si, Silicon; Ni, Nickel; Au, Gold; Cr, Chrome; Ti, Titaninum; CNT, Carbon Nanotube; SiNW, Silicon Nanowire; M/NEMS, Micro/Nano-Electro-Mechanical-Systems; NEMFET, Nano-Electro-Mechanical-Field-Effect-Transistor; EBL, Electron-Beam Lithography; RIE, Reactive Ion Etch; CPD, Critical Point Drying; SEM, Scanning Electron Microscopy; AFM, Atomic Force Microscopy; DNA, deoxyribonucleic acid

Acknowledgements

First of all, I would like to express my sincerest gratitude to my advisor Prof. Jie Xiang for his invaluable guidance, support and enlightenment during all stages of my work in the past 4 years at UC San Deigo. I really feel privileged to be a member in his research group. Here, I have not only gained valuable knowledge and insights in nanoelectronics and NEMS, but also learned an enthusiastic attitude toward scientific research and the intelligent ways of logical thinking, which laid the solid foundation for my future career.

Second, I am grateful to my previous advisor Prof. Deli Wang, who kindly introduced me into the realm of nanowire research and helped me through the most difficult time. He opened up a new path of research for me and encouraged me to engage in a diverse topics of various nanostructure research.

I am also thankful to all my Ph.D. committee members, Professor Prabhakar R. Bandaru, Professor Renkun Chen, Professor Yu-hwa Lo, and Professor Yuan Taur, for taking your precious time to review and evaluate my research, as well as giving me valuable feedback to improve my thesis and showing me the brightest way forward.

Finally, I feel fortunate to work with a group of such intelligent people in both Prof. Xiang and Prof. Wang's labs. My progress and accomplishments cannot be done without your kind support and assistances.

The material in this thesis is based on the following publications

- Chapter 1, 2 and 3, in part, are a reprint of

Z. Sun, D. Wang, J. Xiang. “Self-Bridging of Vertical Silicon Nanowires and a Universal Capacitive Force Model for Spontaneous Attraction in Nanostructures,” ACS Nano, 2014, 8 (11), 11261–11267.

The dissertation author was the primary investigator and author of this paper.

- Chapter 4 and 5, in part, are a reprint of

Z. Sun, S. Kwon, J. Xiang, “Low voltage three-terminal nanoelectromechanical switches using grayscale lithography”, to be submitted.

The dissertation author was the primary investigator and author of this paper.

- Chapter 6, in part, is a reprint of

Z. Li, T. Lavergne, D. A. Malyshev, J. Zimmermann, R. Adhikary, K. Dhami. P. Ordoukhanian, Z. Sun, J. Xiang, and F. E. Romesberg. “Site-Specifically Arraying Small Molecules or Proteins on DNA Using An Expanded Genetic Alphabet,” Chem. Eur. J. 2013, 19, 14205-14209.

Vita

2008	Bachelor of Science, Applied Physics,
	Nanjing Normal University, People's Republic of China
2011	Master of Science, Physics,
	University of South Carolina, Columbia
2016	Doctor of Philosophy, Electrical Engineering
	University of California, San Diego

Publications

(1) Z. Sun, D. Wang, J. Xiang. "Self-Bridging of Vertical Silicon Nanowires and a Universal Capacitive Force Model for Spontaneous Attraction in Nanostructures," ACS Nano, 2014, 8 (11), 11261–11267.

(2) Z. Sun, S. Kwon, J. Xiang, "Low voltage three-terminal nanoelectromechanical switches using grayscale lithography", to be submitted.

(3) S. Kwon, D. Lu, Z. Sun, Z. Liu, and J. Xiang, "Highly stretchable, printable nanowire array optical polarizer" to be submitted

(4) K, Sun, S. Shen, J. S. Cheung, X. Pang, N. Park, J. Zhou, Y. Hu, Z. Sun, S. Y. Noh, C. T. Riley, P. Yu, S. Jin and D. Wang. "Si photoanode protected by a metal modified ITO layer with ultrathin NiOx for solar water oxidation," Phys. Chem. Chem. Phys., 2014, 16, 4612.

(5) S. Vishniakou, B. W. Lewis, X. Niu, A. Kargar, K. Sun, M. Kalajian, N. Park, M. Yang, Y. Jing, P. Brochu, Z. Sun, C. Li, T. Nguyen, Q. Pei, and D. Wang. "Tactile Feedback Display with Spatial and Temporal Resolutions," Scientific Reports, 2013, 3, 1-6..

(6) N. Park, K. Sun, Z. Sun, Y. Jing, and D. Wang. "High Efficiency NiO/ZnO Heterojunction UV Photodiode by Sol-Gel Processing," Journal of Materials Chemistry C, 2013, 1, 7333-7338.

(7) Y. Shu, Z. Sun and Y. Bazaliy. "Modification of the Stoner-Wohlfarth Astroid by a Spin-Polarized Current: An Exact Solution," Physical Review B 2013, 88, 054408 .

(8) Z. Li, T. Lavergne, D. A. Malyshev, J. Zimmermann, R. Adhikary, K. Dhami. P. Ordoukhanian, Z. Sun, J. Xiang, and F. E. Romesberg. "Site-Specifically Arraying Small Molecules or Proteins on DNA Using An Expanded Genetic Alphabet," Chem. Eur. J. 2013, 19, 14205-14209.

(9) K. Sun, N. Park, Z. Sun, J. Zhou, J. Wang, X. Pang, S. Shen, S. Noh, Y. Jing, S. Jin, P. Yu, and D. Wang. "Nickel Oxide Functionalized Silicon for Efficient Photo-oxidation of Water," Energy and Environmental Science, 2012, 5, 7872-7877.

(10) K. Sun, K. Madsen, P. Andersen, W. Bao, Z. Sun, and D. Wang. "Metal on metal oxide nanowire co-catalyzed Si photocathode for solar water splitting," Nanotechnology, 2012, 23, 194013.

(11) M. M. Killian, E. Villa-Aleman, Z. Sun, S. Crittenden, and C.L. Leverette. "Dependence of Surface-Enhanced Infrared Absorption (SEIRA) Enhancement and Spectral Quality on the Choice of Underlying Substrate: A Closer Look at Silver (Ag) Films Prepared by Physical Vapor Deposition (PVD)," Applied Spectroscopy, 2011, No. 3, Vol 65, 272- 283.

ABSTRACT OF THE DISSERTATION

Application of Nanoscale Electrostatic Interaction, 3-D Nano-fabrication and Nano-metrology

by

Zhelin Sun

Doctor of Philosophy in Electrical Engineering (Applied Physics)

University of California, San Diego, 2016

Professor Jie Xiang, Chair

Nanotechnology has seen great development in the past two decades, and numerous nano-devices with superior electrical/mechanical/optical performance have emerged in wide applications such as electronics, biomedicine, solar energy, and aerospace. Nanofabrication, and in particular 3-D nanostructure fabrication, has been

intensively studied for the creation of novel devices, the scaling of existing systems, and the improvement in utilities and reliabilities. However, there are quite a few challenges in nanofabrication, such as the spontaneous attractions among nanostructures. pontaneous attractions have often caused adhesion or stiction that affects a wide range f nanoscale devices, particularly nano/microelectromechanical systems. Previous explorations of the attraction mechanisms have suggested a wide range of origins but none of them is universally applicable to most nanostructures. Here a simple capacitive force model based on the nanoscale electrostatic interaction is proposed to quantitatively study this universally observed phenomenon. Our model is experimentally verified using arrays of vertical silicon nanowire pairs with varied spacing, diameter, and size differences. This work illustrates a new understanding of spontaneous attraction that will impact the design, fabrication and reliable operation of nanoscale devices and systems.

By taking advantage of the nanoscale electrostatic attraction, low voltage nano-electro-mechanical (NEM) switches are built with innovative grayscale electron-beam lithography. The main benefit of this new fabrication technique is that the essential air gaps for movable components (nano-cantilevers or nano-beams) can be generated in a straightforward one-step lithography process, without any growth or etching to traditional sacrificial layers such as dielectrics. The structural dimensions of the nano-switches, as well as switch-on (pull-in) voltages are readily controllable. The fabrication and performance for both single-cantilever nano-switches and doubly-clamped NEM devices are demonstrated.

Nano-metrology such as Scanning Electron Microscopy (SEM) and Atomic Force Microscopy (AFM) is extremely useful in the characterization of various nanostructures, and has been widely applied in our research. At the end of this thesis, one particular example using ambient condition AFM characterization of synthetic individual DNA molecule with site-specific decoration of proteins will be discussed.

Chapter 1:

Introduction

This chapter focuses on the introduction to the development of nanotechnology and current challenges in nanofabrication. A phenomenon named "spontaneous attraction" is one such obstacle that thwarts the industrialization of various nanoscale devices. Previous studies have presented different theories that explain spontaneous attraction under a number of specific circumstances. However, there is not yet a universal theory with verified experimental data that reveals the true physics behind this phenomenon. To solve this puzzle, we developed a simple capacitive force model and conducted a series of controlled experiment to prove that the origin of spontaneous attraction is the long-range electrostatic interaction caused by size variance and natural surface potential in the nanostructures.

1.1 Nanotechnology and Nanofabrication

Nanotechnology, first envisioned by physicist Richard Feynman, has seen significant development in the past two decades. Numerous novel structures with sizes below 100 nanometers are invented or discovered, and advanced into functional devices with superior mechanical, electronic, photonic and thermal properties. From carbon

nanotubes (CNTs) [9] to semiconductor nanowires [2-8], from graphene [10] to quantum dots made of metal or metal oxide particles[44], each type of nanomaterial has its unique strength and characteristics that always attract a tremendous amount of attention at its debut: including not only a thorough investigation from the scientific world, but also the vast investment from the industry and market. In addition, traditional microelectronics are scaling down to the nanoscale regime at a surprisingly fast pace. The size of the gate component in a commercial CMOS transistor has decreased to 22 nm or less[45], and the micro-electro-mechanical-systems (MEMS) that features 10-100 μm movable component are also shrinking down to nano-electro-mechanical-systems (NEMS) with structure sizes less than 100 nm. These efforts were proven to be truly worthwhile. In 2007, $147 billion worth of nanotechnology-enabled products are sold, and that number is expected to reach $1.8 trillion worth of product revenue in 2015 [46].

However, due to the unique nature of nanoscale devices, massive production of such minuscule structures always yields problems as a result of the incomplete understanding to bizarre behaviors that only occur at nanoscale, which hinder the industrialization of nanotechnology and puts a bottle neck in its path of development. For instance, spontaneous attraction among nanostructures is such a phenomenon that universally exists in many types of nanomaterials and nanostructures, but is not yet well-understood. This phenomenon not only affects the fabrication process for nano-devices based on nanowires[2-8], carbon nanotubes (CNTs)[9], graphene[10], and nanoparticles[45,47-48], but also causes performance and reliability issues during the

operation of nanorod-based photodetectors and nano/micro-electro-mechanical systems (NEMS/MEMS)[1, 11-14]. The undesirable attraction between nanostructures typically results in off-design disarrayed components with bending and bundling, malfunctions in nano-electronics, or mechanical failures in NEMS. To fight these difficulties and ensure high-yield manufacturing of nano-devices, the physics behind these phenomenon must be systematically studied to avoid fabrication failures or take advantages of these behaviors for novel applications.

In this thesis, I will demonstrate the mechanism of spontaneous attraction among nanostructures with a universal capacitive force model based on the size disparities and therefore variations in self-capacitance inherent to most fabricated nanostructures. This model is quantitatively verified with a series of systematic experiments using high-aspect-ratio silicon nanowire (SiNW) arrays as an example system. Finally, the knowledge of capacitive-force-induced attractions are applied to our original fabrication of low voltage nano-electro-mechanical switches by novel grayscale electron-beam lithography.

1.2 Spontaneous Attraction

Spontaneous attraction, also known as spontaneous adhesion or stiction[1], is a common but sometimes overlooked phenomenon among various nanostructures such as nanowires[2-8], carbon nanotubes (CNTs)[9], graphene[10] and nano/micro-electro-mechanical systems (NEMS/MEMS)[1, 11-14]. In fact, the bending, collapsing or

stiction induced during device fabrication or operation often lead to unreliability such as poor device performance and even failure. For instance, irreversible stiction is considered a major failure mode in NEMS/MEMS[14-16], and the distortion of geometrical symmetry affects electron transportation properties or optical absorption in ordered nanowire arrays[17,18].

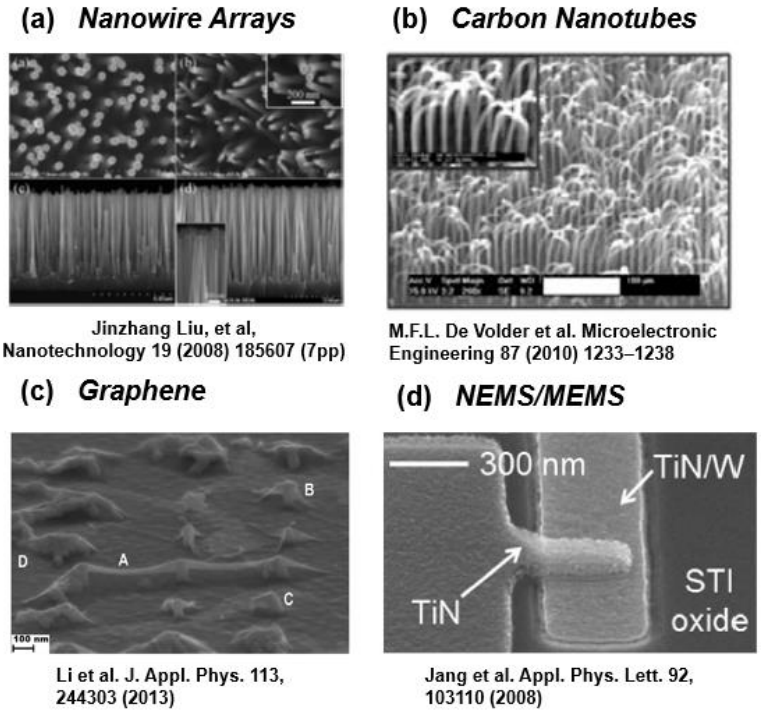

Figure 1.1: Spontaneous attraction in various nanomaterials and nanostructures [4, 9, 10, 49].

Figure 1.1 shows the Scanning Electron Microscopy (SEM) images of spontaneous attraction in a variety of nanomaterials and nanostructures [4, 9, 10, 49]. In Figure 1.1(a), the as-grown vertical ZnO nanowires attract each other near the top, and form bundling clusters instead of perfectly aligned vertical arrays. Figure 1.1(b)

shows that self-attraction among carbon nanotubes (CNTs) occurs as the aspect ratio of CNTs increases during their growth. Another type of carbon 2D nanostructures, graphene, is also observed to naturally adhere to other nanostructures such as the gold nanopillars shown in Figure 1.1(c). Finally, spontaneous adhesion, also known as stiction, is one of the major failure mode during the fabrication or operation of NEMS/MEMS switches, such as the one shown in Figure 1.1(d). As its movable active element (nano/microscale cantilevers or suspending beams) is attracted and jammed onto the substrate or contact electrodes, this adhesion is occasionally irreversible and

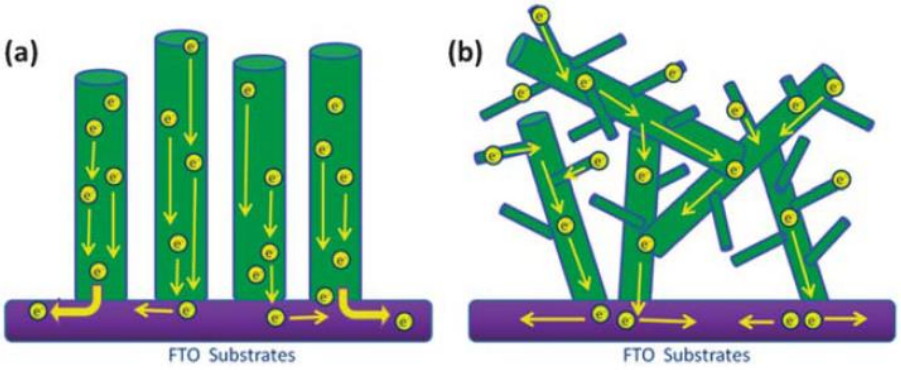

the switch will stop to work.

Figure 1.2: Schematic representation of the electron path on (a) vertically aligned and (b) bundled and branched nanorod electrodes [17].

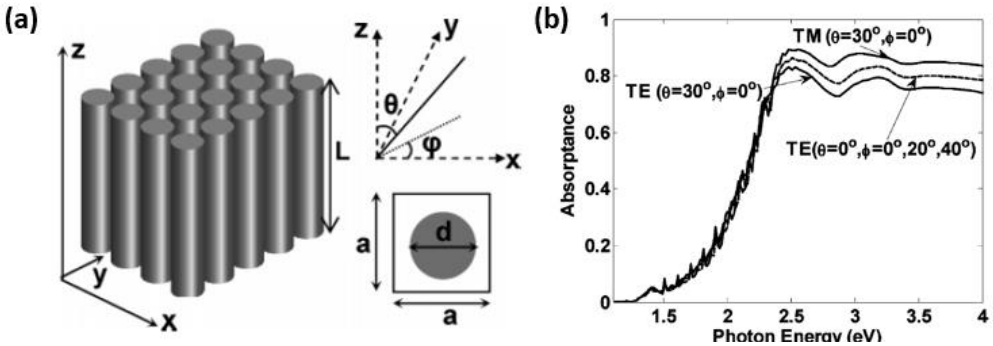

Fig. 1.3: (a) Schematic drawing of the periodic silicon nanowire structure. (b) Angular dependence of light absorptance for a nanowire in respect to incident light. [18]

Other than the impact of stiction on electro-mechanical devices, spontaneous attraction also affects many other types of nano-devices. For instance, the electron transportation in the electrochemical supercapacitors [17] based on manganese oxide nanorod arrays (Figure 1.2) will be significantly altered if the nanorods are bundled by self-attraction, resulting in a remarkable decrease in its specific capacitance. Another example in Figure 1.3 shows that the bending of silicon nanowires in photovoltaic cells [18] will lead to an overall lower light absorptance and lesser optical performance of photon-energy-conversion. Therefore, an in-depth research on the spontaneous attraction is critical to avoid fabrication or performance failures in nanoscale devices.

1.3 Previous Studies on Spontaneous Attraction

By far, we have seen that undesired spontaneous attraction usually distorts the geometrical symmetry of nanostructures and causes serious issues in device performance and reliability. Understanding the mechanism of spontaneous attraction on a quantitative level is crucial for the fabrication of nanostructures and nano-devices. Currently, despite that a good collection of theories has been proposed to explain this phenomenon, these studies give a rather diverse picture and many mechanisms are either not completely understood or only applies in special circumstances. However, spontaneous attraction seems to be a universal phenomenon for numerous types of nanomaterials in different conditions. The fundamental physics for spontaneous

attraction still remains to be explored. We will now discuss some of the previous theories and analyze this phenomenon from the existing experimental results.

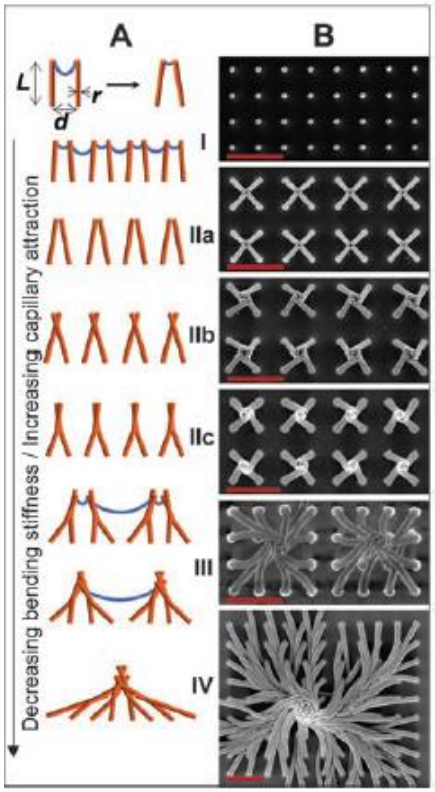

Figure 1.4: (a) Schematic diagrams and (b) corresponding SEM images showing the collapsing of nanopillars and the formation of helical patterns due to capillary force [28]

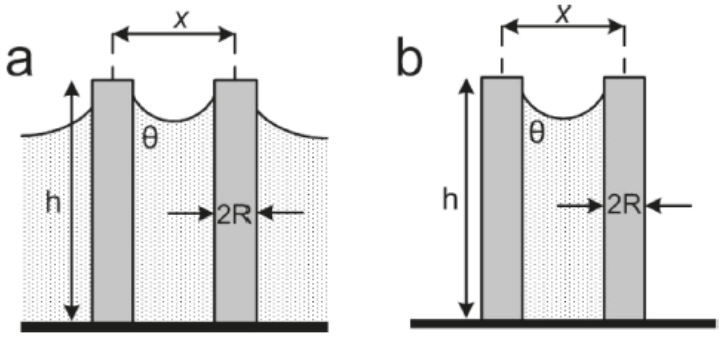

Fig. 1.5: Schematic illustrations of two nanopillars (a) partially immersed in liquid and (b) with an isolated capillary bridge between them [23]

A common explanation for spontaneous attraction during fabrication that involves humid environments [14] or aqueous processing [23, 26, 28] is the capillary force induced by liquid evaporation. Figure 1.4 presents a nice example of well-controlled bundling and collapsing of nanopillars which forms interesting helical assemblies through the evaporation of liquid among the nanostructures. To see more quantitative analysis, Figure 1.5 gives the schematics of two nanopillars (a) partially immersed in liquid or (b) with an isolated capillary bridge between them. The capillary interaction energy between two cylindrical nanopillars in Fig1. (a) is given by [23]

$$W_c = -2\pi\,\gamma\,\mathrm{R}^2\cos^2\theta\,\ln\left(\frac{l_c}{x+\sqrt{x^2-4R^2}}\right)$$

where γ is the surface tension of the liquid, $l_c = (\gamma/\rho\, g)^{1/2}$ is the capillary length of the liquid, ρ is the liquid density and g is the gravitational acceleration. Thus the capillary force between them can be derived as:

$$F_c = -\frac{dW_c}{dx} = -\frac{\pi\gamma R^2\cos^2\theta}{\sqrt{(x/2)^2-R^2}}$$

It can be seen that the capillary force depends not only on the liquid properties: surface tension γ and contact angle θ, but also on the geometry of the nanostructure: the distance between nanopillars x and radius R.

The capillary force theory serves well in explaining collapsing of nanostructures during solvent evaporation. However, spontaneous attraction is also widely observed in entirely dry environment (such as in a vacuum chamber[4,5,8]) or process that does not involve aqueous processing (such as CVD growth for nanowires or nanotubes)

[4,5,9,10]. Now the question is: what could have caused the attraction in dry environment without solvent evaporation?

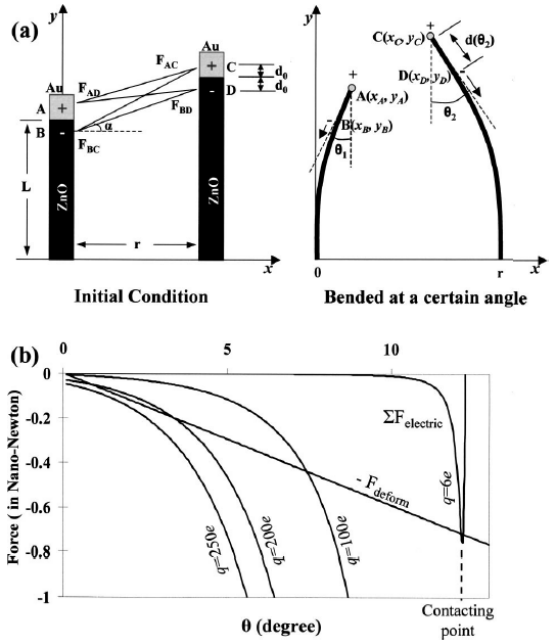

Figure 1.6: (a) Schematic model of the interaction between two ZnO nanorods. (b) The calculated electric attraction force and elastic force based on bending angle. [8]

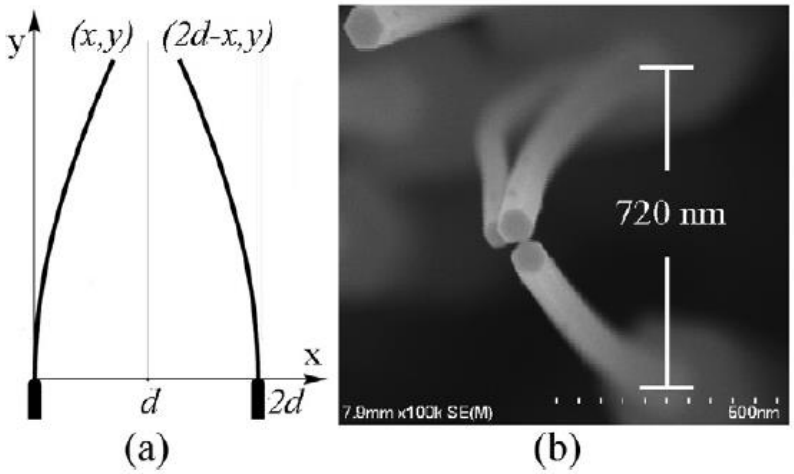

Figure 1.7: (a) Schematic of a cantilever-bending model to account for nanowire bending due to the electrostatic interaction between polar top surface, and (b) a high-magnification FE-SEM image showing a typical bending and bundling of nanowires. [4]

Early theories explaining spontaneous attraction in dry environments include dipole-dipole interaction [8] (Figure 1.6) and electrostatic forces generated by surface polar charges [4] (Figure 1.7). X. Wang et al. [8] attribute the self-attraction among Au-catalyzed ZnO nanorods to the formation of two dipoles between Au/ZnO interface on two separate nanorods. This attraction occurs inside an SEM vacuum chamber with negligible humidity. It is assumed that these nanorods are significantly different in length, and consequently a non-zero angle exists between the dipoles at nanorod tips, providing a sufficient electrostatic attraction force to bend the vertical free-standing structures. However, it is later proven that even without any dipoles from metal/semiconductor interface or any difference in nanowire length, the spontaneous bending of ZnO nanowires may also happen [4]. J. Liu et al. consider surface polar charges created by the unique wurtzite structure of ZnO nanowires to be the main reason of self-bundling among metal-free vertical ZnO nanowires. Nevertheless, self-attraction is also commonly observed on other materials such as silicon[5] (Figure 1.8) and GaAs [6] (Figure 1.9) that lack any of the above characteristics, on which the polarized surface theory will not work. Apparently the spontaneous attraction must be originating from a more universal mechanism that occurs in most nanostructures regardless of materials or fabrication methods.

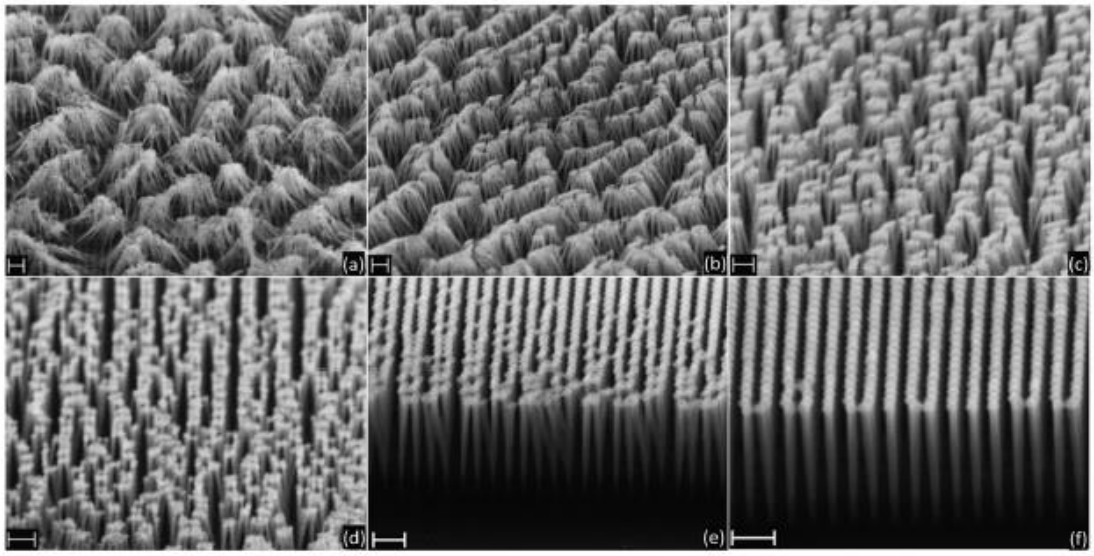

Figure 1.8: Spontaneous attraction among Si nanowires. [5]

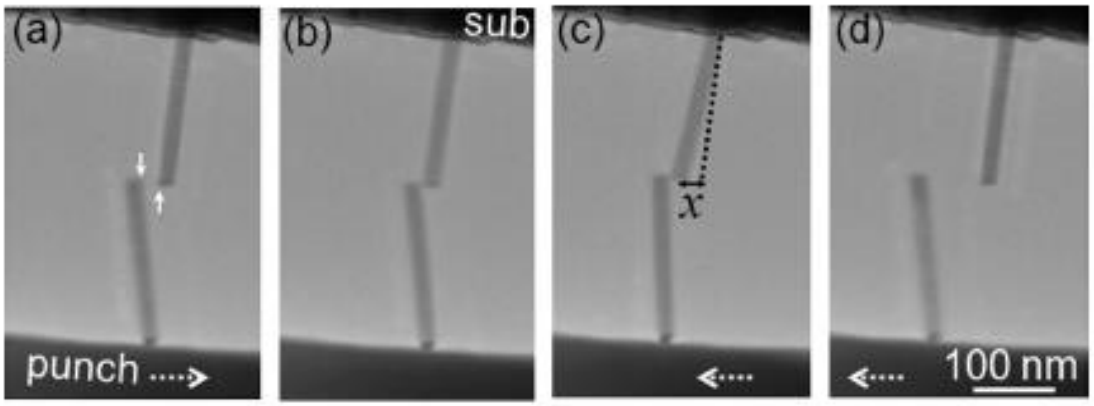

Figure 1.9: Spontaneous attraction among GaAs nanowires. [6]

More recently, researchers have turned their attention to dispersion forces (van der Waals / Casimir Forces) [5, 11-14, 19-22]. In spite of the universality of these forces and their success in explaining the short-range attraction between carbon nanotubes and graphene, the effective ranges of Van Del Waals and Casimir forces are still very limited: their magnitudes are insignificant when the nanostructures are set apart at longer distances (typically beyond 50 nm) [29]. For a common pitch size that easily exceeds

100 nm in most nano-devices, the dispersion forces cannot provide the necessary attraction to overcome the repulsive mechanical forces that holds nanostructures in place (for more details, see also the comparison between attractive dispersion forces and repulsive elastic forces in Chapter 2, Figure 2.9).

In summary, spontaneous attraction is universally seen in most kinds of nanomaterials or nanostructures, at both short and long ranges. In contrast, most current models about this phenomenon either rely on unique material properties or have limitation on the geometry of the nano-devices, and thus can only apply to each special scenario. More importantly, none of the theories has yet been supported by systematically controlled experiments and abundant supporting data. Therefore, in order to facilitate the design and fabrication for future nano-devices, it is imperative to discover the true physics behind nanostructure self-attraction with a universal experimentally-verified model.

1.4 Capacitive Electrostatic Force and Spontaneous Attraction

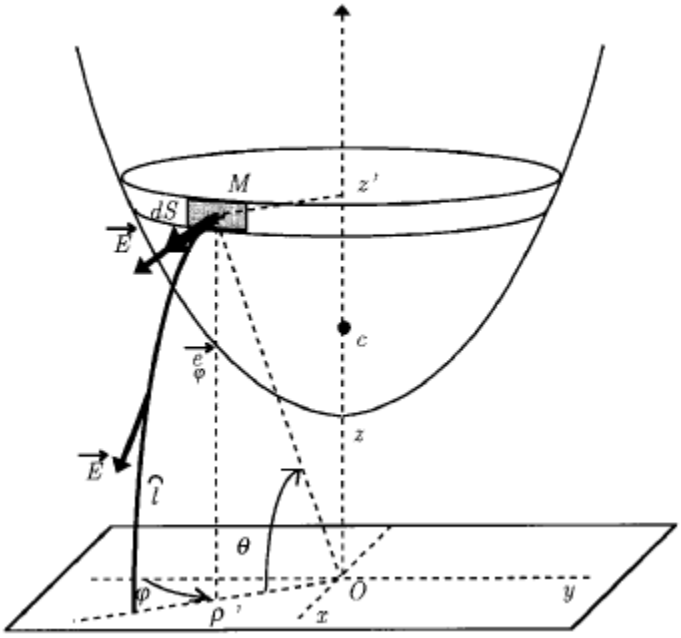

Figure 1.10: Schematic diagram of the electric field that leads to the capacitive attraction force between an AFM tip and a flat test surface [50]

Experimental evidences indicate that the spontaneous attraction among nanostructures should be a universal long-range interaction without external applied potential. Inspired by the capacitive force research in widely-applied Electrostatic Force Microscopy (EFM) [50] and Kelvin Probe Force Microscopy (KPFM) [31], we noticed that this long-range capacitive electrostatic attraction is a good candidate to explain spontaneous attraction. Due to the common existence of natural electrostatic charges on most surfaces, there usually exists a natural potential difference between objects with different geometries (and hence different capacitances). This potential difference

creates an electric field that leads to an attractive electrostatic force between objects. For example, the attractive force between the tiny atomic force microscopy (AFM) tip and a test surface (Figure 1. 10) is determined by the distribution of surface potential on each surface, which is also affected by a number of physical factors: the amount of electrostatic charges, geometry of the tip, topography of the test surface, and the tip-surface distance. Therefore, by measuring the change in this electrical attractive force, Electrostatic Force Microscopy (EFM) can accurately produces the topographical profile of the test surface, and by calculating the potential offset that creates this capacitive force, Kelvin Probe Force Microscopy (KPFM) is able to measure the work function of the surface at atomic or molecular scales.

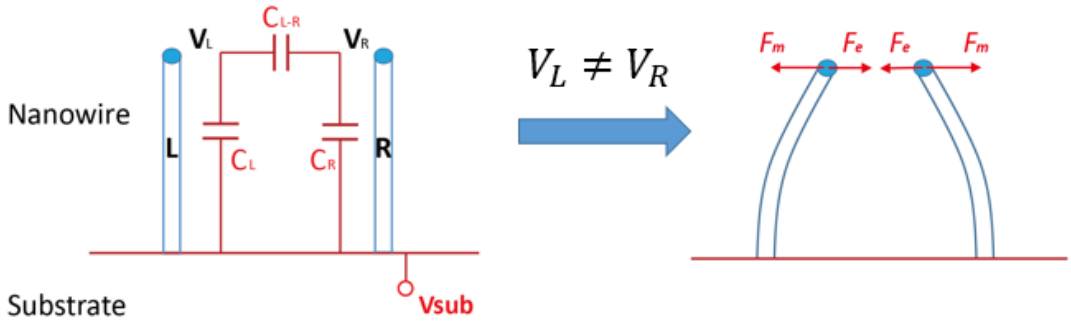

Figure 1. 11: Schematic diagram showing how the size difference (hence the capacitance difference) may lead to electrostatic attraction between two free standing vertical nanowires.

So how does this capacitive force relate to the spontaneous attraction among nanostructures? First of all, most nanostructures are capacitive and carry a distribution of natural charges, and hence, a distribution of natural surface potentials. When a pair of nanostructures does not share the exact same geometry, their capacitance are different

and therefore the distribution of surface potential will be uneven. This creates electric field lines pointing from one structure to another, producing an attractive force between them, just like the interaction between a charged AFM tip and a test surface. In other words, there will be attractive instead of repulsive forces due to the asymmetrical capacitance network in nanostructures, as long as the nanostructures are isolated from other external forces.

Take a pair of free-standing vertical nanowires (Figure 1. 11) for example, if the two nanowires are perfectly symmetrical with the same self-capacitances ($C_L = C_R$), both nanowire surfaces would have the exact same potential ($V_L = V_R$) and there will be zero electrostatic force between them. However, a small size variability caused by realistic fabrication process will render their capacitances slightly different ($C_1 \neq C_2$). Thus the symmetry in the capacitance network will be broken and $\mathrm{V}_L \neq \mathrm{V}_R$. An electrical attraction force F_e is then generated from this potential difference, and this F_e will combat the repulsive mechanical force F_m to make the nanowires bend toward each other. This is a representative scenario for free-standing nanostructures to spontaneously attract, bundle or collapse. To prove this hypothesis, more detailed analytical calculations for different geometries are to be done and a series of well-designed control experiments is required for verification.

1.5 Summary

In this thesis, we propose a universal capacitive force model based on the size variations and therefore variations in self-capacitance inherent to most fabricated nanostructures. We used high-aspect-ratio vertical silicon nanowire (SiNW) arrays as an example system and performed systematic experiments to verify our model for spontaneous attraction. The choice of vertical SiNW arrays is based on two folds: the first is the readiness to modify geometrical parameters of this nanostructure, such as spacing, diameter, length and size difference; the second is their extensive potential applications in biosensors[51], photovoltaics[18], water splitting systems[52] and NEMS[53]. In practice, although nanostructures are often surrounded by multiple structures of similar sizes, we would like to focus on two neighboring structures with the strongest interaction that will render them predominantly attracting each other and bending accordingly. This can mean, for example, two free-standing nanowires that are close to each other. Spacing, diameter, and size difference are varied for these vertically aligned nanowire pairs and revealed the threshold dimensions for causing or avoiding spontaneous attraction, which agree very well with our model.

Next, we take advantage of the capacitive forces to fabricate low-voltage nano-electro-mechanical switches with innovative gray-scale electron beam lithography. With this technique, air gaps and switch-on voltages for the nano-switches can be readily controlled without any additional growth or etching of sacrificial materials. We will demonstrate the success in making 3-terminal single-cantilever nano-swtiches, and

then introduce improved NEMS with the doubly-clamped structure. Finally, the construction and preliminary measurement on NEMFET with Ge-Si nanowires channels and suspending metal gates will be explained in the chapter 5.

1.6 Acknowledgement

Chapter 1, in part, is a reprint of Z. Sun, D. Wang, J. Xiang. "Self-Bridging of Vertical Silicon Nanowires and a Universal Capacitive Force Model for Spontaneous Attraction in Nanostructures," ACS Nano, 2014, 8 (11), 11261–11267.

Chapter 2:

Capacitive Force Model and Simulation

This chapter will demonstrate the analytical modeling and numerical simulations of capacitive force model for spontaneous attraction in nanostructures. First, we introduce the design of experiment with vertical silicon nanowire (SiNW) arrays as an example system to search for the physical parameter dependence and threshold conditions. The details and advantages for our fabrication methods (electron-beam lithography and reactive ion etching) are also discussed. Second, based on the design of experiment, schematics of capacitive force model for a pair of silicon nanowires with nickel masks are illustrated with detailed calculations for both attractive capacitive force and repulsive elastic force. The effect of each physical parameters and the critical condition for nanowire spontaneous bending are shown in the simulation for these competing forces. Furthermore, the permanent adhesion (irreversible stiction) after nanowire bridging is analyzed with the dispersion forces at very close ranges. Finally, we show that the capacitive force model can be extended to explain more generic cases of spontaneous attraction in different nanostructures, with only simple modifications to the nanostructure capacitances.

2.1 Design of Experiment

To prove the capacitive electrostatic interaction as the fundamental mechanism behind long-range spontaneous attraction among nanostructures, a series of systematical experiments must be done with a fabrication-friendly, flexible and well-controlled test system. Then it is possible to find the experimental physical thresholds of spontaneous attraction, and compare them with corresponding numerical prediction from the capacitive force model. For that purpose, high-aspect-ratio vertical silicon nanowire (SiNW) array, fabricated with electron-beam lithography (EBL) and reactive ion etching (RIE), is selected. There are two benefits for this choice: first, the high-aspect-ratio of these nanowires offers more mechanical flexibility and makes it easier to observe the spontaneous-attraction-induced bending among them; Second, the readiness to modify their geometrical parameters, such as spacing, diameter, length and size difference, makes vertical nanowires the ideal structure to set precise structural adjustments and find the critical condition of self-attraction at its physical threshold.

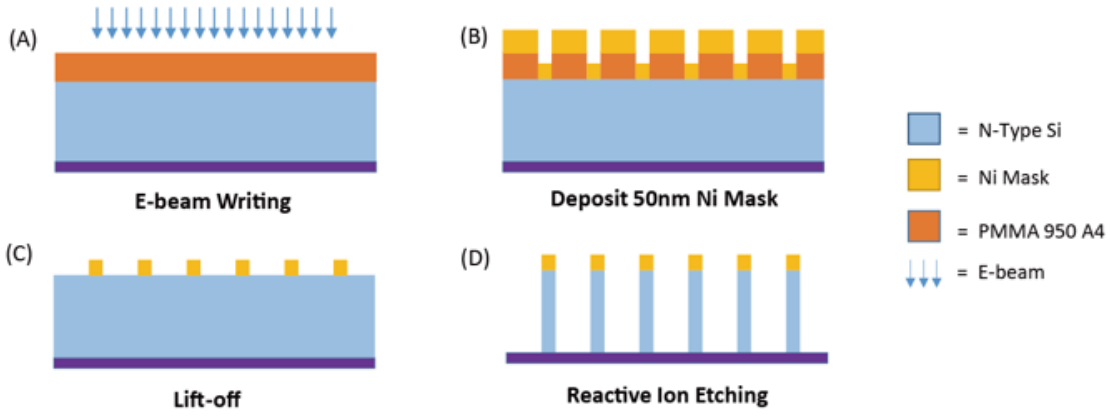

Figure 2.1: Fabrication of vertical silicon nanowire (SiNW) arrays with electron-beam lithography (EBL) and reactive ion etching (RIE)

The fabrication process of vertical aligned SiNW arrays is present in Figure 2.1. At first, electron-beam lithography (EBL) is applied to n-type silicon substrate in order to form dot patterns with precisely-controlled spacing and diameter on the surface. After 50 nm Nickel deposition with electron beam evaporator and lift-off, these as-made nickel dots will serve as protective masks during the subsequent reactive ion etching (RIE) process. Due to the very high etching selectivity between nickel and silicon (>1:400), only the silicon under nickel dots will remain after RIE, leaving free-standing vertical silicon nanowires (SiNWs) on the substrate. Notably, the pitch and size of EBL-patterned nickel dots will determine the spacing and diameter for the etched SiNWs, and the length of nanowires are controlled by the recipe and duration of RIE. The major benefit of electron-beam lithography is its ability to achieve high patterning accuracy below 5 nm, and the merit of RIE is that the nanowire length can be uniformly controlled by the etching time, and the whole progress is purely done in a completely dry vacuum chamber full of high-energy plasmas. Both fabrication methods not only grant precise control on the nanowire geometry, but also ensure that there is no capillary force involved by any aqueous processing. As a matter of fact, to completely avoid capillary effect from solvent evaporation, the nickel masks are intentionally not removed with liquid etchants, and are left on top of the nanowires.

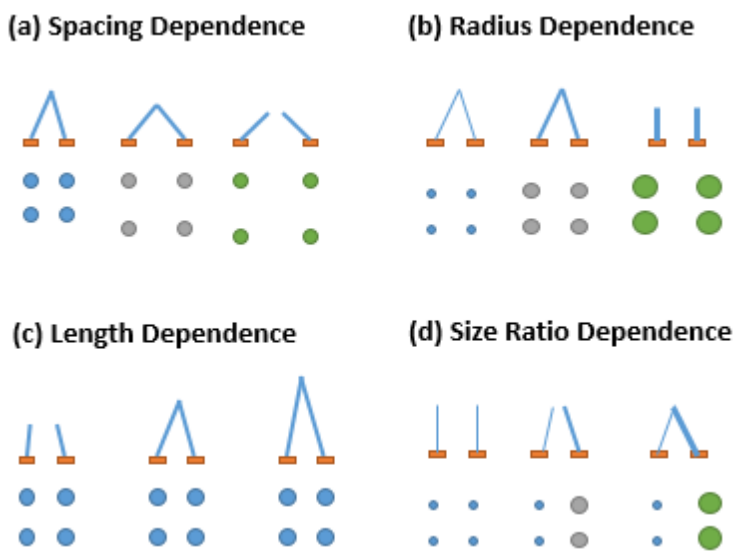

Figure 2.2: Pattern design for pairs of vertical silicon nanowire (SiNW) to find parametrical dependence on (a) spacing (b) diameter (c) length (d) size difference.

To discover the physical thresholds of spontaneous attraction on each geometrical parameter, and to minimize the interaction among adjacent structures, the nanowires are fabricated in separated pairs and put into a variety of parameter dependence tests, as shown in Figure 2.2. For instance, in the spacing dependence (Figure 2.2a), all other parameters such as radius, length and size difference are fixed for the pair of nanowires. Only the spacing between them is increased by small increments to search for the threshold condition between self-assembly and separation. There are also radius dependence and length dependence tests to identify which is the most sensitive parameter. Last but not least, since the capacitive force is anticipated to originate from the capacitance difference caused by size disparity among nanostructures, a size ratio dependence test is also prepared to verify the core of this theory.

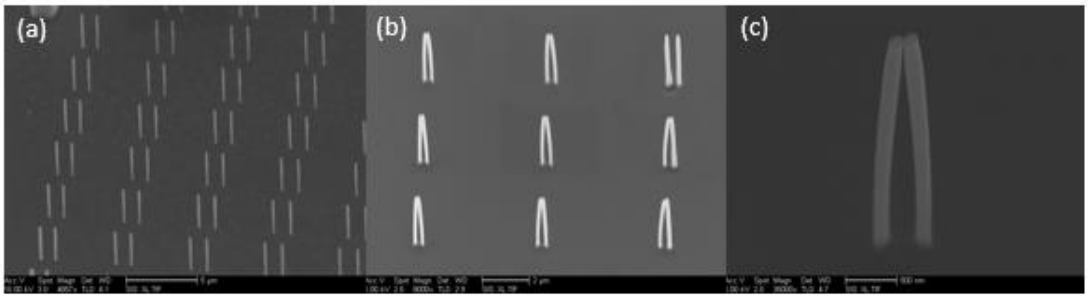

Figure 2.3: SEM images of pairs of vertical silicon nanowire (SiNW) in different configurations: (a) free standing (b) bent and attached, forming a bridging structure (c) zoom in at a pair of "bridging" nanowires.

The result of fabricated vertical SiNW pairs in various parametrical dependence tests exhibits different outcomes (Figure 2.3). For widely-spaced nanowire pairs, the attraction force is insufficient to overcome the mechanical restoration force, which leads to separated free standing nanowires (Figure 2.3a). Instead, at smaller spacing with adequate diameter, length and size ratio, nanowire pairs are observed to spontaneously bend and attach onto each other (Figure 2.3b). A closer look at one pair of the "bridging" nanowires (Figure 2.3c) indicates that the connection are formed at the top of the nanowires, or more accurately, near the junction between silicon and remaining spherical nickel mask. These evidences imply that the forces accounting for spontaneous attraction are mostly likely strongest near the top of nanowires, and are certainly sensitive to various geometrical parameters. More detailed modeling and calculations on these dependences will be discussed in the next section.

2.2 Schematics of Capacitive Force Model

Now we can use the nanowire example system to illustrate our theory. The mechanism behind the spontaneous bending of the nanowire pairs can be expressed with a simple capacitive force model, where the main source of attraction is considered to be the electrostatic interaction caused by capacitance difference between nanowires. Semiconductor and metallic nanostructures are typically anchored on a substrate which form a capacitive and resistive network between them (Figure 2.4a). The substrate carries a potential V_{sub} that originates from the natural charge distribution [31-34] . Its value and sign depend on the nature of the substrate material and the processing steps. We focus on steady state electrostatic forces and ignore all transient behaviors. We can therefore ignore equivalent resistances here for simplification because resistance values only affect transient behaviors, in other words how fast or slow the network reaches the steady state equilibrium solutions. Voltage reference (ground) is defined at very faraway that experimentally could represent the metal instrument chamber wall or a sample holder.

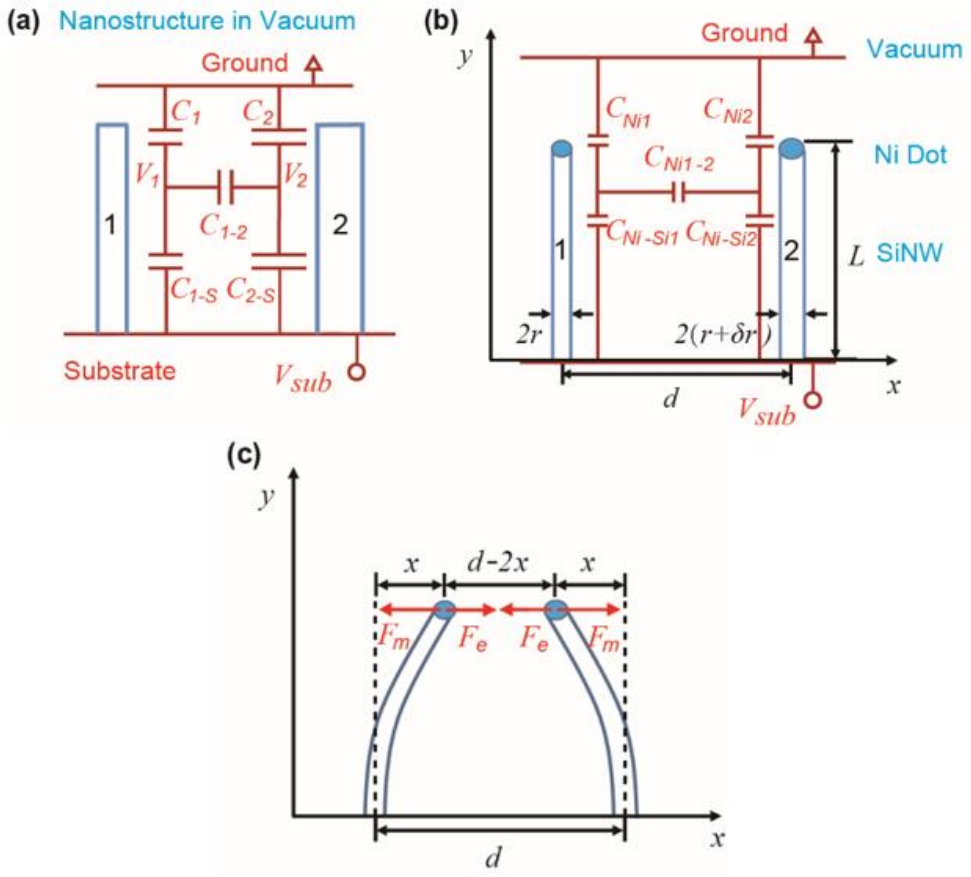

Fig. 2.4: Capacitance force model. (a) Generic circuit diagram between semiconductor nanostructures in vacuum. C_1, C_2 are self-capacitances, C_{1-S} and C_{2-S} are the capacitance between the nanostructure and substrate. C_{1-2} is the interactive capacitance between nanostructures, V_1 and V_2 are the potential on the nanostructures. (b) Capacitance force model for a pair of vertical nanowires with spacing d, radius r and length L. V_{sub} is the substrate voltage from surface charges and ground is at a faraway location from the sample, typically sample holders, instrument chambers etc. C_{Ni}, C_{Ni-Si}, and C_{Ni1-2} are the capacitances on the SiNW with Ni dots on top. r is the radius difference between the two NWs. (c) Force diagram between a pair of nanowires. F_e is the attractive capacitive force and F_m is the repulsive elastic force. x is the displacement of one of the nanowires.

In Figure 2.4a, if the pair of nanostructures are symmetrical, with same self-capacitances ($C_1 = C_2$) and equal substrate capacitances ($C_{1-S} = C_{2-S}$), the two nanowire surface would have the exact same potential and there will be zero

electrostatic force between them. However, as no nanofabrication can yield atom-to-atom precision in size variability across neighboring structures, their capacitances are typically slightly different ($C_1 \neq C_2$ and $C_{1-S} \neq C_{2-S}$), leading to a potential difference between them ($V_1 \neq V_2$), resulting in electric field lines emanating from the higher potential surface and terminating in the opposite surface. The resulting attractive electrostatic force will cause bending once it overcomes the mechanical restoration force of the nanostructures. In our experiments we use RIE-etched silicon nanowires as the test subject. The equivalent capacitive circuit for a pair of nanowires with nickel dots is shown in Figure 2.4 (b). The nickel dots served as masks during RIE process and were not removed from these SiNWs to avoid any effect from capillary force during aqueous processing. The small size variation between nanowires after fabrication leads to a difference in their capacitances, including the self-capacitance of nickel dot C_{Ni} and the Schottky junction capacitance C_{Ni-Si} between nickel dot and the n-type SiNW. Consequently, there is a potential difference δV between nanowires, creating an attractive capacitive force that leads to spontaneous bending (Figure 3c). Note that the inclusion of a Ni dot at the tip is not necessary to generate attractive forces in generic nanostructures (See section 2.6, Figure 2.10).

2.3 Capacitive Attraction Force and Elastic Restoration force

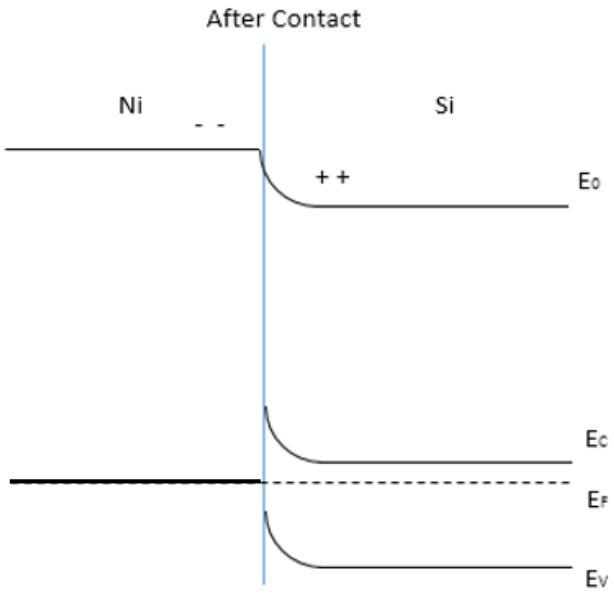

Figure 2.5: Energy-band diagram of Ni-Si Schottky junction.

With the schematics of capacitive force model given above, detailed calculations for the forces between a pair of nanowires with spacing d, radius r, radius difference δr and length L can be derived here. The nickel dot has self-capacitance $C_{\mathrm{Ni}} = 4\pi\epsilon_0 r$, where $\epsilon_0 = 8.85 \times 10^{-12}\ F/m$ is the vacuum permittivity. The Ni-Si junction capacitance can be easily calculated from standard Schottky junction model $C_{\mathrm{Ni-Si}} = C_0 \pi r^2$, where $C_0 = \epsilon / X_d$ is the capacitance per unit area, $X_d = \sqrt{2\epsilon\phi_i / qN_d}$ is the width of depletion region. The n-SiNWs in our experiments has doping concentration $N_d = 5 \times 10^{18}\ cm^{-3}$, built-in potential $\phi_i = 0.67\ eV$, and

dielectric constant $\epsilon = 11.68\epsilon_0$. $C_{\mathrm{Ni-Ni}} = 4\pi\epsilon_0 r_1 r_2/d$ is a very small capacitance between Ni dots that only takes effect when nanowires are very close. In our experimental demonstration since the substrate is electrically connected directly to the pair of nanowires by the same semiconducting Si material, the nanowire-substrate capacitances $C_{1\text{-}S}$, $C_{2\text{-}S}$ in Figure 2.4a are replaced by the Schottky junction capacitance $\mathrm{C_{Ni-Si}}$. The charges responsible for the differential potential between the two nanostructures are predominantly stored across $\mathrm{C_{Ni-Si}}$ in the Ni tips. All these capacitances are dependent on the nanowire radius *r*. Assuming there exists a radius variance δr between two nanowires, this size discrepancy will break the symmetry of capacitances and create a potential difference $\delta \mathrm{V}$ shown below:

$$\delta \mathrm{V} = \frac{\beta \cdot \mathrm{C_{Ni-Si1}} - \mathrm{C_{Ni-Si2}}}{\mathrm{C_{Ni1}} + \mathrm{C_{Ni-Si2}} + (\beta + 1)C_{\mathrm{Ni-Ni}}} \mathrm{V_{Sub}} \tag{2.1}$$

where $\beta = (C_{\mathrm{Ni2}} + C_{\mathrm{Ni-Si2}})/(C_{\mathrm{Ni1}} + C_{\mathrm{Ni-Si1}})$

The capacitive attractive force created from this potential difference is[35]:

$$F_{\mathrm{e}} = -[\,\delta \mathrm{V} \frac{r(r+\delta r)}{r + (r+\delta r)}]^2 \frac{1}{(d-2x)^2} \tag{2.2}$$

where x is the displacement of nanowire tips (Figure 2.4b). This is the attraction force that makes nanowires lean toward each other. The vertical nanowire can be modeled as a cylindrical cantilever[34], and the magnitude of this restoring force is proportional to the displacement x:

$$F_m = \frac{3\mathrm{EI}}{L^3} x = \frac{3\pi E r^4}{4L^3} x \tag{2.3}$$

where $E = 175\ GPa$ is the elastic modulus of SiNWs [36], $I = \frac{1}{4}\pi r^4$ is the area moment of inertia for cylindrical nanowires.

The nanowire pairs will begin to bend due to attraction, but whether they can bend all the way toward each other and bridge together (creating a stiction) is determined by the competition between the capacitive attractive force and the repulsive elastic force, both of which rely on various parameters of nanowires, such as spacing, radius, and their size difference. The analysis for the dependence on each parameter will be discussed in the next section with numerical simulations.

2.4 Parametric Analysis and Threshold Conditions for Spontaneous Attraction

As mentioned above, the outcome of spontaneous attraction relies on both attractive capacitive force and repulsive elastic force, whose magnitude are controlled by various physical parameters of the nanowires: spacing d, radius r, length l, radius difference δr, and the natural potential on the substrate V_{Sub}. Each parameter has its own effect on different forces. Thus, simulating the change of forces by varying one physical parameters while fixing the others can help us see how it leads to different outcomes in the nanowire bending, and find the "threshold conditions" between nanowire-bridging and non-bending for each parameter.

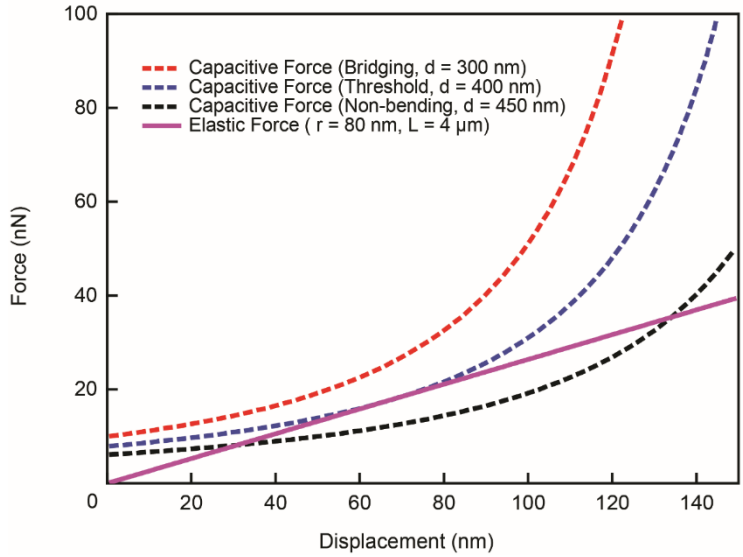

Fig. 2.6: Simulation of the competition between capacitive force and elastic force (purple solid curve) for bending (red dashed curve), threshold (blue dashed curve), and non-bending (black dashed curve) situations. The horizontal axis is the lateral displacement x of the nanowire tip. The parameters used in the simulation are $r = 80\ nm\ \delta r = 10\ nm,\ L = 4\ \mu m,\ V_{sub} = 150\ mV$.

To begin with, spacing d determines the initial capacitive force and the maximum elastic force when nanowires are permanently stuck together. The simulation in Figure 2.6 describes three different bending scenarios when only the spacing is varied. The other parameters used in the simulation are kept the same, and consistent with an actual sample fabricated for this study ($r = 80\ nm,\ L = 4\ \mu m,$ and $\delta r = 10\ nm$). In order for a nanowire to bridge or get in contact with one another, the capacitive force must overcome the elastic force at all times ($F_e > F_m$ for all $x < d$), which requires the initial spacing to be sufficiently small ($d =$ 350 nm, red curve). However, as the spacing increases to the threshold value ($d =$ 400 nm, blue curve), F_e and F_m will only intersect on a tangent at one particular displacement x_0 (stability

analysis gives $x_0 = d/3$). At this threshold, a small fluctuation in spacing or radius may result in different outcomes : bridging or non-bending. Lastly, when the spacing goes wider than the threshold ($d = 450$ nm, black curve), the capacitive force is always less than the elastic force, and spontaneous bending will not be favorable.

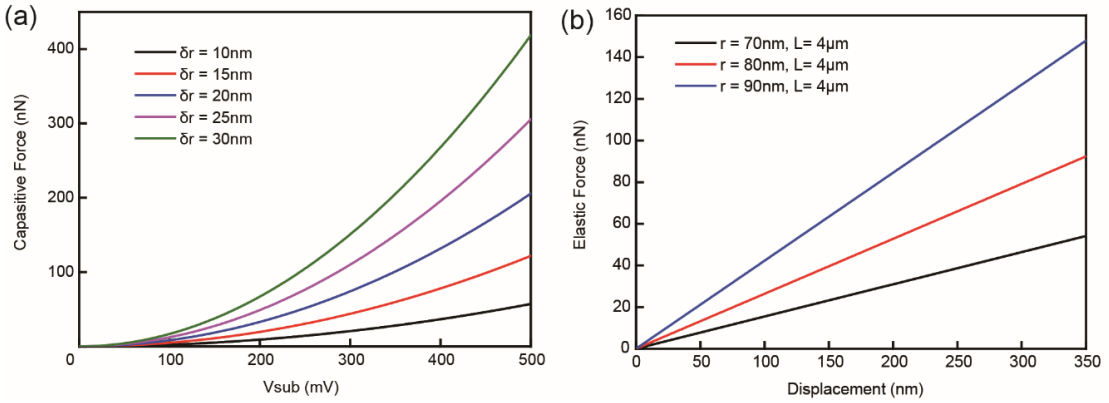

Figure 2.7: (a) Substrate voltage dependence of capacitive attraction force for varied radius difference from 10 to 30 nm. Nanowire spacing is fixed at 500 nm and radius is fixed at 80 nm. (b) Displacement dependence of elastic force for varied radii of 70 nm, 80 nm and 90 nm. For both simulations, spacing is fixed at 500nm and length is fixed at 4 μm.

Besides spacing, the significance of other parameters can also be obtained from the equations for F_e and F_m. For example, radius r affects not only various capacitances, but also has influence on the mechanical stiffness of a nanowire. Furthermore, radius difference δr and substrate voltage V_{Sub} determine the potential difference between two nanowires and thus the magnitude of the attractive force F_e. The simulation in Figure 2.7 (a)(b) shows the effect of V_{Sub}, r, and δr on both capacitive force F_e and elastic force F_m. From equation 2.2 and Figure 2.7a, it is evident that F_e increases quadratically with δV (hence substrate voltage V_{sub}) and is also very

sensitive to the radius difference δr. Compared with the elastic force F_m calculated with the same radius $r = 80\,nm$ (red curve, Figure 2.7b), it can be seen that the bending force F_{e} does not actually require a very large V_{sub} to overcome its mechanical restoring force F_m. In addition, with a very small increment in δr (ex. 5 nm), a great change is observed in the magnitude of attractive force F_{e}, resulting in completely different bending outcomes for nanowires with seemingly similar sizes. On the other hand, equation 2.3 and Figure 2.7b show that the mechanical force increases linearly with nanowire displacement x (deflection), and is most sensitive to the radius r. This is why in the experimental radius dependence test (Figure 3. 1) in the next chapter, an increment as small as 12 nm can mean the difference between bridging and non-bending, with the same spacing and length.

Notably, length l is a unique parameter that only affects the elastic force F_{m}. Since the attraction is concentrated on top of the nanowires where the major capacitances (Schottky junction capacitances) are located, the capacitive force F_{e} does not have explicit dependence on length l (eq. 2.3). It is natural that as length increases, higher aspect ratio nanowires will have less mechanical stiffness and become easier to bend. A threshold value for length between bridging and non-bending could be easily found. However, due to the limitation in our equipment, in actual experiments it is very difficult to vary only the length by increasing RIE process time while keeping other parameters such as nanowire radius and radius difference fixed. As the etching time goes up, the size of remaining nickel mask decreases, making the radius of the nanowire beneath it smaller than those etched with shorter length. Consequently, in order to apply

strict variable control in all test experiments, we fixed most nanowire length to be around 4 μm and focused on the effect of other parameters such as spacing, radius, size difference and substrate voltage.

2.5 Nanowire Bridging (Irreversible Stiction) and Dispersion Forces at Close Proximity

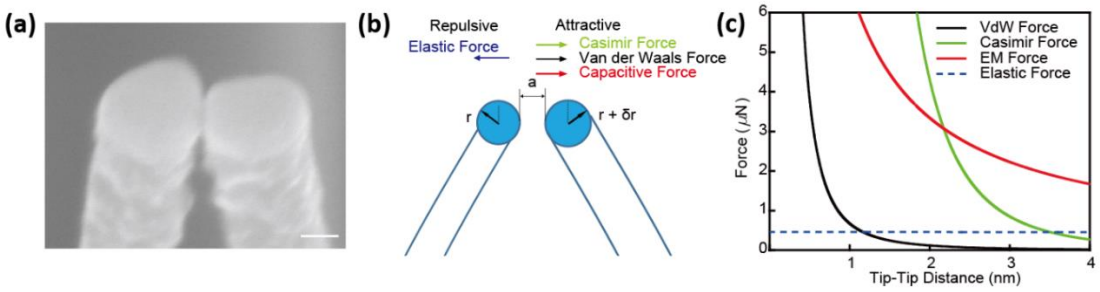

Figure 2.8: (a) SEM image showing the contacting tips of two bridging nanowires. The scale bar is 50 nm. (b) Schematics for nanowires bridging (adhesion) at close proximity. The tip-tip distance is 'a', the radius for the left nanowire is 'r', and a radius difference 'δr' exists between the nanowires. All forces are shown with different colors and their directions are present. (c) Simulation for Van der Waals force (black solid curve), Casimir force (green solid curve), capacitive force (red solid curve) and elastic force (blue dashed curve) at close tip-tip distance $a = 0 \sim 4$ nm, for nanowires with spacing $d = 500$ nm, radius $r = 80$nm, radius difference $\delta r = 8.7$ nm, length $L = 4$ μm and substrate voltage $Vsub = 150$mV.

It is widely observed in experiments that once nanowires bridge and make contacts, the adhesion between them is usually very strong and permanent. Figure 2.8a is such an SEM image showing two nanowire tips stuck together after bridging. When nanowires are bridged, the attractive capacitive force will vanish due to the redistribution of charges and can no longer account for the stiction. However, most

nanowires are still permanently connected due to adhesion caused by several short-ranged dispersion forces such as Van der Waals force and Casimir Force. The detailed analysis and calculations for this adhesion are given below.

Figure 2.8b is the force diagram showing all four types of forces acting on two nanowire tips with radius r and $r + \delta r$, separated by a very small distance a. There are three attractive forces (capacitive force, Van der Waals force and Casimir Force) and one repulsive force (elastic force) that tries to restore the nanowire to vertical free-standing status. For two nanowires with a spherical nickel tip and a cylindrical silicon body, the Van der Waals force F_{vdW} is calculated to be [42]

$$F_{\mathrm{vdW}} = -\frac{Al\sqrt{\frac{r(r+\delta r)}{r+(r+\delta r)}}}{16(a)^{5/2}} + \frac{A}{6}\frac{r(r+\delta r)}{a^2} \tag{2.4}$$

The other attractive Casimir force F_c is approximately [43]

$$F_c = -\frac{\pi^2 \hbar c}{240 a^4}\pi\frac{r(r+\delta r)}{r+(r+\delta r)} \tag{2.5}$$

For the capacitive force, before the nanowires actually touches and vanishes, it takes a modified form at close range

$$F_{\mathrm{e}} = -\frac{1}{4}(\delta \mathrm{V})^2\frac{r(r+\mathrm{dr})}{r+(r+\mathrm{dr})}\frac{1}{a} \tag{2.6}$$

Finally the repulsive or restoration elastic force for nanowires with spacing d, and length L is:

$$F_m = \frac{3\pi E r^4}{4L^3}\frac{(d-a)}{2} \tag{2.7}$$

The simulation of all four forces discussed above is present in Figure 2.8c for a pair of nanowire tips at close range ($a = 0 \sim 4$ nm). At this extreme proximity, both Casimir force F_c and Van der Waals force F_{vdW} grows quickly when the distance decreases, and start to dominate over the elastic force at $a = 3.5$ nm and $a = 1.25$ nm respectively. Therefore, even if the capacitive force F_{e} vanished after contact, the overall attraction force can be much larger than the repulsive elastic force at close range ($F_{\mathrm{vdW}} + F_{\mathrm{Casimir}} > F_{\mathrm{elastic}}$), which leads to the permanent stiction.

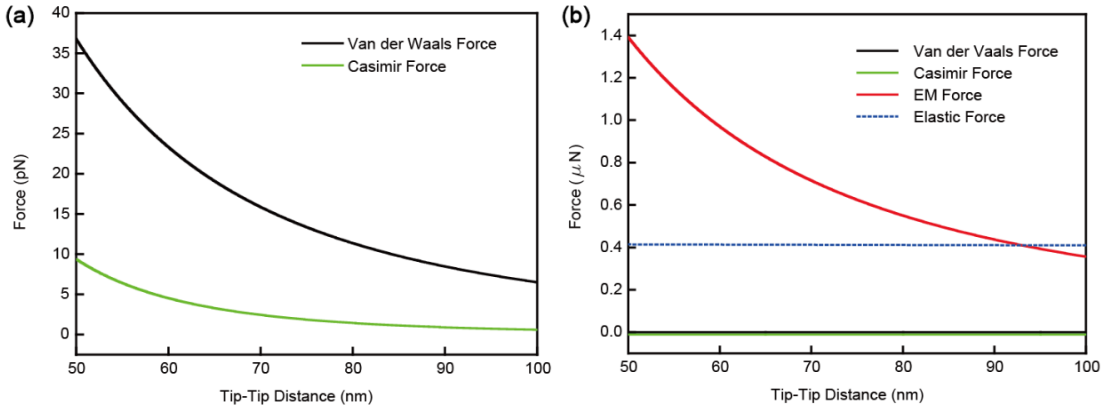

Figure 2.9: (a) Simulations for Van der Waals force (black solid curve) and Casimir force (green solid curve) at long tip-tip distance $a = 50$ to 100 nm (b) Comparison between all forces. Van der Waals force (black solid curve), Casimir force (green solid curve), capacitive force (red solid curve) and elastic force (blue dashed curve) at large tip-tip distance $a = 50$ to 100 nm, for nanowires with spacing $d = 500$ nm, radius $r = 130$nm, radius difference $\delta r = 8.7$ nm, length $L = 4$ μm and substrate voltage $V_{sub} = 150\ mV$.

However, although the dispersion forces are significant at very close range, they still cannot explain the commonly observed long range (>50 nm) spontaneous attraction because their force magnitude are negligible at this distance. As shown in Figure 2.8, at longer ranges that exceeds 50 nm (typical initial spacing between the nanowire tips),

the Van der Waals and Casimir forces diminish dramatically to the scale of pico-Newton and are too small compared to that of elastic force or capacitive force at micro-Newton level. As a result, the long-range capacitive attraction force is considered to be the fundamental reason for spontaneous bending among nanowires in our study.

2.6 Spontaneous Attraction among Nanowires on an Insulating Substrate without Metal Clusters

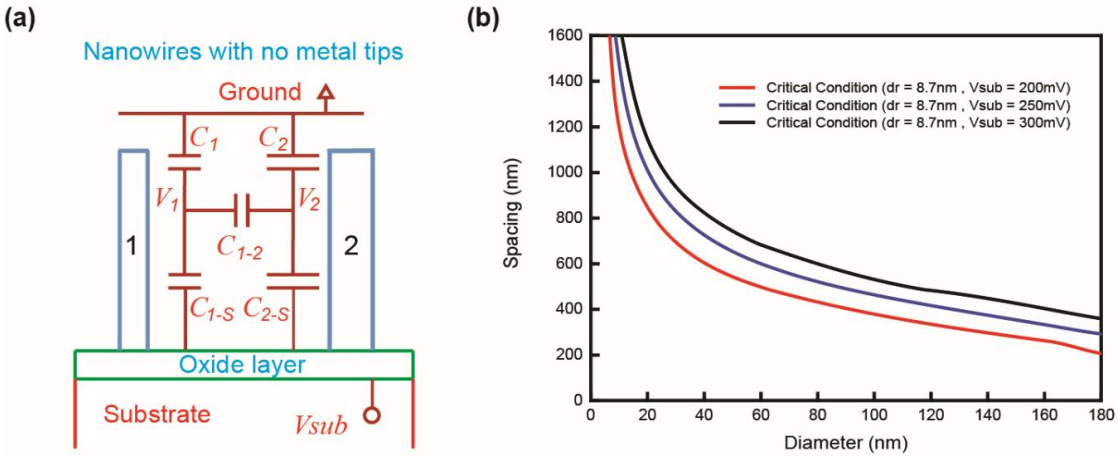

Figure 2.10: Model and simulation for spontaneous attraction between a pair of silicon nanowires on 100 nm thick SiO_2 layer without metal tips. (a) A generic circuit diagram between nanostructures. (b) Simulation result of NW bridging critical conditions. NWs with dimensions under the curve are expected to spontaneously bend. The simulation for critical condition curves are done with radius $r = 80$ nm, radius difference $\delta r = 8.7$ nm, length $L = 4$ μm, and substrate voltage $V_{sub} = 200/250/300\, mV$.

In more generic cases, the nanowires are grown on an insulating substrate, such as oxide layers, without any metal clusters on top. Our capacitive force model also works in explaining the spontaneous attraction phenomenon in such situations, with

only simple modifications to the capacitances (Figure 2.10a). The capacitances responsible for generating potential/charge difference between nanowires are changed as the following: self-capacitance of nanowire $C_1=(8+4.1(L/r)^{0.76})\epsilon\, r$, $C_2=(8+4.1(L/r)^{0.76})\epsilon(r+\delta r)$, mutual nanowire capacitance $C_{1-2}=2\,\pi\,\epsilon_0\frac{L}{\mathrm{Ln}[d^2/r(r+\delta r)]}$, and nanowire-substrate capacitance through the oxide layer $C_{1-S}=\epsilon\,\pi\,r^2/t$, $C_{2-S}=\epsilon\,\pi\,(r+\delta r)^2/t$. By applying the same equations and conditions as discussed in chapter 2.4, we produce a simulation of critical bending conditions for these nanowires without metal tips, and discovered that nanowire spontaneous bending will happen with just a small radius difference $\delta r = 8.7$ nm and an arbitrarily assumed substrate potential $V_{\mathrm{sub}} = 200\mathrm{mV}$.

2.7 Conclusion

Through detailed calculations and simulations with the capacitive force model, we successfully analyzes the fundamental mechanism for nanostructures to bend, bundle or collapse at long distance, and demonstrated the origin for permanent adhesion (stiction) at extreme proximity. By using the vertical silicon nanowire arrays as an example system, the sensitivity on various physical parameters, as well as the threshold conditions of spontaneous attraction, are revealed. It is remarkable that with just a very slight size variance in nanostructures and a reasonable amount of natural surface potential, the generated electrostatic attraction force is sufficient to overcome elastic mechanical resistance and deform the nanostructures. Finally, we show that the

capacitive model can be universally applied to other nanostructures with the exact physics principle and some simple modifications to the expressions of nanostructure capacitances.

2.8 Acknowledgement

Chapter 2, in part, is a reprint of Z. Sun, D. Wang, J. Xiang. “Self-Bridging of Vertical Silicon Nanowires and a Universal Capacitive Force Model for Spontaneous Attraction in Nanostructures,” ACS Nano, 2014, 8 (11), 11261–11267.

Chapter 3:

Experimental Study on Spontaneous Attraction

3.1 Fabrication of Vertical Silicon Nanowire Test System

A solid theory must be verified with scientifically designed experiments. To prove that the capacitive electrostatic force is the fundamental mechanism for spontaneous attraction in nanostructures, we used the vertical silicon nanowire (SiNWs) arrays as an example system, and adjusted various physical parameters for these nanowires to find their individual influence as well as their threshold values for this phenomenon. In Chapter 2.1, we have introduced the design of the experiments. Now it is time to clarify the detailed assembly methods of these SiNWs. Overall, the vertically aligned silicon nanowires, in pairs, are created with electron-beam lithography (EBL) and reactive ion etching (RIE) in order to precisely control their spacing, radius, length and radius difference. First, n-type silicon substrates (100) are cleaned with acetone, isopropyl alcohol (IPA), and DI water for 5 min with sonication. 200 nm thick methyl methacrylate (MMA) layer and 200 nm thick Polymethyl methacrylate (PMMA) e-beam resist layer are deposited on silicon wafer by spin-coating and baked on a hot plate at 180 ˚C for 90 s and 120 s, respectively. Next, metal (nickel) dot arrays with various spacing and diameter are patterned on the silicon wafers by JEOL 6400 SEM/NPGS e-

beam lithography system as RIE masks to fabricate nanowires. The pattern produces a gradual variation in nanowire spacing with an increment of 50 nm between each group. Different diameters are attained with increasing dosages under 30 kV e-beam exposure. The patterned film was developed in a 3:1 mixed solution of isopropyl alcohol (IPA) and methyl isobutyl ketone (MIBK) for 120 s. Afterwards, nickel thin film with 50 nm thickness is deposited onto the wafers by Themescal BJD 1800 E-beam evaporator. In the lift-off process, PMMA and MMA are removed with acetone, leaving the patterned nickel nano-dots on top as metal masks for the following RIE. RIE process is done using an Oxford Plasmalab 100 RIE/ICP chamber with a mixed gas of SF_6 and C_4F_8. Vertically aligned SiNW arrays are formed after the unmasked silicon being etched away. Finally, the bending and bridging of SiNW arrays are studied with a high-resolution scanning electron microscope (FEI SFEG UHR SEM) to identify the parametrical thresholds of spontaneous attraction.

3.2 Physical Parameter Dependence in Experiments

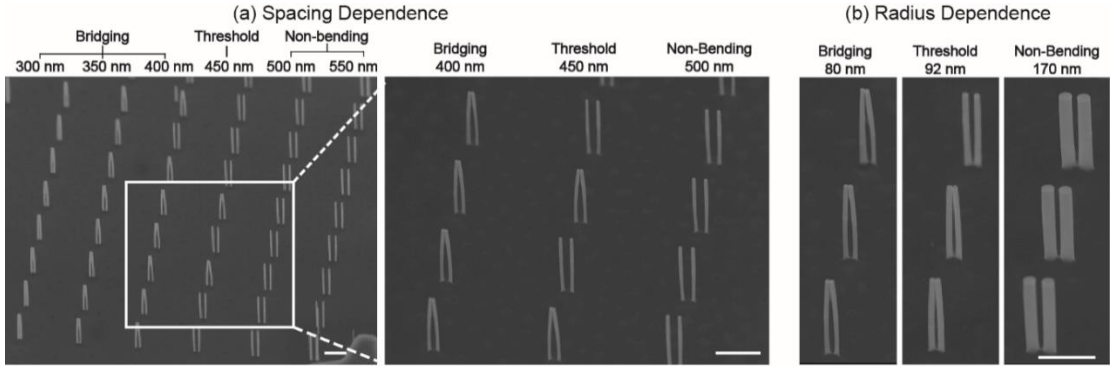

Fig. 3.1: SEM images with 30º tilt angle, showing various parameter dependence of nanowire spontaneous attraction. All Scale bars are 2 μm. (a) Spacing dependence. From left to right, the center-to-center spacing between a pair of nanowires increases from 300 nm to 550 nm, with 50 nm increment in each column. All nanowires have radius of 160 nm and length of 4 μm (b) Radius dependence. All nanowires have the same spacing of 350 nm and the same length of 4 μm. The nanowires radii are 80 nm, 92 nm, and 170 nm, respectively.

In Chapter 2, we discussed the effects of various physical parameters such as nanowire spacing, radius, length and size difference, and simulated the critical conditions of nanowire bending when adjusting the value of each factor. Now these the theoretical predictions are compared with experimental data. We first evaluated the spacing dependence of spontaneous nanowire attraction. In the SEM images in Figure 3.1a, all nanowires are fabricated with length of 4 μm and radius of 80 nm, and a radius standard deviation of +/- 8.7 nm. From left to right, the spacing between nanowire pairs increases from 300 nm to 550 nm with an increment of 50 nm for each column. We found all the nanowires with spacing $d \leq 350$ nm are bent and stuck in pairs, forming a nanowire-bridge structure. Some nanowires at $d = 400 - 450$ nm appear separated; while they all become completely separated or non-bending at $d \geq 500$ nm. To

quantify our observations, a column with more than 80% of bridging nanowire pairs is defined as a "bridging column". Likewise, a "threshold column" means there are 20%-80% bridging nanowires, and a "non-bending column" has most NW pairs separated (more than 80%). The threshold value in this particular test is found between $d = 400 - 450$ nm, which is very close to the theoretical threshold $d = 400$ nm with our model (Figure 2). It is clear that the spontaneous bending favors smaller spacing since the capacitive attractive force drops quadratically over distance.

Notice that once the nanowires bend and form a bridge, the junction will not be easily broken due to the strong attraction caused by dispersion forces (Van Der Waals force/Casimir Force) at extremely small distance. However, the long range attraction that brings nanowires together is dominated by the capacitive force, because the magnitude of these short-ranged forces are negligible compared with the elastic force at initial nanowire spacing of several hundreds of nanometers (for details see Chapter 2, Figure 2.8, Figure 2.9).

The second set of experiments examines the effect of different radius on nanowire spontaneous bending. Spacing and length of nanowires are fixed at 350 nm and 4 μm, respectively (Figure 3.1b), while the radius varies from 80 nm to 170 nm. We define radius as measured across the center of the nanowires since our simulation (see Section 3.6, Figure 3.8) has shown that even in the case of non-uniform nanowire diameters or tapered wires, the threshold calculated for electrostatic bending is well approximated with a uniform wire with the center or average radius. The threshold value for radius is found at 92 nm where non-bending nanowires begin to show up. In

our model, radius *r* plays a significant role in determining not only the capacitances on a nanowire, but also its mechanical stiffness. Both capacitive and elastic forces show very strong dependence on radius in equations (2.2) and (2.3). Notably, in Figure 3.1b a small change of average radius of 12 nm is enough to bring completely different fate in bridging or non-bending.

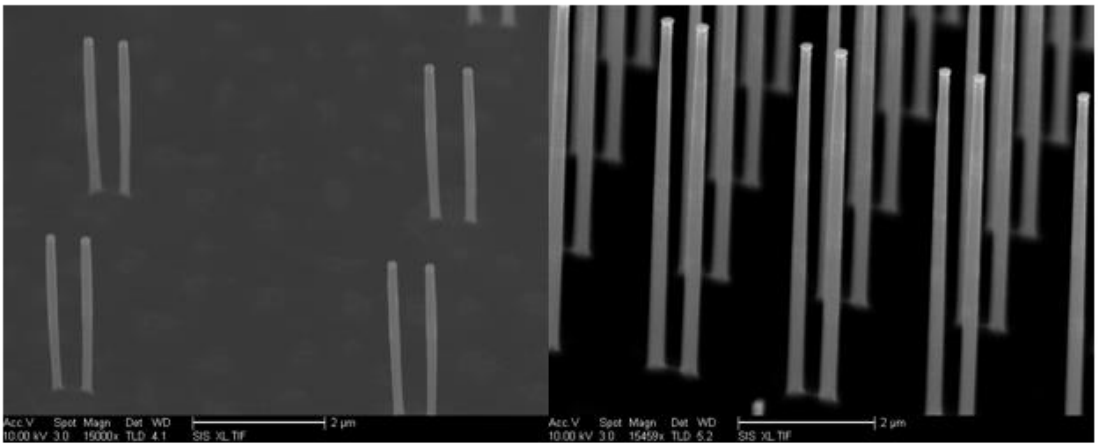

Figure 3.2: SEM images with 30º tilt angle, showing the effect of increasing length on nanowire spontaneous attraction. All Scale bars are 2 μm. All nanowires have the same spacing of 500 nm and the similar radius around 80 nm. Length has increased from (a) 3.2 μm to (b) 7.3μm. Spontaneous bending was not observed even with a 228% increment in length.

As discussed in Chapter 2.4, the length is a factor that only affects the nanowire mechanical stiffness, but has no significant influence on the capacitive attraction forces, because most of the electrostatic charges are concentrated at the Ni-Si Schottky junction near the top of nanowires and are irrelevant to length. It is also observed that although length can be easily varied with different etching time in RIE process, longer etching time usually results in the diminishing of nickel mask dots, leading to subsequently

smaller nanowire radius. The non-uniformity of average nanowire radius is undesirable for the variable control experiments. Thus we unified most nanowire length to 4um with approximately 10min of RIE etching.

Nonetheless, a tentative experiment on nanowire length dependence is done (Figure 3.2). The nanowires in this test are fabricated with the same spacing of 500 nm and the similar radius around 80 nm, while the length increases from 3.2 μm to 7.3μm. The radius of nanowires in Figure 3.2b was made close to 80 nm by using slightly bigger nickel masks and etching for longer periods. The geometrical parameters of nanowires in Figure 3.2a are carefully designed to be near the bending threshold. However, even with a 228% increment in length, the nanowires are still free standing and separated, with no bridging phenomenon detected. The fact that the longer nanowires does not bend could be attributed to the higher mechanical stiffness caused by its slightly larger radius, or the fact that the size of nickel masks on top are reduced by over-etching, which produces reduced Ni-Si Schottky capacitances and thus weaker capacitive forces to attract the nanowires.

3.3 Size-Variance-Induced Spontaneous Attraction

The key consideration in our model for spontaneous adhesion or stiction due to capacitive electrostatic attractions is the inevitable size variations between nanostructures. We can test the hypothesis using pairs of nanowires with fixed radius and spacing, but varying degree of radius difference δr. If δr is zero, there is zero

capacitive force and no bending will occur. A threshold minimum δr can be calculated from the equations in Chapter 2. Nanowire bridging would be favored if the actual experimental radius difference exceeds that δr. A pair with very small δr will have much smaller attractive forces and will not bridge whereas a pair with the same dimensions but a larger variation δr will bridge instead. The threshold δr can be easily calculated from our model.

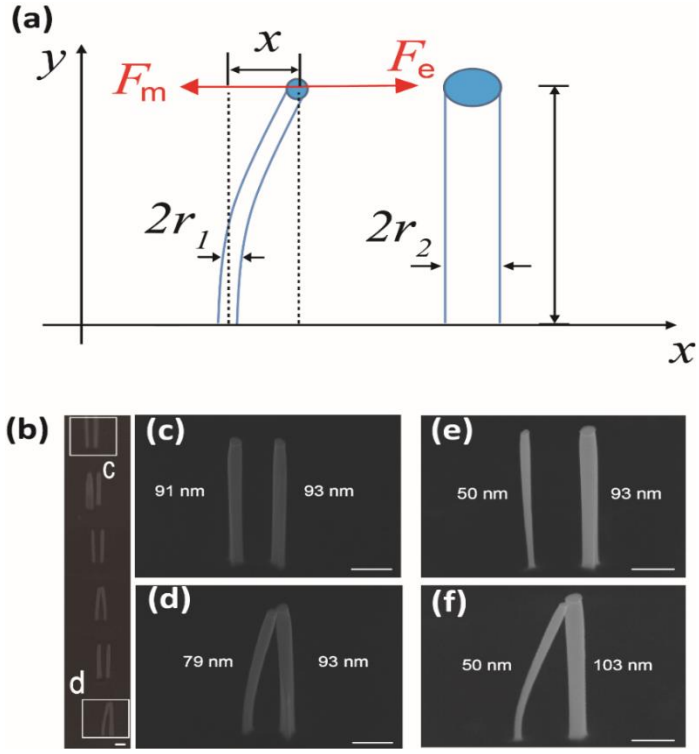

Fig 3.3: Asymmetrical nanowire bending/bridging of nanowires with different radius. (a) Schematics for nanowire attraction and asymmetrical bending. SEM images of asymmetrical SiNW pair bending/bridging. (b, c, d) SEM image showing the nanowires with same spacing of 560 nm and length of 3.4 μm in a "threshold column". Bending is favored for larger radius difference. (e, f) Two pairs of nanowires with larger size difference, same spacing of 660 nm and length of 3.5 μm. The different radii are clearly marked on the images. All SEM images are at 30º tilted angle. All scale bars are 500 nm.

Additional experiments on size difference dependence are done with intentionally fabricated asymmetrical nanowire pairs (Figure 3.3). Our model states that the attraction between nanowires originates from capacitance difference caused by their size variance. Thus a larger size difference should produce a greater capacitive force that favors spontaneous bending. In contrast, nanowires with similar sizes lack the required attraction force to bend and should remain vertical. This prediction is confirmed experimentally as shown in Figure 3.3b-e. On the one hand, a controlled experiment in Figure 3.3 (e)(f) compares two nanowire pairs carefully designed and fabricated with the same spacing $d = 660$ nm , same length $L = 3.5\ \mu m$, but different ratios of radii (r_1/r_2). The radius of the thinner nanowires is strictly controlled at the same 50 nm, to ensure the same mechanical properties (elastic force), whereas the thicker nanowires are 93 nm to 103 nm in radius, giving the ratio of radii of 1.96 and 2.06 for each nanowire pair correspondingly. It can be seen that larger size difference indeed favors nanowire bridging/bending, which is consistent with the prediction of our model.

The variation of the attractive force F_e based on δr also explains why in the threshold column some nanowire pairs are beginning to bridge while the others remain non-bending. A careful inspection on the nanowires from a "threshold column" (Figure 3.1b) indicate that that here the non-bending nanowire pairs have smaller radius difference (2 nm, Figure 4c) than the bridging ones (24 nm, Figure 4d), despite having the same spacing $d = 560$ nm, length $L = 3.4\ \mu m$ and intended radius of 93 nm. This difference in δr likely comes from size variances in the patterned Ni dot mask sizes

during e-beam lithography runs. Therefore the threshold column best illustrates how fabrication variations, under certain conditions, may lead to dramatically different fates in terms of spontaneous adhesion that ultimately may give rise to detrimental results.

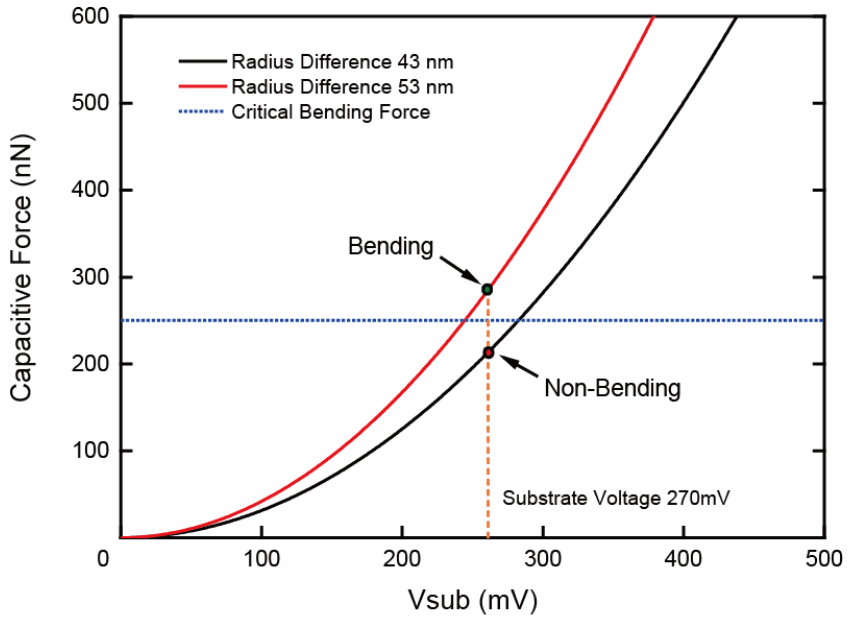

Figure 3.4: Simulation of capacitive forces for the nanowires shown in Figure 3.3 (e,f).

With our capacitive force model, the simulation result for both sets of nanowires in Figure 3.3(e,f) also agrees with the actual outcomes in experiments. The solid black curve stands for the capacitive force of nanowires in Figure 3.3e, with smaller radius difference 43 nm; and the solid red curve represents the other pair in Figure 3.3f with larger radius difference 53 nm. In order for the smaller nanowire (fixed radius $r_1 = 50\ nm$) to bend and attach to the larger one, the capacitive force between them must be greater than the critical bending force shown by the blue dotted line (the critical bending force is the elastic force at displacement equals to 1/3 of the initial spacing, $x = \frac{1}{3}\ d =$

220 nm). In other words, with the same distribution of natural electrostatic charges (hence a certain substrate voltage), the blue line draws a boundary between bridging and non-bending. It can be seen from Figure 3.4 that, with a substrate voltage around 270mV, spontaneous bending indeed favors the nanowire pair with larger size variance (Figure 3.3f) and the pair with smaller radius difference (Figure 3.3e) should result in non-bending. This simulation represents exactly what happened in experiments.

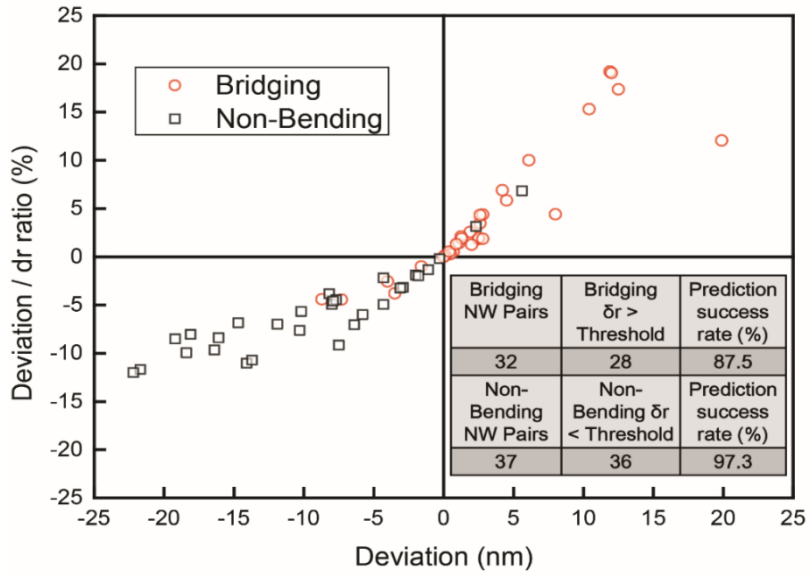

Bridging NW Pairs	Bridging δr > Threshold	Prediction success rate (%)
32	28	87.5
Non-Bending NW Pairs	Non-Bending δr < Threshold	Prediction success rate (%)
37	36	97.3

Fig. 3.5: Study on radius difference dependence with comparison between experimental data and simulation results. δr is the experimental value of radius difference between each pair of nanowires. The deviation of the experimental δr from the calculated threshold δr is shown in the horizontal axis; the ratio between deviation and experimental δr is shown in the vertical axis. Theoretically, positive deviation ($\delta r >$ Threshold) leads to bridging and negative deviation ($\delta r <$ Threshold) leads to non-bending. The actual bending status for each experimental data point is indicated by different colors: red dot for bending nanowires and black squares for non-bending nanowires. Inset table shows a summary of the number of samples and statistical percentage that follow theoretical description.

Finally, we carefully evaluated experimental radius differences from all samples and compared with their individually calculated threshold in Figure 3.5. The data from experimentally bridging nanowires are shown with red dots and the non-bending ones are shown with black squares. Notably, most bridging nanowires (87.5 % of 32 bridging pairs) indeed have size difference larger than threshold and the majority of non-bending nanowires (97.3 % of 37 non-bending pairs) also follows the model because their size difference is smaller than the threshold. The consistency between the experimental data and the model prediction in both Figure 3.4 and Figure 3.5 strongly suggests that the principle mechanism for spontaneous attraction is the capacitive force induced by size variations in nanostructures.

3.4 Comparison between Experimental Data and Simulation

To summarize these experiments, we plot in Figure 3.6 all experimental data points collected, categorized into three groups: red hollow circles, blue solid triangles and black hollow squares represents nanowire pairs in the bridging columns, threshold columns and non-bending columns, respectively. Similar to the simulation in Chapter 2, Figure 2.6, for each combination of spacing/radius, we can calculate and determine from our model of the balance between F_e and F_m whether the nanowire pair will be in bridging/threshold/non-bending category. In particular, for the threshold condition, Figure 4 plots a combination of spacing/diameter values (purple curve). This calculated

threshold curve describes the boundary between bridging and non-bending configurations. In this simulation $\delta r = 8.7\ nm$ is used because it is the experimental average from the dependence tests. Note that there is only one fitting parameters in our model which is the substrate voltage V_{sub}. By adjusting this parameter we can fit the observed threshold column data points (blue triangle) with the theoretical boundary when V_{sub} = 150 mV, which is consistent with the natural surface potential measured from Kevin-probe microscopy literatures [31] for our n-type silicon substrate ($N_d = 5 \times 10^{18}\ cm^{-3}$).

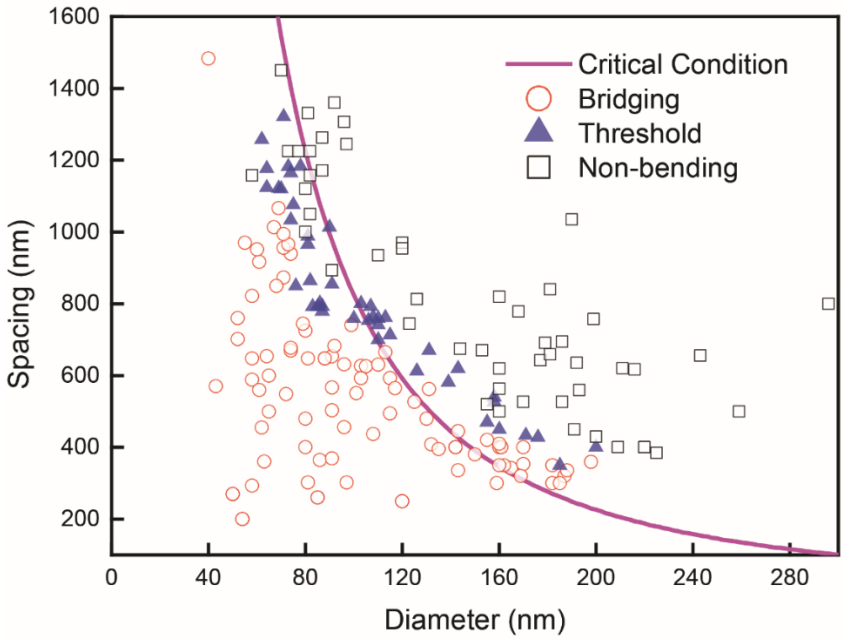

Figure 3.6: Experimental data compared with simulation of NW bridging critical condition. Critical curve calculated form the capacitive force model is shown as purple curve. Data points for nanowires in bridging, threshold or non-bending columns are present by red hollow circles, blue solid triangles and black hollow squares, respectively. The parameters used are $\delta r = 8.7$ nm , $L = 4$ μm; according to experimental conditions $V_{sub} = 150mV$.

3.5 Effect of Substrate Voltage

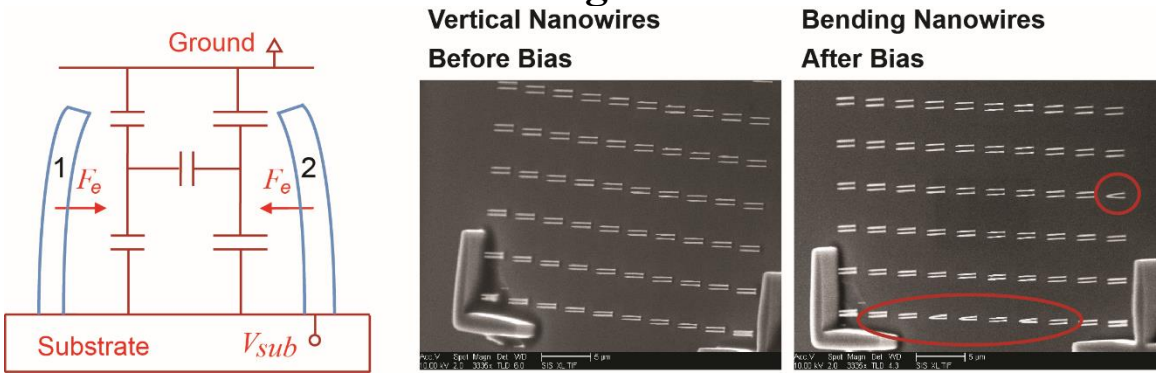

Figure 3.7: SEM images showing nanowire bending after applying 10V bias through the back gate under the substrate.

The substrate voltage V_{sub} is the only fitting parameter in our model simulations, and its main effect is changing the magnitude of capacitive force. In the critical condition simulation above (Figure 3.6), varying V_{sub} will shift the theoretical threshold for bending vertically (purple curve). It is difficult to directly monitor the substrate voltage V_{sub} for the nanowires as it may change during each step of fabrication process. Thus in the simulations a fitting value of $V_{\text{sub}} = 150nm$ is applied to the simulations, which safely falls in the range of natural surface potential measured from Kevin-probe microscopy literatures [31] for our n-type silicon substrate ($N_d = 5 \times 10^{18}\ cm^{-3}$).

However, it is interesting to do a quick back-gate bias test to see the effect of substrate voltage on nanowire attractions. Although our setup does not allow in-situ SEM observation of nanowire bending with external bias applied on the substrate, we applied 10V bias on the back of the Si substrate for 2 minutes before the bias was removed and took the sample into the SEM chamber for observation with the substrate

grounded during imaging. Prior to this experiment, SEM shows that none of the NW pairs on this sample are bending because the array dimensions are outside the bending threshold and there is no sufficient spontaneous attractive forces based on the natural V_{sub} alone. After the 10 V biasing, it is found that even though the external bias is removed, some NW pairs exhibit bending and remain adhered (red circles, Figure 3.7), in particular NW pairs in the bottom row with the smallest spacing, which suggests that varying the substrate voltage has led to stronger attractive forces and more bending, in line with the V_{sub} dependence from our model. Not all NWs remain bending after such a large bias treatment, perhaps due to mechanical restoration forces overcoming most of their adhesion when the bias was removed. In summary, higher substrate bias creates greater potential difference between the pair of nanowires, and induced larger capacitive force that favors bending. This is similar to the working principle of capacitive nano-electromechanical switches [1].

3.6 Analysis for Spontaneous Attraction in Tapered Nanowires

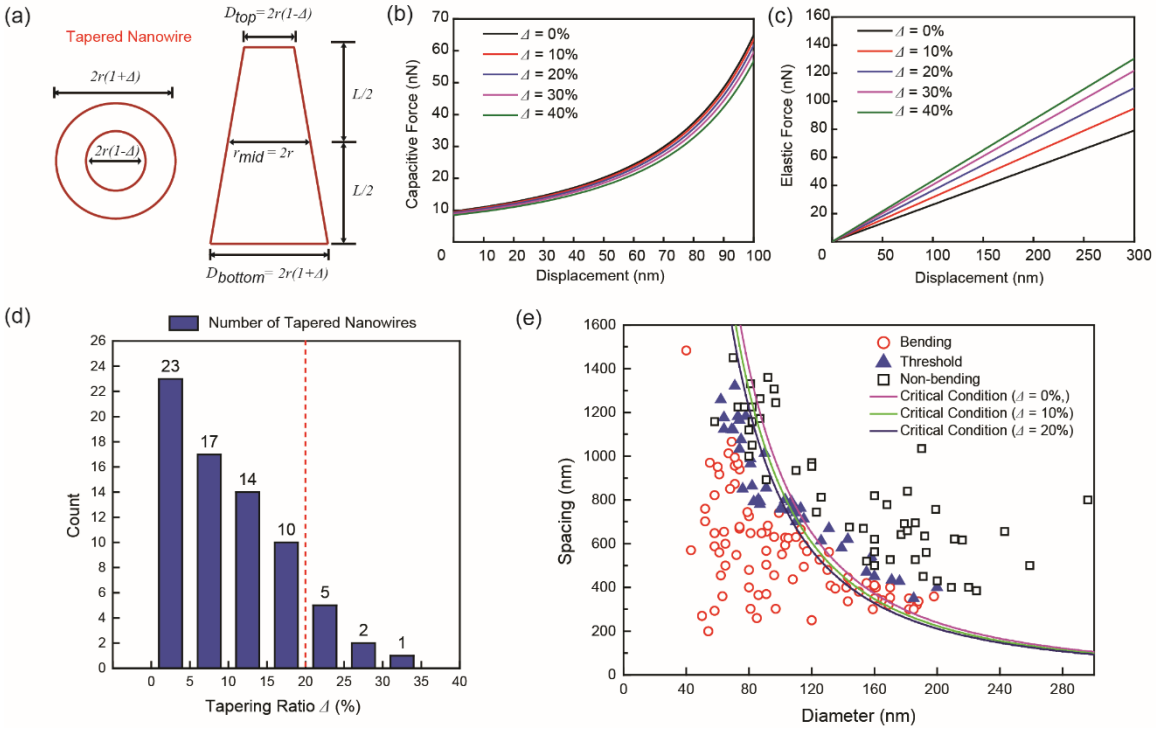

Figure 3.8: Schematics and Simulation results for uniformly tapered conical nanowires. The tapering of a nanowire is indicated by a tapering ratio Δ. (a) Schematics and definition for parameters. (b, c) Simulation of capacitive forces and elastic forces with no nanowire tapering ($\Delta = 0\%$), moderate tapering ($\Delta = 10\%, 20\%$), and significant tapering ($\Delta = 30\%, 40\%$).In this simulation, $d = 330\,nm$, $r = 80\,nm, L = 4\,\mu m, \delta r = 8.7\,nm$ and $V_{sub} = 150\,mV$. (d) Histogram showing the number of nanowires with measurable tapering ratios from experiments. The dashed red line shows that a majority (90%) of nanowires in this study have very small or moderate tapering $(\Delta \leq 20\%)$. (e) Calculated critical condition curves at different levels of tapering compared with experimental data. The threshold curves show very small deviation from that modelled with uniform, non-tapered nanowires, even with moderate tapering (Δ = 10% or 20%).

Upon further inspection, some of our studied nanowire pillars are not perfectly cylindrical, but rather of a slight conical tapered shape based on the SEM images. This is a limitation from the RIE etch fabrication process. We have studied effects of nanowire tapering to our spontaneous attraction model and found that moderate tapering

does not have a significant effect on the calculation of critical bending conditions compared to simply using a uniform nanowire with the same center or average radius to represent tapered nanowires. The simulation result is shown in Figure 3.8. We use a model of tapered conical nanowires, with the change to the radius along nanowire length indicated by a tapering ratio Δ (Figure 3.8a). The capacitive force F_{e} at the tip of the nanowire is:

$$F_{\mathrm{e}} = -\left[\delta \mathrm{V} \frac{r_{\mathrm{top}}\left(r_{\mathrm{top}} + \delta r_{\mathrm{top}}\right)}{r_{\mathrm{top}} + \left(r_{\mathrm{top}} + \delta r_{\mathrm{top}}\right)}\right]^2 \frac{1}{(d-2x)^2} \tag{3.1}$$

And the elastic force F_m is also modified as :

$$F_m = \frac{3EI_{\mathrm{top}}}{L^3}\left(\frac{r_{\mathrm{top}}}{r_{\mathrm{bottom}}}\right)^3 \mathrm{x} = \frac{3\pi E}{L^3}(r_{\mathrm{mid}})^4(1-\Delta)(1+\Delta)^3 x \tag{3.2}$$

These equations and the simulation results in Figure 3.8 (b, c) show that, F_{e} does not change significantly with different tapering levels, while the elastic force F_m increases with more degrees of tapering. Significantly, our result shows that tapering has minimal effect on the calculation of bending thresholds (Figure 3.8 e). This is because while tapered nanowires become more rigid and have a larger F_m, the magnitude of F_{m} is extremely sensitive to values of the average radius r_{mid} ($F_m \sim (r_{\mathrm{mid}})^4$) than the tapering ratio Δ ($F_m \sim (1+2\Delta)$ for small Δ). Therefore any change in rigidity from a finite Δ can easily be compensated by using a slightly smaller radius r_{mid} so the nanowire can be bent with the same F_{e}. For example, when 20% tapering strengthens F_m by around 38%, the threshold radius r_{th} only has to reduce by 6% to compensate this change. Since a majority of our studied nanowires have

tapering $\Delta \leq 20\%$ (Figure 3.8d), we can conclude that our model using uniformly cylindrical NWs represented our experimental distributions very well.

3.7 Conclusion

We propose and experimentally demonstrate a universal mechanism for spontaneous attraction between vertically aligned Si nanowires in terms of electrostatic interaction caused by capacitance differences due to fabrication size variations. Si nanowire pairs with varied diameter, spacing, and radius variance were fabricated using e-beam lithography and RIE process, from which the quantitative investigation of the critical conditions for nanowire bending was performed. Small substrate charges in the capacitive network may create a bias and capacitive attraction force enough to overcome the inherent mechanical restoring force and cause stiction between opposing nanostructures with size variations as small as 12 nm. The capacitive force model provides guidelines for fabricating self-bridging nanowire arrays for potential applications as nanowire-bridge biological sensor or bias-controlled vertical nano-mechanical switch. More broadly speaking, since capacitive force is universal in most nanostructures, this model is applicable to many other nanostructures from bottom-up assembled nanowires[2, 3, 37], nanorods[7, 17 ,38], CNTs[9, 39, 40], graphene[10, 41] to top-down fabricated NEM devices[1, 12-15, 41]. These results illustrate the importance of nanofabrication precision and accuracy, which can be determining

element to the success of scientific research or practical realization of functional devices or systems.

3.8 Acknowledgement

Chapter 3, in part, is a reprint of Z. Sun, D. Wang, J. Xiang. “Self-Bridging of Vertical Silicon Nanowires and a Universal Capacitive Force Model for Spontaneous Attraction in Nanostructures,” ACS Nano, 2014, 8 (11), 11261–11267.

Chapter 4:

Grayscale Electron-beam Lithography for 3-D Nanostructure Fabrication

Inspired by the attraction phenomenon caused by capacitive interactions in nanostructures, we are interested in exploring the opportunities to benefit from it in functional nano-devices. A well-known direct application of such capacitive forces is the nano-electro-mechanical switch, a simple low-power device in which an external bias is applied between the capacitive nanostructure components to control ON and OFF states of electrical connections. However fabricating such a device is not as simple. Among various existing fabrication methods, a novel 3-D patterning technique named "grayscale electron-beam lithography (gray-EBL)" catches our attention with its straightforward operational process and excellent controllability on the dimensions of suspending nanostructures. In this chapter, we will first illustrate the basic concepts of gray-EBL, and then show examples of various suspending nanostructures fabricated with this method. Finally, the calibration of 3D nanostructure geometry through detailed dosage tests with different development conditions will be studied using Atomic-Force-Microscopy(AFM) and Scanning-electron-Microscopy (SEM).

4.1 Principle of Grayscale Electron-beam Lithography

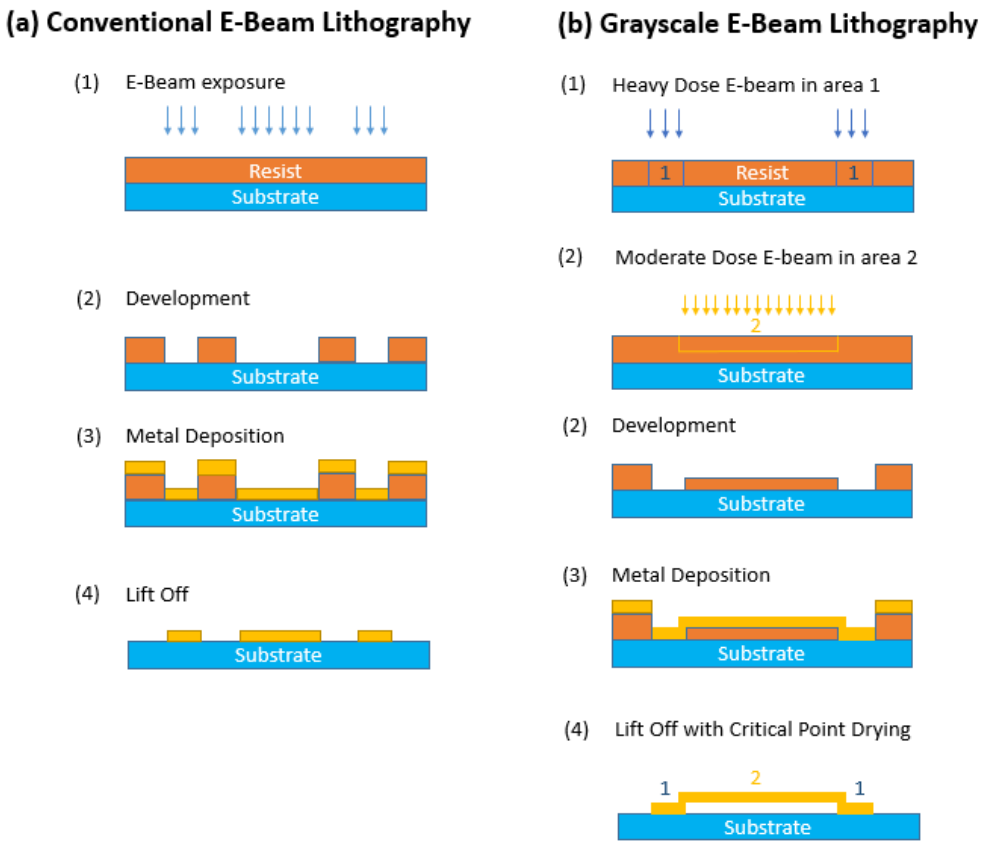

Figure 4.1: Schematic comparison of the process flow in (a) conventional e-beam lithography and (b) grayscale e-beam lithography.

Grayscale electron-beam lithography (Gray-EBL), or 3D e-beam lithography, is a recently developed patterning technique for fabricating high aspect ratio 3D nanostructures over a large device area. It is an ideal method to produce suspending nanostructures with sub-microscale air gaps, and perfectly meets the fabrication demand of micro/nano-electro-mechanical systems (M/NEMS). It is well-know that in the conventional EBL process (Figure 4.1a), the e-beam resists will be injected with high energy electron at target locations, and the solubility of resists will change for certain

solvents. After “development” with these solvents, the resists at patterned location will be either completely removed (negative resist), or remain intact while the rest are washed away (positive resist). In contrast, the main working principle of gray-EBL (Figure 4.1b) relies on setting the injected electron dosage to a moderate level and “partially” penetrate the e-beam resist at designed locations to create “air gaps”, while using high-energy electrons to fully penetrate the resist layers in other areas to form “anchors” that are connected to the substrate. For example, in the “nano-bridge” fabrication process shown in Figure 4.1b, electron beams with high dosage are applied on both sides (area 1), while moderate dosage is used in the middle (area 2). After development, the negative resist at area 1 will be removed, but some residue resist layer with controlled thickness will remain in area 2. Finally, with metal deposition and lift-off, area 1 becomes a metal anchor on the substrate, and in area 2 a suspending beam is formed with an air gap thickness equal to the thickness of the residue resists. The partially-developed resists also served as a sacrificial layer under the metal bridges during lift-off. Particularly, since the lift-off process is usually done with solutions such as acetone, critical point drying (CPD) technique is frequently applied here to minimize the capillary effect and avoid collapsing.

The major advantage of gray-EBL is that air gaps below suspending structures can be precisely controlled from electron-beam dosage; yet the whole procedure is done in only one lithography process, with no growth and etching process for traditional sacrificial layers such as dielectrics. For mass-production purpose, this not only improves manufacturing yield by reducing the number of fabrication processes, but also

facilitates the integration with conventional semiconductor devices because a good number of semiconductor materials are notoriously incompatible with traditional dielectric growth process or isotropic etching. Thus we have chosen gray-EBL method to fabricate our capacitive NEM-switches for the reasons above. Exemplary nanostructures fabricated with gray-EBL are also shown in the next sections. By applying a variety of electron beam doses, air bridges with different length, width, thickness and air gap can be readily created.

4.2 Suspending 3-D nanostructures fabrication with Gray-EBL

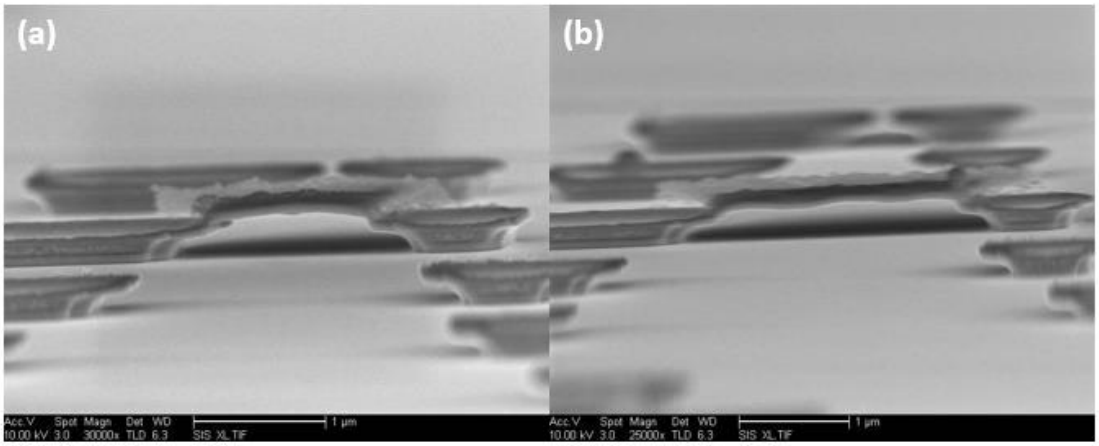

Figure 4.2: SEM images showing suspending nano-bridge structures fabricated with gray-EBL: (a) e-beam dose 60 μC/cm^2, beam length 1 μm, air gap 320 nm. (b) center e-beam dose 60 μC/cm^2, beam length 2 μm, air gap 280 nm. All scale bars are 1 μm.

The first type of 3-D nanostructures we created with grayscale electron beam lithography is the suspending nano-bridges (Figure 4.2) with the discussed process flow

in Figure 4.1b. First, substrates of n-type Si (100) with 100 nm thick thermal SiO_2 layer are cleaned with acetone, isopropyl alcohol (IPA), and DI water for 5 min with sonication. Next, 150 nm thick Polymethyl methacrylate (PMMA) e-beam resist layer are first deposited on the SiO_2 substrate by spin-coating and baked on a hot plate at 180 ˚C, followed by a 350 nm thick methyl methacrylate (MMA) layer spin-coating and baked with the same condition. The resist is then exposed with heavy doses (350 $\mu C/cm^2$) at the "anchors" on both sides, and with moderate doses (60 $\mu C/cm^2$) in the middle where the "suspending beam" will form. Afterwards, the patterned resist was developed in a 3:1 mixed solution of isopropyl alcohol (IPA) and methyl isobutyl ketone (MIBK) at room temperature 23.5˚C for 60 s. Finally, 10 nm Cr and 60 nm Au are deposited with Themescal BJD 1800 e-beam evaporators, and the lift off was done in acetone with Tousimis AutoSamdri 815A critical point dryer (CPD). The nano-bridges with different length are then formed.

Notice that the MMA-PMMA double-layer resist applied here has a reversed structure compared with the conventional setup, in which the PMMA is at the top and MMA is traditionally at the bottom for easier lift-off. We purposefully deposited the MMA layer on the top because MMA is more sensitive to e-beam exposure, and could be cleanly removed after development with moderate e-beam dosage while keeping the PMMA layer beneath intact. The suspending air gap height will depend on the remaining thickness of PMMA after development. The sensitivity of MMA and PMMA layers to e-beam doses are studied with AFM height measurements in the next section.

From the SEM images of nano-bridges in Figure 4.2, we can see that suspending beams with various length, thickness and width are readily fabricated with gray-EBL. Moreover, the height of air gap beneath the beam is also dependent on the length of the structure. With the same dose 60 μC/cm^2, the beam with 1um length gives 320nm air gap while the 2um beam has the air gap reduced to 280nm. This is possibly due to the change in beam mechanical stiffness when beam length is longer. It implies that when other geometrical parameters are fixed, there is a maximum limit on the length before nano-bridge collapse due to its weakened Young's modulus. To see more of this effect from length variation, in Figure 4.3, a series of suspending beams with length from 1-5 μm made with dose 70 μC/cm^2 has gradually decreased air gap height from 157 nm (1 μm length) to 110nm (4 μm length), while the 5 μm long beam collapsed on to the substrate.

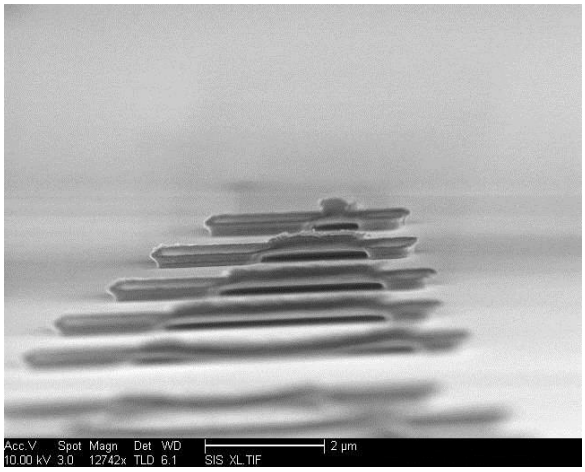

Figure 4.3: Side-view SEM images showing suspending nano-bridge structures fabricated with various beam length from 1 μm to 5 μm. E-beam dose 70 μC/cm^2. The scale bar is 2μm.

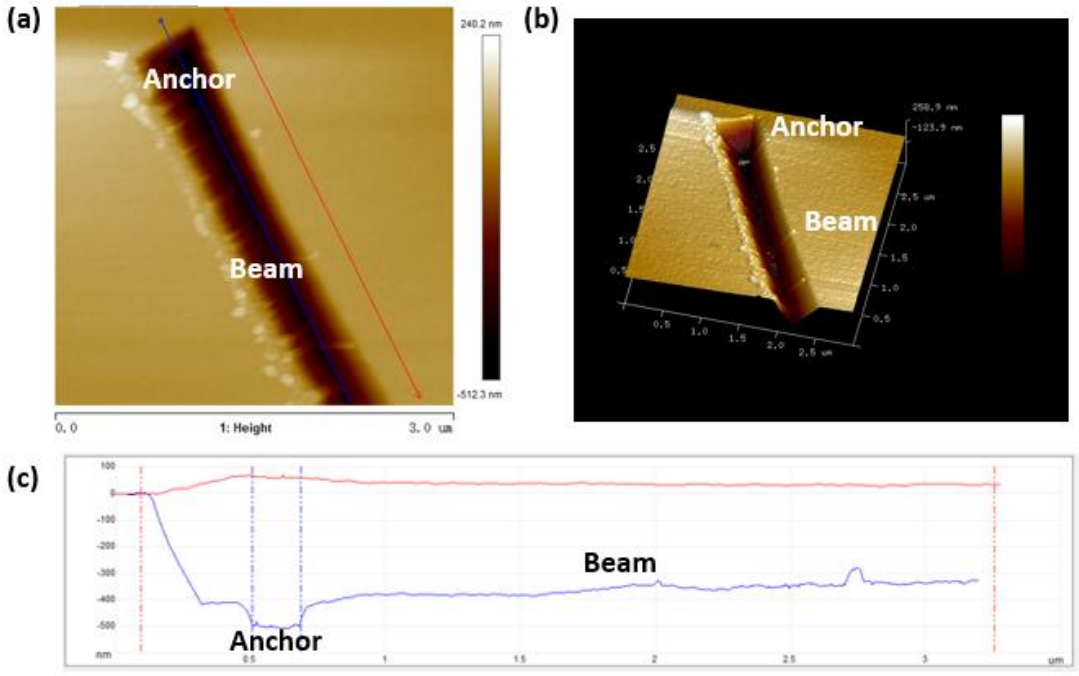

Figure 4.4: AFM study on the resist layer after development for nano-bridge structures fabrication, with anchor dose 350 μC/cm^2 and beam dose 75 μC/cm^2. (a) 2-D topography, (b) 3-D image of the etched trench after development and (c) height profile measurement along the developed region (blue) and the undeveloped region (red).

The AFM study on a resist layer patterned and developed for nano-bridge fabrication (before metal deposition and lift-off) is given in Figure 4.4. The anchor region has heavy dose 350 μC/cm^2 to ensure that all resist in this area are fully exposed and removed with developer solution, while the beam region receives a moderate dose 75 μC/cm^2 to maintain some remaining resist layer for subsequent suspending-beam deposition. From the height profile of the developed "trench" in the resist layer (blue curve, Figure 4.4c), depth of the fully-penetrated "anchor" is measured to be about 500nm, which is exactly the total thickness of the MMA+PMMA resist; and compared

with the reference of the lower anchor region, the remaining resist along the "beam" region has an average thickness of 123 nm, which is expected to be the height of the air gap after resist lift-off. Notably, although the doses are digitally designed in each region without any intentional transition, the height profile at the edges of the "anchor region" is still gradually rising instead of a steep change. This is due to the proximity effect caused by electron scattering inside the resist and on the SiO_2 substrate. Also because of the proximity effect, it is observed in both 2-D and 3-D topography images (Figure 4.4a, b) that the "trenches" has a tilted sidewall with angle around 45˚. During subsequent metal deposition, some metal will adhere to this sidewall making protruding "wings" at the edges. We can see this phenomenon in side-view SEM images (Figure 4.2) near the edges of the anchors and the suspending beams. It explains why the thickness of the beam/anchor looks larger than the deposited 70nm (10nm Cr + 60nm Au).

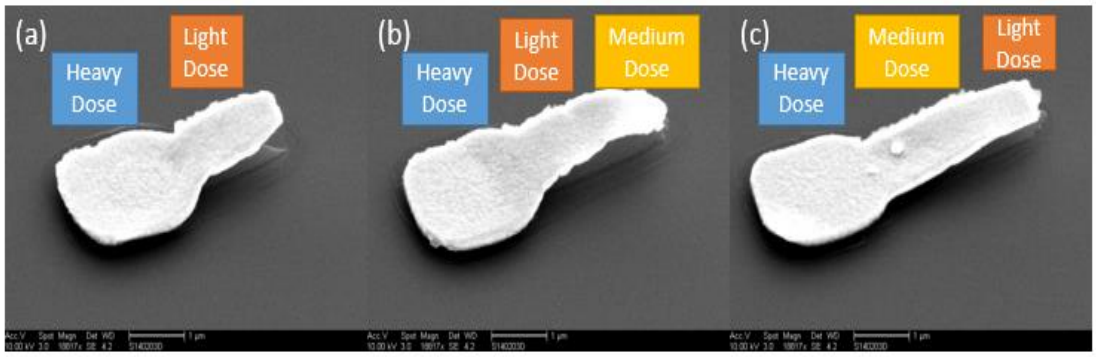

Figure 4.5: 45˚Tilted-view SEM images showing suspending nano-cantilever structures with different combinations of e-beam doses. Various structural profiles are achieved by controlling air gaps in each region with gray-scale EBL. All scale bars are 1μm.

Naturally, single-anchor nano-cantilevers can also be fabricated with gray-EBL. By applying heavy and light e-beam doses in different areas (Figure 4.5a), the metal thin film on the right is suspended with an air gap. Additional tricks can be done by the dose control to make special shapes of cantilevers. For instance (Figure 4.5b), an additional region with medium dose can be added to the right of the "light-dose" area, such that a "dip" with smaller air gap height is formed on the basis of original cantilever. This technique is particularly useful to reduce the pull-in voltages in a NEM-switch, and makes sure that electrical connections are formed between the drain electrode and the lower "medium-dose" area, while keeping the higher "light-dose" part (typically above the gate electrode) away from touching the gate and create gate leakage or short-circuits. Another practice is also very useful in 3-D nanostructure fabrication. In Figure 4.5c, a nano-cantilever with increasing air gaps are prepared with gradually reduced doses along the metal beam. This is suitable for making larger air gaps because the "medium-dose" region will serve as structural connection with the "anchor" and higher beams with greater air gaps. By repeating this increment, the air gap height is able to reach its theoretical maximum which is the total thickness of the resist layer.

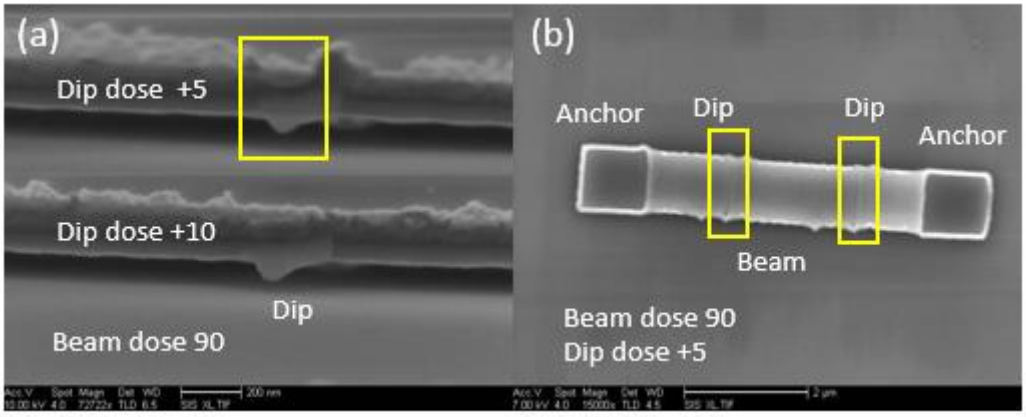

Figure 4.6: (a) Side-view and (b) top-view SEM images showing double-anchor suspending beam structures with probing "dips" fabricated with additional e-beam doses at specific locations. The doses for the beams and dips are indicated on the graphs (unit μC/cm^2). The scale bars are 200 nm and 2 μm respectively.

The additional-dosage technique can certainly apply to the double-anchor suspending beam structure as well. In Figure 4.6, probing "dips" with smaller air gaps are fabricated on the suspending beams by setting additional e-beam doses at the specific locations. The beam with dose 90 μC/cm^2 has an air gap 89 nm, and applying +5 or +10 μC/cm^2 additional doses will reduce the dip air gap to 50 nm or 39 nm respectively. Since the deposited metal thin film has the uniform thickness, the dips will show up as shallow trenches in the top-view SEM with diameter about 50 nm. This method is also used in our fabrication of doubly-clamped beam NEM-switches to reduce pull-in voltages and avoid gate leakage currents.

4.3 Precise control on geometries of 3-D nanostructures

Grayscale e-beam lithography is advantageous in fabricating suspending structures with various shapes and air gaps. It does not require any mask or additional sacrificial layers to make 3-D structures, and has a higher spatial resolution thanks to the precisely control in both planar mapping (pixel-to-pixel distance less than a few nanometers) and height determination (area dose sensitivity up to 0.5 $\mu C/cm^2$). Hence besides NEM-switch fabrication [54], this technique is also useful in optoelectronic devices [55], ultrasonic machining [56] and laser micromachining [57]. The core technique of gray-EBL is how to control the remaining thickness of resist by adjusting the proper energy level of incident electrons [58]. Both e-beam exposure and resist development (etching) will play important roles in this process. We will study these effects with systematically designed experiments in the following sections.

4.3.1 Resist Sensitivity to E-beam Exposure

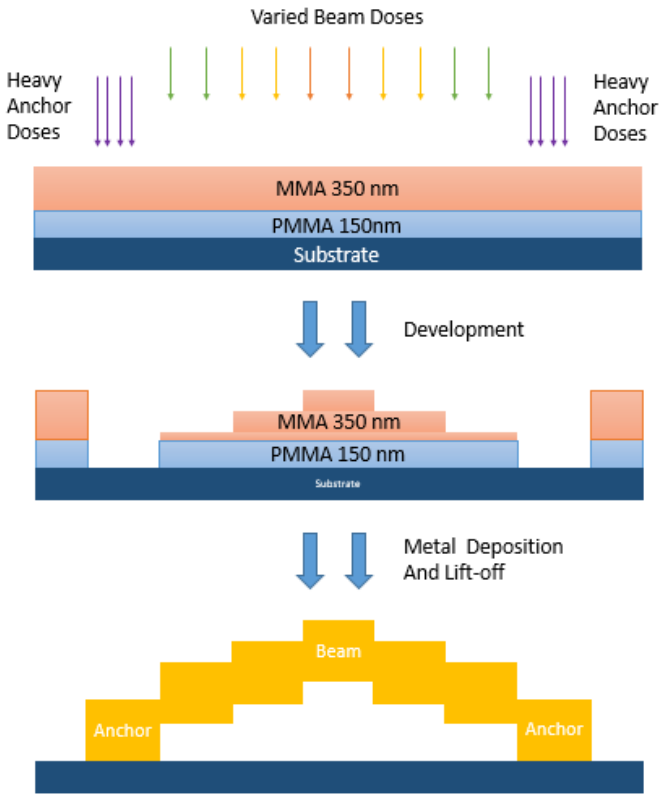

Figure 4.7: Schematic diagram showing the fabrication of staircase nanostructures with gray-EBL. The gradual increment in air gaps is achieved by controlled e-beam exposure on the center with digitally varied doses.

First and foremost, we investigate the resist sensitivity to electron beam exposure, in order to find the relationship between e-beam dosage and remaining resist thickness after development, which determines the air gap height in 3D-nanostructures. To study this effect, we first create stair cases structures with processes shown in Figure 4.7. Again, a MMA-PMMA double layer resist is deposited on SiO_2 substrate. Heavy doses are used at both ends to form the anchors, and moderate doses are applied at the middle in a binary fashion. After development, staircase structure in the remaining resist

appears in the AFM height profile measurement. The individual sensitivity of both MMA and PMMA can be determined from the AFM data. Finally, after metal deposition and lift-off with CPD, staircase 3D meal beam is created and the air gaps under each "stair" are measured from side-view SEM images.

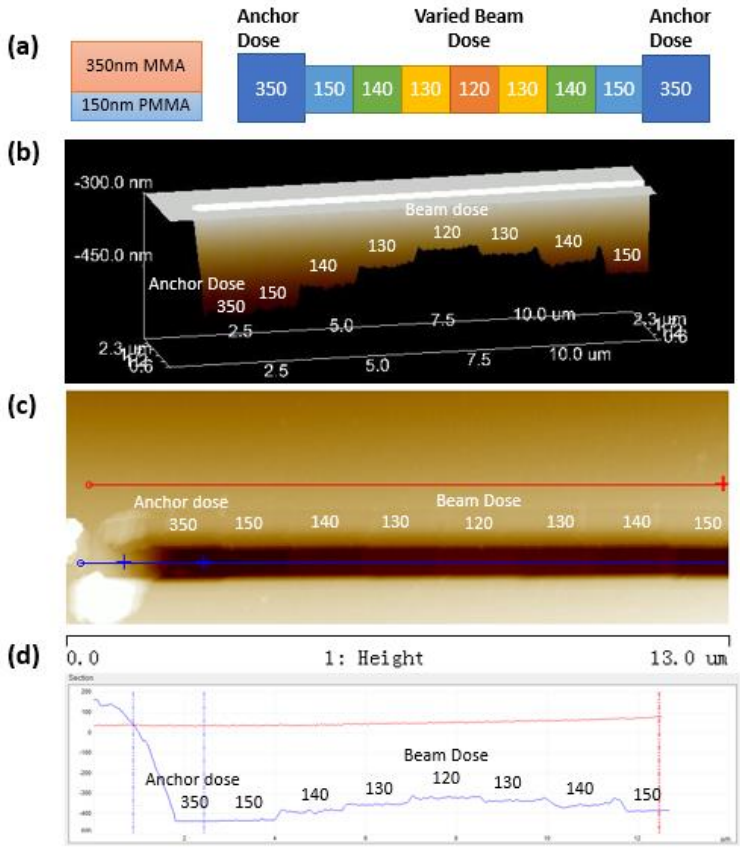

Figure 4.8: AFM study on the developed resist for staircase nanostructures fabrication. (a) Resist composition and dosage distribution in the "anchor" and "beam" regions (unit $\mu C/cm^2$). (b) 3-D side-view topography of the developed resist. (c) 2-D top view topography with (d) height profile measurement for the remaining resist.

Figure 4.8 demonstrates an exemplary AFM measurements on a developed resist layer for staircase nanostructures (development done in MIBK:IPA 1:3 solution for 60s at room temperature 23.5˚). Here, the anchor area has a very large dose 350 $\mu C/cm^2$

such that all the MMA-PMMA resist layer are removed and the silicon substrate is exposed. The dose in the beam region varies gradually from 120 to 150 μC/cm^2, with the minimum dose 120 μC/cm^2 at the center to form a peak, and the greater doses near the anchor to work as necessary connections for the next "stair" (Figure 4.8a). Figure 4.8b shows the side-view 3D-topography zoomed-in at the bottom of the etched trench. Significantly, the profile of the resist clearly exhibits staircase shape. The height of each "stair" is measured along the developed trench (blue line, Figure 4.9c, d), and the etched depth is calculated by comparing with the profile of nearby undeveloped resists (red curve). Notice that the height of the peak (116nm) with dose 120 μC/cm^2 is already within the bottom PMMA layer (thickness 150nm), suggesting that all the MMA layers are already fully exposed and removed with this level of dosage.

After 60nm Ti deposition and lift-off with CPD, the staircase-structure emerges on the basis of remaining resist layer. From the segments of different doses 120/130/140 μC/cm^2 (Figure 4.9a), we can clearly observe the binary increment in their air gap heights. It is also evident that the air gap height at each segment measured by SEM (red curve, Figure 4.9b) matches perfectly with the thickness of remaining resist measured by AFM (black), strongly indicating that the height of remaining resist directly determines the geometry of the 3-D nanostructures. Also critical point drying (CPD) is proven to be very effective in reducing the capillary effect during lift-off process to avoid attraction or collapse of the nano-beam. Lastly, Figure 4.9 (c-d) depicts the relationship between doses and air gaps. The air gap gradually decreases as the dose

increases. For dose 150μC/cm^2, the air gap disappears and the suspending beam is touching the substrate like an anchor.

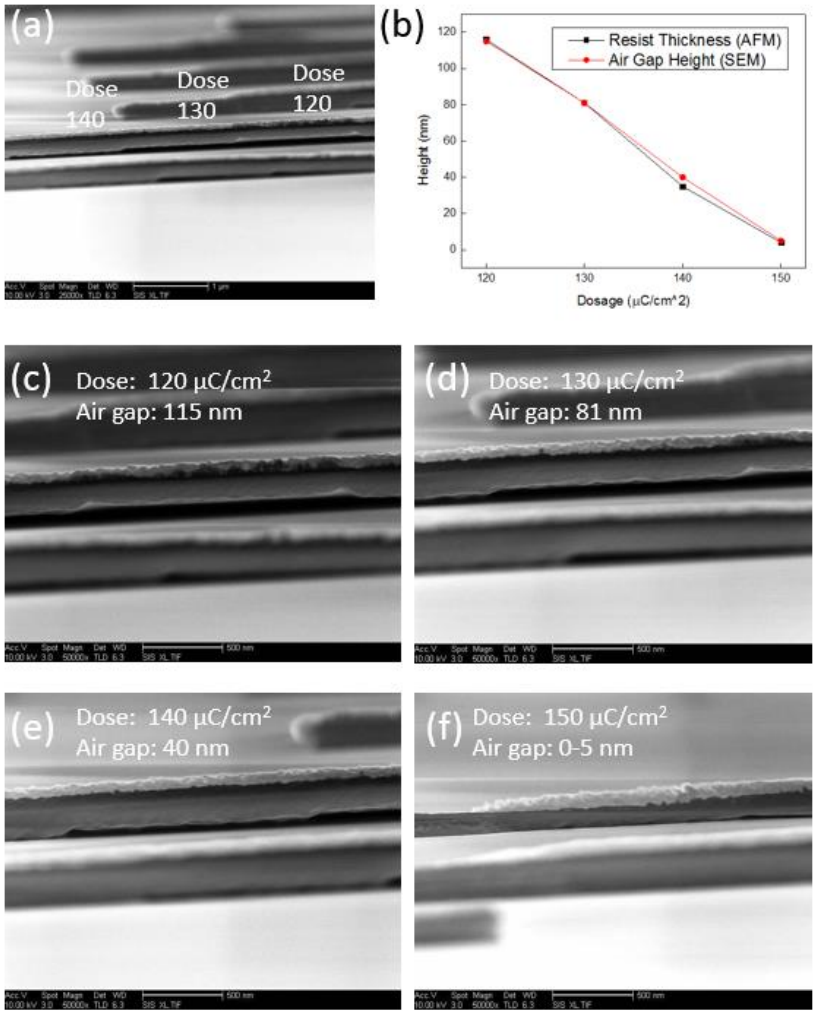

Figure 4.9: (a) Side-view SEM image on a segment of staircase nanostructures fabricated form the resist layer shown in Figure 4.8. The corresponding doses are indicated on the graph with unit μC/cm^2 (b) Comparison between the resist thickness measured by AFM (black curve) and the air gap height measured by SEM (red curve). (c-f) Side-view SEM images showing the air gap height and dose level in each "stair" segment. The scale bars are 1μm and 500nm.

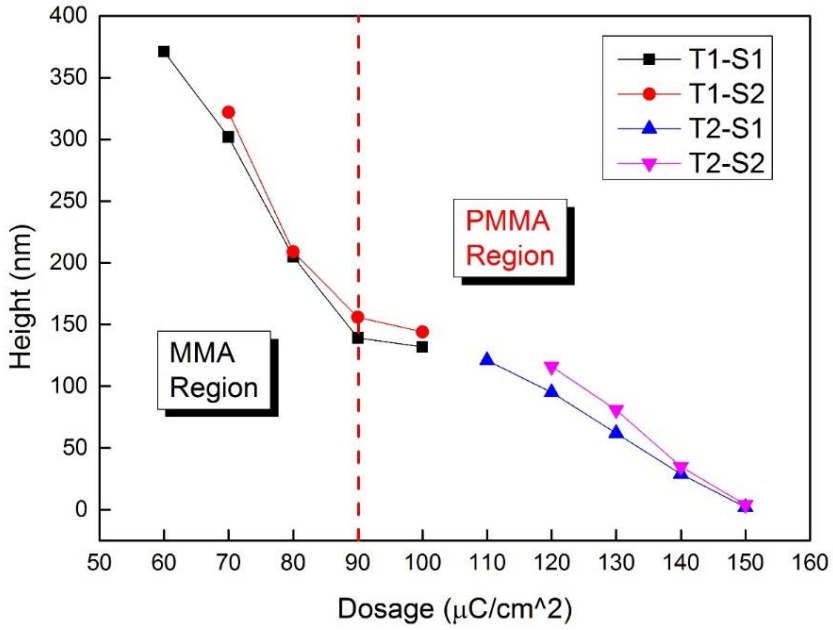

Figure 4.10: Remaining resist height versus e-beam exposure dosage, with data obtained from 4 different samples. The bilayer resist (350 nm MMA on top of 150 nm PMMA) is exposed with varied doses from 60 to 150 μC/cm^2, and developed in MIBK:IPA 1:3 solution for 60s at room temperature. The red dashed line indicates the threshold dosage 90 μC/cm^{2}for penetrating all the MMA resist.

Similar dosage tests are repeated on the bilayer resist with diverse dose from 60 to 150 μC/cm2, developed in MIBK:IPA 1:3 solution for 60s at room temperature. A plot showing the remaining resist thickness versus e-beam dosage is present in Figure 4.10. First, the obtained data are very consistent between different tests, indicating the repeatability of vertical geometry control of nanostructures with gray-EBL. Second, at a threshold dose 90 μC/cm^2 (red dashed line), the remaining resist height happens to be around 150nm, which is the total thickness of the PMMA layer. Hence this red line also serves as a boundary between lower doses that only expose the MMA region on top,

and higher doses that start to penetrate into the PMMA region at the bottom. In addition, we can see that the data points in both MMA region and PMMA region show good linearity, with two different slopes in each region. From the fitting slopes and the total thickness of the resist layer (500 nm), we are able to calculate the resist sensitivity to e-beam exposure for both MMA (8.12 nm / ($\mu C/cm^2$)) and PMMA (3.43 nm / ($\mu C/cm^2$)). The MMA has a better sensitivity, and is more suitable for fabricating tall 3D nanostructures with a large variation in vertical dimension. On the other hand, the PMMA has better precision in controlling the remaining resist thickness with variation of doses, and is ideal for making nano-devices with precise air gaps.

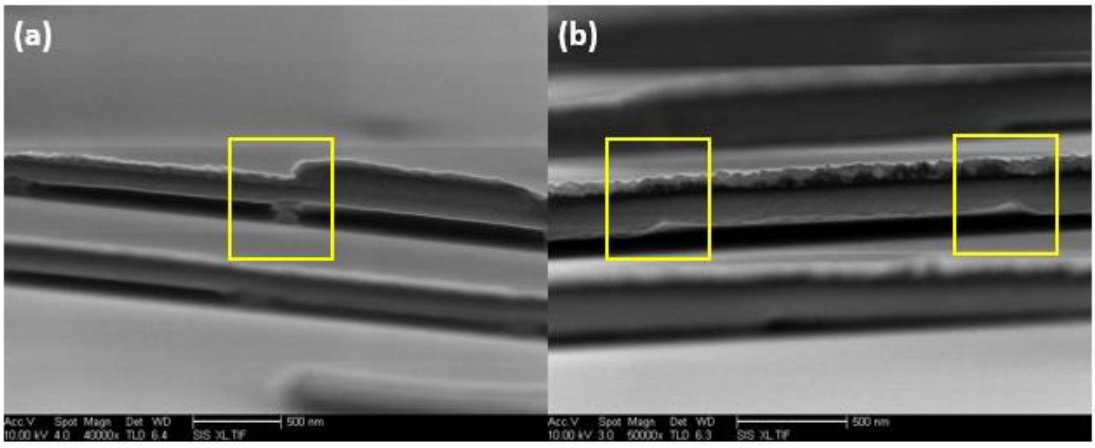

Figure 4.11: Side-view SEM image showing staircase nanostructures (a) with proximity effect and (b) without proximity effect. The scale bars are both 500nm.

There is, however, a “proximity effect” in grayscale e-beam lithography that must be corrected because it usually causes over-dose exposure at pattern boundaries. The proximity effect is triggered by the scattering of injection electrons inside the resist

layer and at the surface of the substrate. It typically occurs at the joint edge between regions patterned with different doses. When the two patterns are very close, the scattered electrons may spread and overlap, causing excess dose right at the boundary. The SEM image in Figure 4.11a depicts an example of over-exposed edge caused by the proximity effect between two “stairs” in the suspending beam structure. The resist at the edge of two “stairs” is accidentally fully exposed, resulting in an “off-design” narrow pillar after metal deposition. The best way to fix proximity effect is to find the spatial dosage profile through experiments [58], calculate the electron scattering for different doses and pattern geometries, determine the electron-point-spread-function (ESPF) [59], and finally generate a gradually varied dosage mapping for the patterns. This method is widely applied in fabricating optical diffraction gratings [55, 59] and nanoimprint molds [60] that require strict geometry at boundaries. Alternatively, a more practical and straightforward way to circumvent the proximity effect is to measure the pixel-to-pixel distance designated by the e-beam writer, and leave a narrow empty region (zero dose) with width slightly larger than the pixel-to-pixel distance between two patterns. For example, this simple method is applied to the staircase structure in Figure 4.11b and the over-dose due to proximity effect is then corrected.

4.3.2 The Resist Development Conditions

As previously mentioned, another factor that determines the geometry of 3-D nanostructures fabricated with gray-EBL is the resist development condition. In the

prior dosage tests, we used MIBK:IPA1:3 solution to develop the exposed resists for 60s at room temperature (RT, 23.5˚ C). We can also vary the development conditions such as time and temperature to study their effect on modifying the shape of nanostructures.

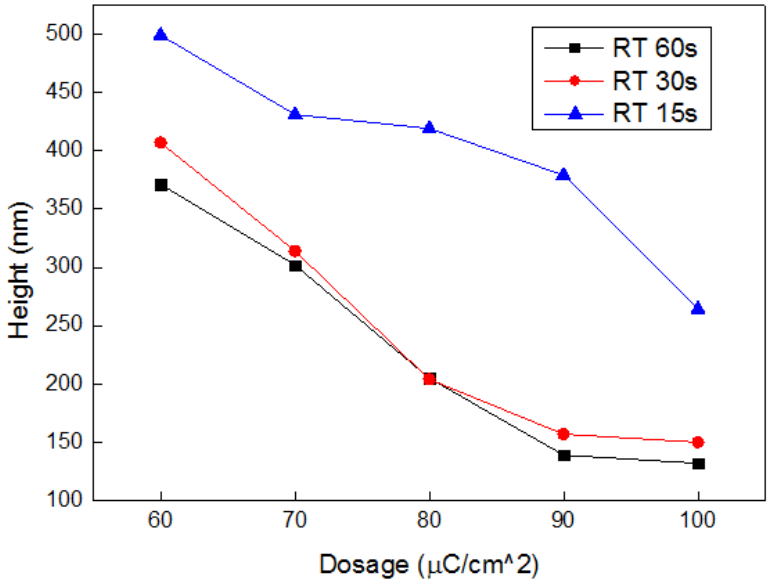

Figure 4.12: Remaining resist height versus e-beam dosage plot for different developing time. The MMA (350nm) and PMMA (150) bilayer resists are exposed with various doses, and developed in MIBK:IPA 1:3 solution at room temperature for 60s, 30s, and 15s respectively.

First, the development time in MIBK:IPA 1:3 solution is varied and the height of remaining resists versus different e-beam dosage is measured in Figure 4.12. Obviously, for 15s development, the resists are under-etched so the remaining height is comparably much greater than 30s and 60s development results. Notably, at dose 60 $\mu C/cm^2$, for 15s development the resist is barely etched as it keeps the original thickness

of 500nm, but for 30s and 60s development there is a significant decrease in the resist thickness. What is more, the etched resist depth (subtracting remaining resist height from total thickness 500 nm) for 30s is slightly smaller than that for 60s, but they are comparable in magnitude so the etching depth is expected to reach saturation. This result indicates that resist development is not a linear process: for light dose 60 μC/cm^2, etching to the resist freezes in the first 15s; but after certain time period (30-60s), adding etching time does not effectively reduce remaining resist layer thickness anymore. Also noteworthy is that for 30s and 60s development, dose 90 μC/cm^2 is still the threshold dosage before penetrating the underlying PMMA layer, as the height vs dosage slope (sensibility to exposure) starts to change at this point.

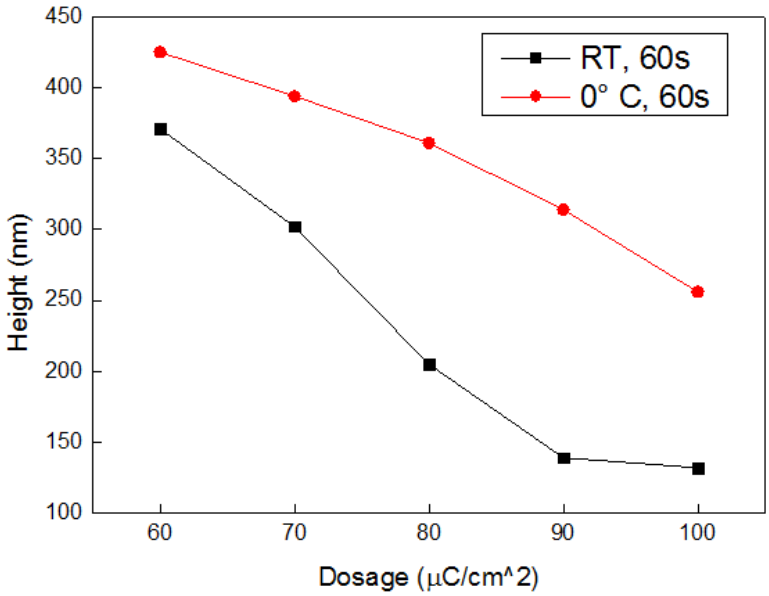

Figure 4.13: Remaining resist height versus e-beam dosage plot at different temperatures. The MMA (350nm) and PMMA (150) bilayer resists are exposed with various doses, and developed in MIBK:IPA 1:3 solution for 60s at room temperature (RT, 23.5˚) and 0˚C respectively.

Next, we change the development temperature to zero degree Celsius by conducting the development process in a cooling bath with ice-water mixture for 60s. Then the remaining resist height versus dosage relationship at 0˚C is compared with room temperature results (Figure 4.13). Naturally, since the resist development is a chemical etching process closely associated with the temperature, the etching rate at 0˚C turns out to be much slower than that at the room temperature. Because of that, even with larger dose 100 μC/cm^2, the remaining resist after 0˚C 60s development is still in the MMA region, with the data points showing a uniform linear slope (indicating the sensitivity of MMA at 0˚C). However there is an advantage for 0˚C development. Although it will take more time to etch the resist to a certain thickness level, the slower progress renders better and more accurate control on the design of geometry.

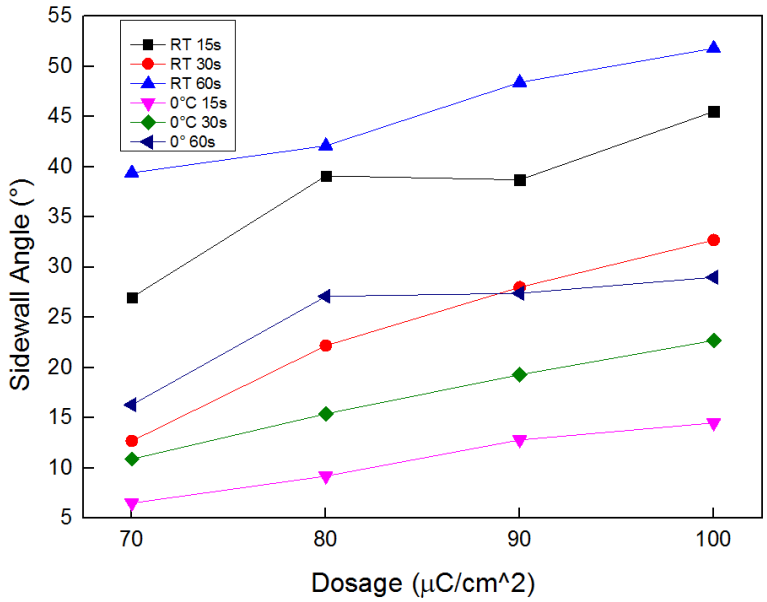

Figure 4.14: Remaining resist sidewall angle versus e-beam dosage plot for different development time and temperatures.

Finally, the sidewall angle of the etched "trench" mentioned in section 4.2 (Figure 4.14) is also affected by both development time and development temperature. Overall, the sidewall angle is proportional to the e-beam dosage, and longer time or higher temperature favors large sidewall angle. For 60s development at room temperature, the sidewall angle reaches a maximum between 39.4˚to 51.8˚. However the angle is very small (6.5˚ to 16.3˚) for short period development 15s at low temperature 0˚. This will create a problem in defining the steep edges in nanostructures such as the staircase structure. For example, in the remaining resist profile developed at 0˚for 15s shown in Figure 4.15c, due to very small sidewall angles, the boundaries between areas with different dosage are "smoothed out". Thus it is critical to select appropriate development strategies for fabricating nanostructures with different geometries and surface profiles.

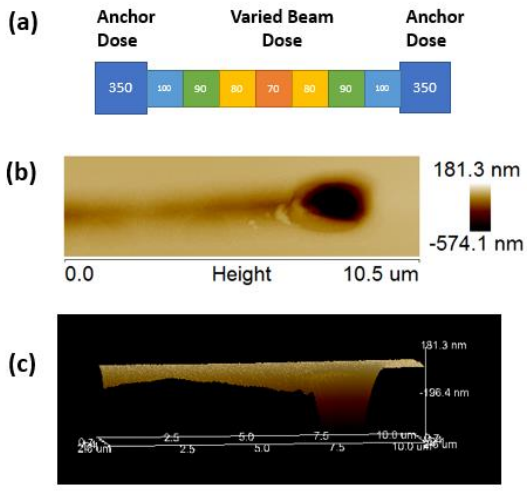

Figure 4.15: AFM study showing the "smoothing effect" when the resist is exposed with various doses and developed for a short period of time 15s, at low temperature 0˚C (a) Dosage distribution design in the "anchor" and "beam" regions (unit μC/cm^2). (b) 2-D top view topography. (c) 3-D side-view topography of the developed resist.

4.4 Conclusion

In this chapter, we have illustrated the principle of grayscale electron-beam lithography and given examples of various types of suspending 3-D nanostructures fabricated with this method. Several factors that affect the precise control of 3-D nanostructure geometry, such as the resist sensitivity to e-beam dosage, development time and development temperature are studied with AFM and SEM. With sufficient data to optimize the gray-EBL technique, we are now ready to fabricate our 3-terminal NEM-switch which is a direct application of capacitive-force-induced attraction in nanostructures.

4.5 Acknowledgement

Chapter 4, in part, is a reprint of Z. Sun, S. Kwon, J. Xiang, “Low voltage three-terminal nanoelectromechanical switches using grayscale lithography”, to be submitted.

Chapter 5:

3-Terminal Nano-electro-mechanical (NEM) Switches

5.1 Introduction

The nano-electro-mechanical (NEM) switch is a direct application of capacitive forces in nanostructures. Similar to conventional semiconductor switches, the NEM switches are also functional as relays, transistors, logic devices and sensors, but with fundamentally different working principles. Although transitional semiconductor devices such as CMOS (complementary metal-oxide semiconductors) are dominating the market with their supreme performance, good reliability, and extremely low cost thanks to decades of development in semiconductor industry, the continuous scaling of CMOS devices will eventually cause serious power consumption issues. On the other hand, The NEMs switches offer advantages such as reduced leakage currents [61], lower power consumptions [62] and improved on/off ratios [62,63]. In addition, their operations are comparatively unaffected by harsh environments such as extreme temperature [64], radiation[65], and external EM fields [66]. Therefore, exploring the practical applications of NEM switches and incorporating them into conventional semiconductor industry are beneficial in many ways. However, due to their lower fabrication yield and operational reliability caused by complications such as spontaneous attraction phenomenon, NEM switches are unlikely to replace

conventional semiconductor devices in the near future, but may work as supplementary devices for low power needs. Again, this addresses the importance of understanding fundamental physics behind nanofabrication.

5.1.1 Operation Principle of NEM switches

A NEM switch operates similar to a traditional mechanical switch used for light bulbs, but with a much smaller size in nanometers. Typically a NEM switch consists of a movable component (active element) in the form of nano-cantilevers or suspending nano-beams, and a local control pad (gate) that attracts the movable component through externally-biased electrostatic interaction to form an electrical connection ("switch-on"). If the elastic restoration force of the cantilever or beam is large enough to overcome the adhesion forces (generally dispersion forces and capillary forces) at the contact, the attraction will be released when the external bias is removed, and the movable part will return to its original position, preparing for switching in the next cycle. This is called the "volatile behavior" of NEM-switches (Figure 1.12b). Notably, due to the adhesion forces, the "pull-out" voltage is usually less than the "pull-in" voltages, causing a hysteresis in the output current versus gate voltage diagrams of NEM switches. Furthermore, whether the restoration force is sufficient to break adhesion on the contact surface depends on a couple of variables, such as the stiffness of the active element, the air gap height between active element and the control electrode, the surface roughness and the humidity in the working environment. With smaller air gap or reduced

cantilever/beam stiffness, it is feasible to obtain lower "pull-in" voltages, faster switching speed, and lesser energy consumption. But if the design aiming for better electronic performance is too aggressive such that the restorative elastic force becomes smaller than the adhesion forces, the active element will then "stick" to the electrode, never breaking off and causing a permanent "on" state. This is the infamous "stiction" phenomenon, where the switch exhibits non-volatile operation (Figure 1.12a) or even ceases to work if the stiction is irreversible. Notice that this "stiction" can also happen during the fabrication of NEM devices, which is the "spontaneous attraction" between the active element and the gate. Importantly, stiction is considered one of the major failure modes in NEMS, and must be avoided with careful fabrication designs.

5.1.2 Single-anchor cantilever structure

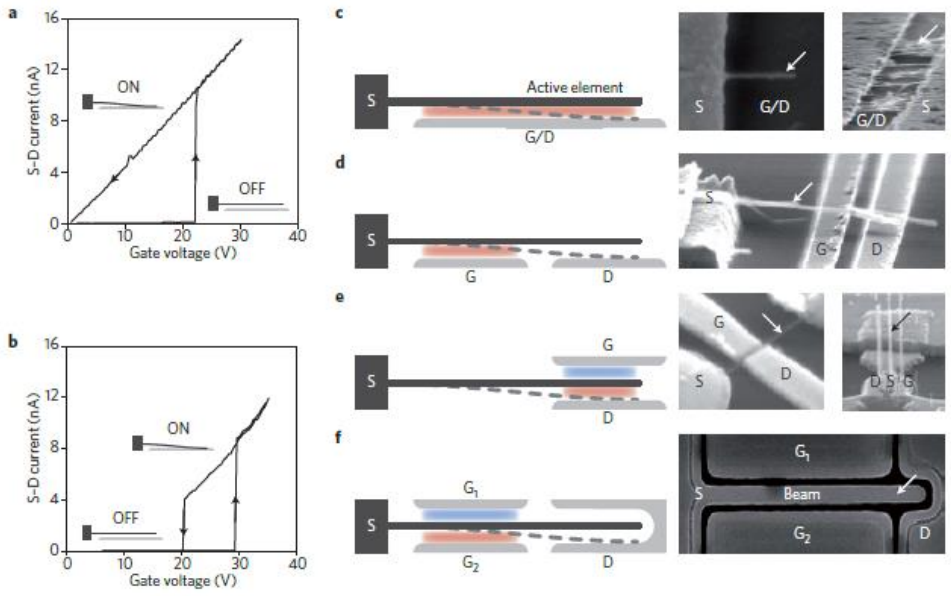

Figure 5.1: Basic operating characteristics of NEM switches. (a-b) Current versus voltage for NEM devices exhibiting (a) non-volatile and (b) volatile behavior. (c-f) Schematics and SEM images for various types of NEM switches. [1]

There are various types and structures for NEM switches. First, by the structures of the active elements, they can be categorized into single-anchor cantilever type and Doubly-clamped beam type. Figure 5.1c-f shows a few examples of single cantilever NEM switches. Different in the number of electrodes, simple 2-terminal switches (only source and gate electrode, Figure 5.1c) and more sophisticated 3-terminal switches (source, drain and one or more separate gate electrodes for switching control, Figure 5.1d-f) can be fabricated. Both the location and the number of gate electrodes play very important roles in controlling the movement and pull-in voltages in the NEM switches. For instance, a gate on the same side of drain (Figure 5.1d) attracts the nano-cantilever to the same direction, but a gate on the opposite side (Figure 5.1e) take advantages of the repulsive interaction between the same-biased gate and source, while the drain is grounded. Furthermore, with two gates on each side, the cantilever has the freedom to move both ways, or hold in the middle with varied combinations of gate biases. This setup is also an effective way to combat accidental stiction during operation.

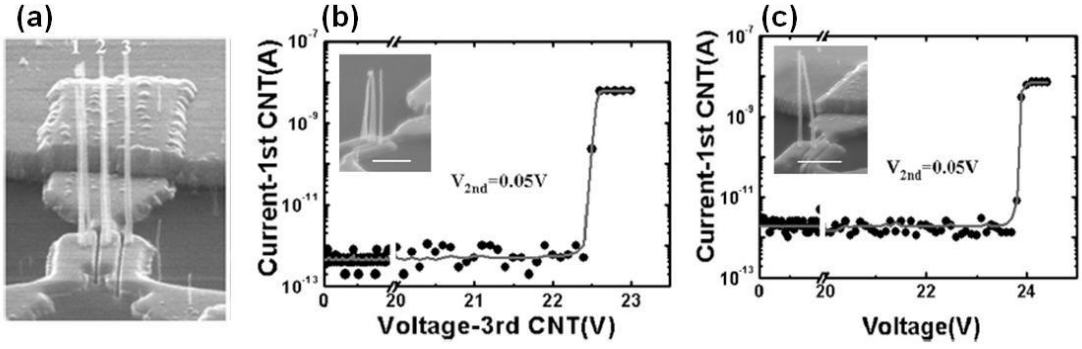

Figure 5.2: 2-terminal or 3-terminal NEM switch with vertical CNT [67]. (a) 45˚tilted SEM image. (b) Transfer curve of the fabricated device with 3-terminal. (c) Transfer curve of 2-terminal. Inset of (b)(c) is the SEM images in the ON state of each device.

A NEM device shown above (Figure 5.2) is of particular interest to the spontaneous attraction research. This nano-switch [67] is based on vertical CNTs, whose structure is very similar to the vertical nanowire array used as our example system to prove the capacitive force model. It is apparent that with external bias between the CNTs, attraction or repulsion are both possible. The authors of this article also mentioned that during the fabrication, spontaneous attraction may occur between the CNTs during growth, and during operations, once the CNTs attract each other the bond was irreversible causing stiction. Only well-designed spacing and geometry may avoid spontaneous attraction in the fabrication process, and the stiction in 3-terminal test may be released by applying a reverse bias on the non-contact electrode to attract the middle CNT (active element) back to the other end.

5.1.3 Doubly-clamped beam Structure

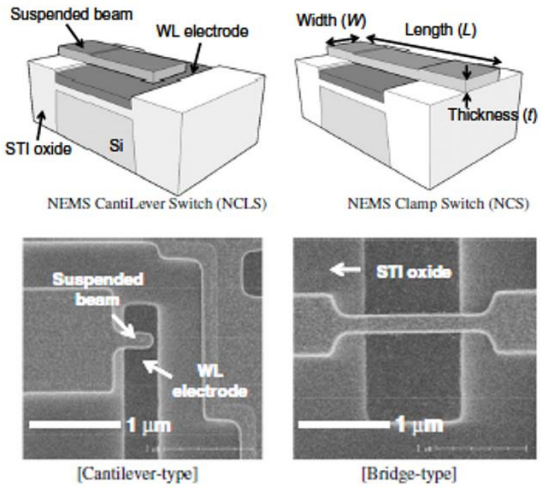

Figure 5.3: Schematics and top view SEM images for single-anchor cantilever and Doubly-clamped beam NEM switches. [68]

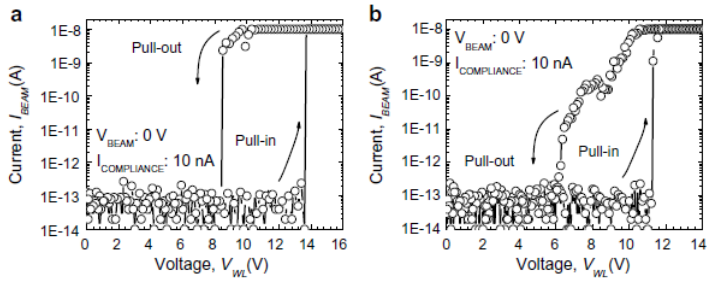

Figure 5.4: I-V plots of the two types of fabricated NEMS switches for (a) cantilever (W/L/t = 200 nm/300 nm/30 nm) (b) clamp (W/L/t = 200 nm/ 1000 nm/30 nm) [68]

Another type of the NEM switch features the doubly-clamped beam structure. With both ends fixed, the doubly-clamped suspending beam has greater mechanical stability, higher resistance to stiction and thus better reliability than the single-cantilevers. Figure 5.3 gives a comparison between both cantilever and double-clamp structures, and Figure 5.4 shows their corresponding I-V plots. Theoretically speaking, for a cantilever and a double-clamp with exactly the same geometrical dimensions and the same air gap toward the electrode, the cantilever shall have weaker mechanical stiffness and favor lower pull-in (switch-on) voltages. However, thanks to the stronger mechanical stability of a double-anchored clamp, beams with longer length and smaller air gaps can be fabricated without stiction, which results in an even lower pull-in voltage depicted in Figure 5.4.

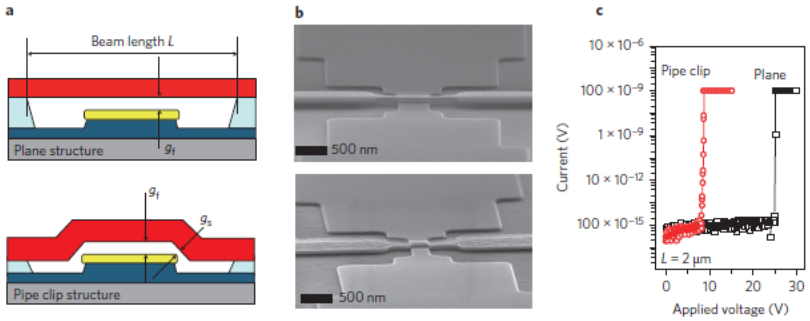

Figure 5.5: (a) Schematics and (b) SEM image for 2-termial plane structure and paper clip structure NEM switches. (c) Measured I-V curve [13]

There is another nice example for doubly-clamped beam structures shown in Figure 5.5. J. O. Lee et, al. made two kinds of suspending beam structures (traditional plane beam and pipe clip) for a 2-terminal NEM switch, and successfully reduced the pull-in voltage while strengthening its reliability in the pipe clip structure, by decreasing the effective contact area between the beam and the gate. It is remarkable that the effective air gap was shortened to as small as 4 nm and the pull-in voltages was pushed to as low as 400mV (Figure 5.6) [13].

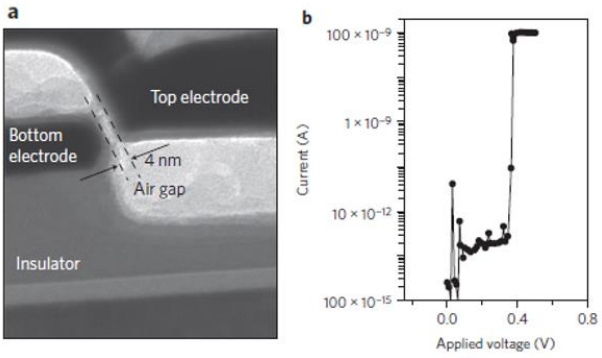

Figure 5.6: (a) TEM image of the clip-pipe NEM switch showing 4 nm air gap (b) I-V characteristics of the two-terminal NEM switch featuring 400 mV turn-on voltage. [13]

5.2 Calculation of Pull-in Voltage

The working principle of NEM-switches is similar to the spontaneous attraction we discussed in Chapter 2 and 3. The switching relies on the capacitive electrostatic attraction between a movable component (active element) and a local electrode (gate). The capacitive attraction force F_e will compete with the elastic restoration force F_m and determines whether the active element can reach the gate (pull-in) and create electrical connections. However, the major difference is that this attraction is manually controlled by an external bias applied on the gate (or on the active element), instead of being spontaneous. Fortunately, we can use the similar capacitive force calculations to find the threshold "pull-in" voltage V_{pi}.

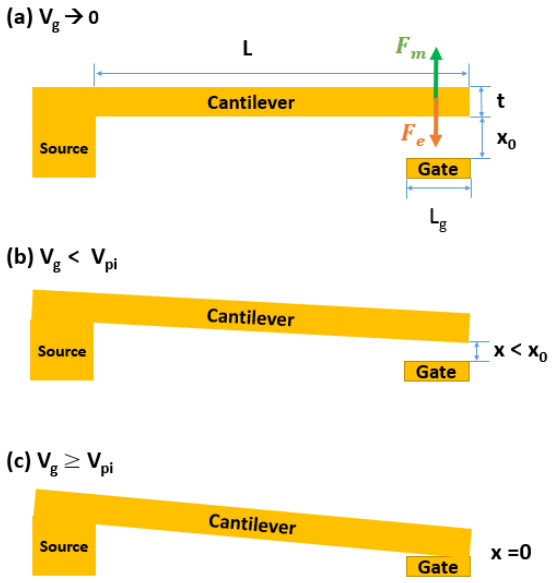

Figure 5.7: Schematic diagram of the pull-in process for a single-anchor metallic nano-cantilever for (a) no cantilever movement (b) partial attraction (c) complete pull-in. The cantilever beam has length L, thickness t, width W. The gate electrode has length L_g and the same width W. The distance between the cantilever tip and the gate electrode is denoted by x, with an initial air gap x_0.

The schematic diagram in Figure 5.7 describes how a nano-cantilever reaches pull-in condition with increasing gate bias. In this setup, the cantilever is connected to the source electrode (grounded), and a gate bias V_g is applied to the gate electrode. Depending on the magnitude of V_g, there are three distinct stages: (a) for a very small gate bias ($V_g \approx 0$V), the capacitive force F_e generated near the tip of the cantilever is trivial and is quickly balanced by the elastic restoration force F_m; (b) gor gate bias less than the pull in voltage ($V_g < V_{pi}$), the cantilever is attracted but the attraction force is still insufficient to bend it all the way to the gate. The capacitive force F_e is again equal to the mechanical force F_m before reaching a critical point, where F_e starts to rise faster than the increment in F_m as the distance "x" between gate and cantilever continues to decrease; (c) when gate bias exceeds a threshold value ($V_g \geq V_{pi}$), the cantilever collapse onto the gate and forms an electrical connection. Currents will start to flow from the source to the drain.

To calculate the threshold (pull-in) voltage, we need to first find F_e and F_m. This time, the capacitive force can be calculated by modeling the gate electrode and the tip of the cantilever into two parallel plates, with length L_g and width W; and the elastic force at tip displacement ($\Delta x = x_0 - x$) is simplified as $F_m = k\,(x_0 - x)$, where k is the spring constant of the suspending beam. The related force balance equation without external forces is then [69]:

$$\frac{W L_g \epsilon_{\text{gap}} {V_g}^2}{2x^2} = k(x_0 - x) \tag{5.1}$$

where L_g and W are the length and width of the gate; ϵ_{gap} is the dielectric constant in the air gap between the cantilever and the gate.

Stability analysis [70] in Figure (5.8) indicates that the critical point for "pull-in" voltage occurs when the cantilever tip displacement equals to 1/3 of the initial air gap thickness ($\Delta x = \frac{1}{3}\, x_0$), which leads to $x = \frac{2}{3}\, x_0$. At this point, the capacitive force is equal to the elastic force. But when $x > \frac{2}{3}\, x_0$, the attraction force will grow faster than its rival – the linearly increasing restoration force, leading to an inevitable "pull-in" between the cantilever and the gate. This result is also confirmed by our simulation for spontaneous attraction in chapter 2, Figure 2.6.

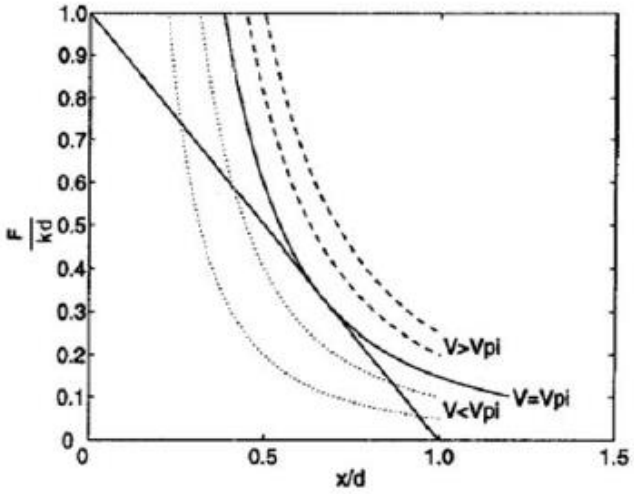

Figure 5.8: Normalized restoring and electrostatic forces vs. normalized electrode separation [70].

Accordingly, the pull-in voltage for a NEM-switch can be calculated form equation (5.1) by setting $x = \frac{2}{3}\, x_0$:

$$V_{\text{pi}} = \sqrt{\frac{8k{x_0}^3}{27\epsilon_{\text{gap}} W L_g}} \tag{5.2}$$

where k is the string constant. For a cantilever fixed at one end with a point force at the tip, the string constant k_1 is calculated as

$$k_1 = \frac{E\ W\ t^3}{4L^3} \tag{5.3}$$

where E is the Young's modulus of the material, and W, t, L are the width, thickness, and length of the suspending cantilever.

The pull-in voltage for a nano-cantilever is then:

$$V_{\text{pi-cantilever}} = \sqrt{\frac{2\ E\ t^3\ {x_0}^3}{27\ \epsilon_{\text{gap}}\ L^3\ L_g}} \tag{5.4}$$

From this equation, we see that the pull-in voltage is most sensitive to the thickness and length of the suspending beam (which determine the mechanical stiffness of the beam), as well as the air gap height between the beam and the gate electrode (which defines the magnitude of electrostatic interaction). Other parameters, such as the Young's modulus E and dielectric constant ϵ_{gap}, are representing the material properties for the beam and the dielectrics between the gap. Remarkably, width W has no influence on the pull-in voltage in this equation.

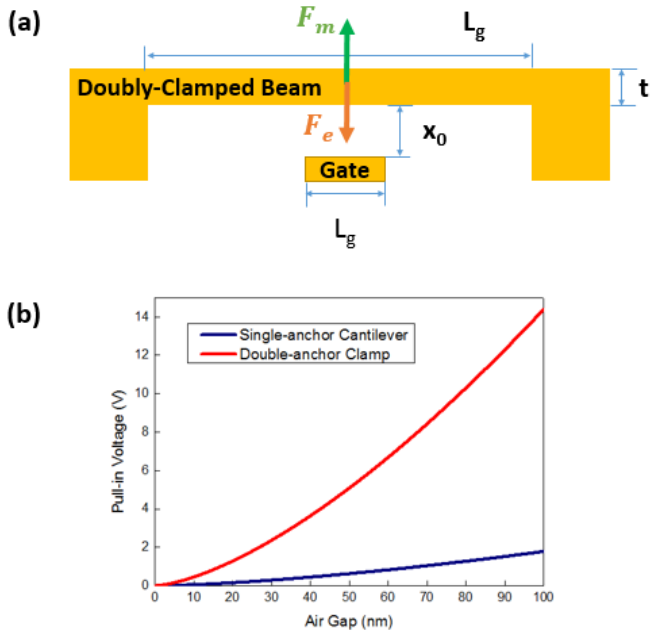

Figure 5.9: (a) Schematics diagram for the doubly-clamped suspending beam. (b) Simulation of the pull-in voltages versus initial air gap thickness, comparing both single-anchor cantilever and doubly-clamped beam structures with the same dimension: 60nm thick titanium beam with Young's Modulus 110.3Gpa, beam length 5 μm, width 500nm; gate length 500nm, width 500nm. Air is the medium between the gap.

The pull-in voltage equation (5.2) is also applicable to the doubly-clamped structure (Figure 5.9a), with only the modification in spring constant k:

$$k_2 = \frac{\pi^4 E w t^3}{6L^3} \tag{5.3}$$

This is based on a simplified model in which a point force is applied in the center of the suspending beam, neglecting the residue stress. Then the pull-in voltage for the doubly-anchor beam is calculated as

$$V_{\text{pi-clamp}} = \sqrt{\frac{4\pi^4 E t^3 {x_0}^3}{81\epsilon_{\text{gap}} L^3 L_g}} \tag{5.4}$$

The comparison between the pull-in voltages of single-anchor cantilever and doubly-clamped beam with the same structure dimension is displayed in Figure 5.9b. Both beams consist of 60nm thick titanium with Young's Modulus 110.3Gpa, with beam length 5 μm, width 500nm; gate length 500nm, width 500nm. The initial air gap varies from 0nm to 100nm in this plot. Obviously the doubly-clamped structure is more resistant to pull-in at lower gate bias, but its better mechanical stiffness improves the device reliability with larger elastic restoration force to fight the adhesion at beam-gate contact surface.

3-terminal NEM-switches with both cantilever and doubly-clamped structures are later fabricated by gray-EBL with their electrical properties measured by semiconductor analyzers. Designs with various materials and geometry are also tested to improve the device performance and reliability. Details for these real devices will be discussed in the following sections.

5.3 Single-Cantilever NEM-switches

First, we fabricated the single-cantilever type of NEM-switches. These devices feature very low pull-in voltages at the cost of reliability. With grayscale e-beam lithography, the fabrication process was quick and straightforward, and specific modifications to the beam structure can also be done. In this section, we will explain the fabrication processes, device performance and design improvements for this type of device.

5.3.1 Device Fabrication

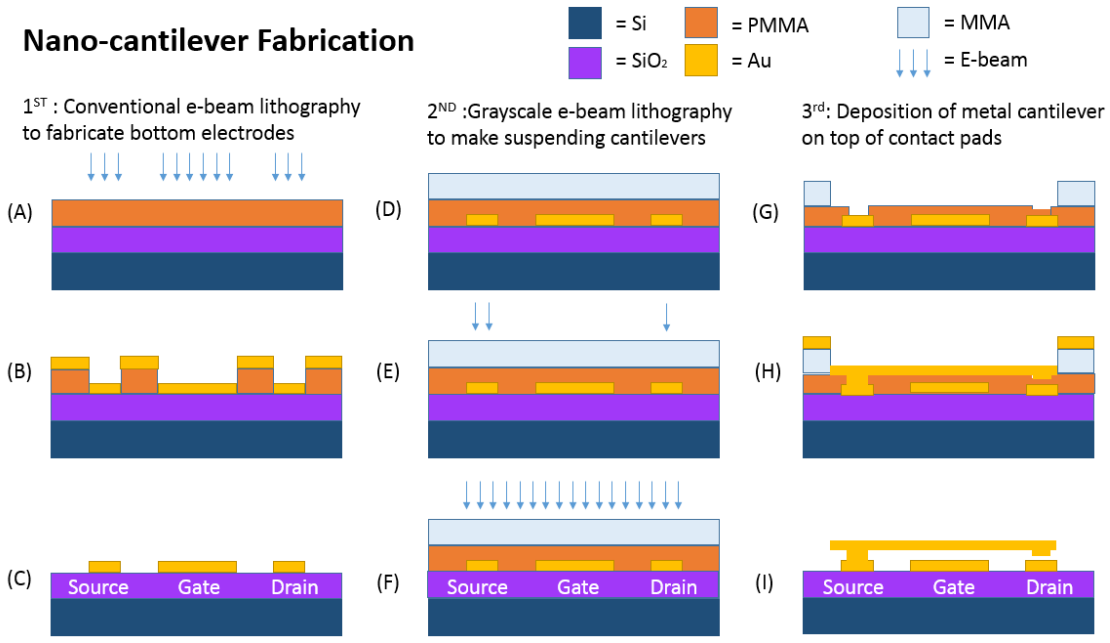

Figure 5.10: Fabrication process for 3-terminal NEM-switches with suspending nano-cantilever by grayscale electron beam (gray-EBL) lithography. (A-C) conventional EBL to make contact electrodes: source, gate and drain. (D-F) grayscale lithography with varied e-beam dosage to modified the resists for subsequent suspending beam deposition. (G-I) Metal thin films are then deposited on the developed resist and lift-off was done with critical point drying (CPD) to form the suspending cantilever.

The fabrication of single-cantilever type NEM-switch is describe in Figure 5.10. Significantly, only two steps of lithography steps are required without the use of any sacrificial dielectrics. The first one is a conventional e-beam lithography to build 3-terminal electrodes under the subsequent suspending beam. To begin with, n-type silicon substrates (100) with 100nm thermal silicon oxide are cleaned with acetone, isopropyl alcohol (IPA), and DI water for 5 min with sonication. Next, 200 nm thick methyl methacrylate (MMA) layer and 200 nm thick Polymethyl methacrylate (PMMA)

e-beam resist layer are deposited on silicon wafer by spin-coating and baked on a hot plate at 180 ˚C for 90 s and 120 s, respectively. After development in a 3:1 mixed solution of isopropyl alcohol (IPA) and methyl isobutyl ketone (MIBK) for 120 s, 50nm Au + Cr metal thin film is deposited by JEOL 6400 SEM/NPGS e-beam lithography system. With lift-off in acetone, the PMMA+MMA resist layer is removed, leaving three electrodes (source, gate and drain) on the silicon oxide surface.

The interesting part takes place in the subsequent grayscale lithography. First, 350nm MMA and 150nm PMMA are spin-coated on the wafer with contact electrodes and baked at 180 ˚C, both for 120s. Afterwards, controlled e-beam doses are given to different areas on the substrate: a heavy dose is assigned to the source electrode to fully penetrate the resist layer here, for the connection between source and suspending cantilever; a medium dose is applied in the center beam region to ensure partial exposure of the resist and prepare for depositing suspending structures; finally, a very light dose is added to the drain area, making the dose at beam tip slightly larger than the average dose in the middle. In this way, a “dip” below the suspending beam can be created. The exposed resist is then developed in MIBK:IPA 1:3 solution for 60s, with a 60 nm thick Ti film deposited with the e-beam evaporator. Finally, after lift-off in acetone with critical point drying (CPD), a suspending cantilever with a probing “dip” above the drain electrode is formed. This “dip” is made by the extra light dose at the cantilever tip, such that during the pull-in process, it will prevent the gate electrode from touching the beam by establishing the electrical connection only between the drain electrode and the “dip”. It not only avoids gate leakage, but also reduces the effective contact area between the

cantilever and the electrodes, leading to less adhesion force and lower chance of operational failure due to stiction. The electrical performance of this device will be discussed in the next section.

5.3.2 Electrical Characterization

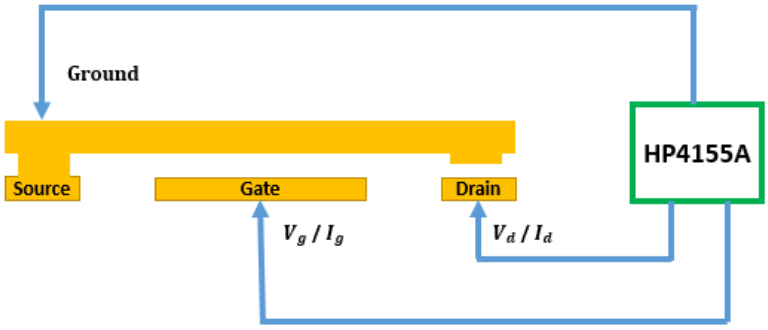

Figure 5.11: Equipment setup of electrical measurement for single cantilever NEM-switch. The device is connected with semiconductor analyzer (HP4155) in a probe station. The source electrode is grounded, the gate electrode is biased with V_g to attract the suspending beam, and the drain has a small bias V_d to test the electrical connection (I_d) at "ON" (pull-in) status.

The setup of electrical characterization for a single cantilever NEM-switch is depicted in Figure 5.11. Inside a probe station, the NEM-device is connected with semiconductor analyzer HP4155 to control the applied voltage on each electrode and measure all currents. First, the source electrode, together with the suspending beam, is set to zero voltage (ground) for charge neutrality on the cantilever. Second, the gate is biased with V_g to create an electric field between gate and the cantilever. The consequent capacitive attraction will "pull-in" the beam if $V_g \geq V_{pi}$(threshold pull-in voltage).Then the tip of the cantilever will touch the drain electrode and signify the "ON"

state. Notice that the probing "dip" designed on the cantilever tip will prevent the beam from touching the gate to avoid any gate leakage current I_g. Finally, a small bias V_d is applied on the drain electrode to test electrical connectivity. By sweeping Vg from 0V to higher bias, The change in I_d indicates the transition from "OFF" state to "ON" state at $V_g = V_{pi}$. In this manner we can identify the experimental "pull-in" voltages for the NEM-switch, as well as the contact resistance at ON state. In addition, this drain bias V_d is carefully set to a small value (<50mV) to minimize the electrostatic interaction between the drain and the cantilever. Furthermore, to prevent potential electrostatic damage to the NEM-switch, all the currents (I_d and I_g) are set with a compliance in μA scale

An exemplary side-view SEM image for a 3-terminal single cantilever NEM-switch fabricated with gray-EBL is given in Figure 5.12(a). The 60nm Ti cantilever beam is suspending above both gate and drain electrodes, with a smaller air gap at the drain (45 nm) and a larger air gap at the gate (108nm).

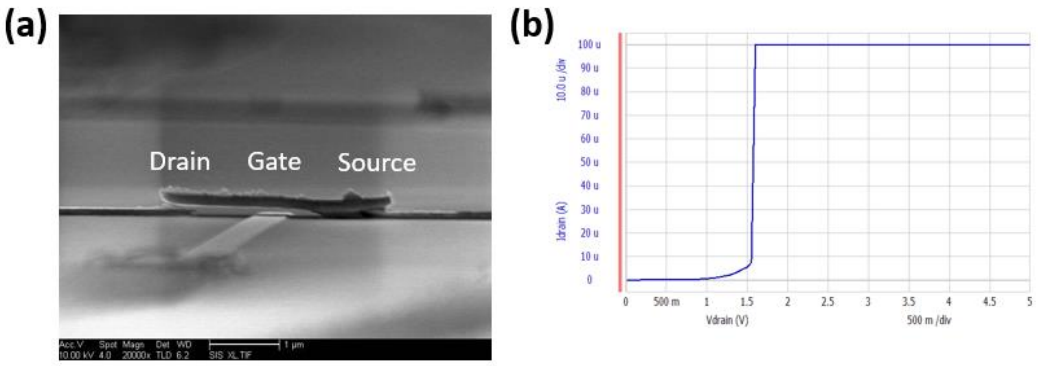

Figure 5.12: (a) Side-view SEM image of 3-terminal single-cantilever NEM-switch with 50nm Cr+Au bottom electrodes. The gate electrode has width 400nm. Ti suspending beam has thickness 60nm, width 400nm and length 2.3 μm. (b) Experimental $I_{ds} - V_g$ plot showing the measured "pull-in" behavior of the NEM-switch at $V_g = V_{pi} = 1.6V$. The scale bar in the SEM image is 1 μm.

This device switches at an impressive low pull-in voltage of $V_{pi} = 1.57V$, measured from the $I_{ds} - V_g$ plot in Figure 5.12b. In the setup, the drain is biased at a small voltage 50mV, and the source (beam) is grounded. As the gate voltage V_g sweeps from 0V to 5V, the drain current I_d exhibits an abrupt increase at $V_g = V_{pi} = 1.6V$. This is when the cantilever touches the beam and forms a circuit between source and drain. Notice that right before pull-in ($V_g < V_{pi}$), there is a slight gradual increase in I_{ds} probably due to the tunneling currents when the beam and the drain are in proximity. For gate voltage exceeding the pull-in threshold ($V_g > V_{pi}$), the switch stays "ON" as the electrostatic force and the dispersion forces keeps the mechanical connection. Considering the good conductivity between the Ti beam and Au electrode (from this graph, contact resistance $R < 500\Omega$), a 100 μA compliance is applied on I_{ds} to protect the NEM-switch from electrostatic damage or over-heating due to the large

current. The simulated pull-in voltage for this device gives $V_{g-simulation} = 1.82V$, which is close to the experimental value of 1.57V. The reason for the disparity could be that the actual Young's modulus for the nano-beam is lower than the bulk material value used in the simulation due to its size and geometry. Also, in the simplified model other forces such as gravity and the small attraction between the drain and the cantilever are neglected.

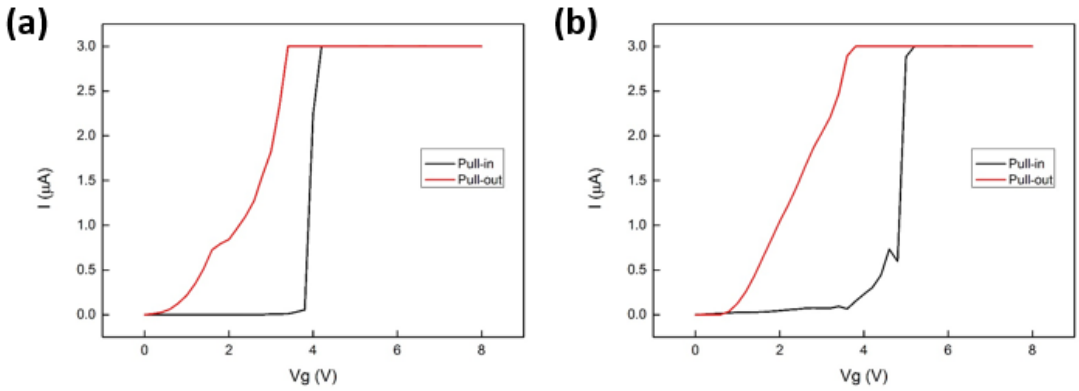

Figure 5.13: $I_{ds} - V_g$ plots for another single cantilever NEM-switch at (a) first run, $V_{pi-1} = 3.9\,V$ (b) second run, $V_{pi-2} = 5.0\,V$. The black and red curves indicate the pull-in (V_{pi} sweeping up from 0V to 8V) and pull-out (V_{pi} sweeping down from 8V to 0V) behaviors respectively. Source electrode is grounded and drain electrode has a small bias $V_d = 50\,mV$. 3μA current compliance is set to avoid electrostatic and thermal damages to the NEM-switch due to large "on" currents.

Single-cantilever NEM-switch has the benefit of lower pull-in voltages, but at the cost of reliability. Figure 5.13 shows the $I_{ds} - V_g$ curves of another cantilever type device at its 1st and 2nd runs. The red and black curves indicate the changes in I_{ds} at "pull-in" and "pull-out". On one hand, a shift occurs in the pull-in voltages from $V_{pi-1} = 3.9\,V$ to $V_{pi-2} = 5.0\,V$, which indicates a change in the air gaps between the cantilever beam and the electrodes during 1st and 2nd runs. After the first "pull-out", the

beam did not return to its original position, but most likely switched to a higher location with a slightly larger air gap that requires larger gate bias to overcome the elastic force at greater deflection. On the other hand, the "pull-out" Id curve (black) shows non-volatile switching behavior that is a gradual decrease instead of an abrupt change. This implies that a temporary stiction occurs after pull-in, so the contact at drain is not immediately released as V_g drops below V_{pi}. However, fortunately this stiction is non-permanent and the device has functioned again.

5.3.3 Reliability Issues

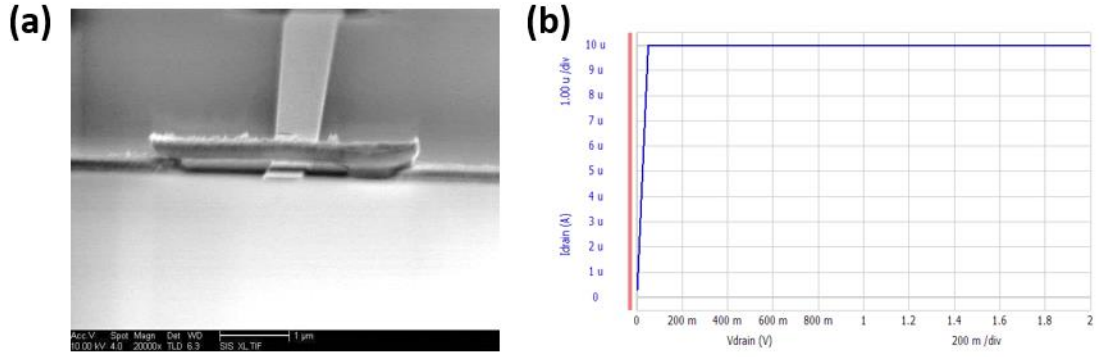

Figure 5.14: (a) SEM image and (b) $I_{ds} - V_g$ showing a single cantilever NEM-switch with permanent stiction. The scale bar in the SEM image is 1 μm.

Permanent stiction is a failure mode for NEM-switch that occasionally happen during fabrication or operation. An exemplary SEM image for a single cantilever NEM-switch with permanent stiction at the drain is shown in Figure 5.14a. After running for a few cycles, the tip of the cantilever adhered to the drain electrode, and this device ceased to work with its $I_{ds} - V_g$ plot (Figure 5.15b) displaying a "short-circuit"

behavior: the device is always in the "ON" state like a resistor and I_{ds} quickly reaches the compliance current 10 μA. Overall, due to its inferior mechanical stiffness, the cantilever type NEM-switch is more vulnerable to structural deformation or stiction during operations.

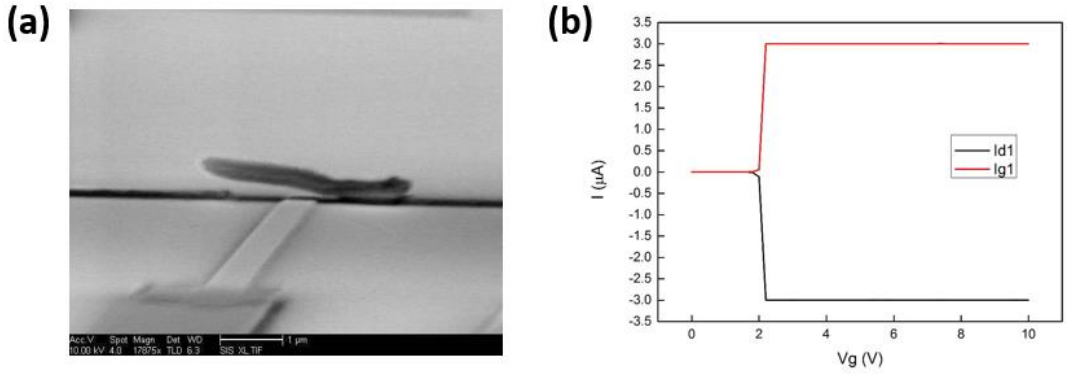

Figure 5.15: (a) SEM image and (b) $I_{ds} - V_g$ showing a single cantilever NEM-switch with gate leakage. The scale bar in the SEM image is 1 μm.

Another reliability concern is the gate leakage in single-cantilever NEM-switches. By design, with a probing "dip" fabricated with gray-EBL at the end of the suspending beam, the device should be able to avoid gate leakage at "pull-in" when the drain electrode touches the beam. Nevertheless, devices without such a structure, such as the one in Figure 5.15a, will have gate in contact with the beam first during "pull-in", and will form an electrical connection from gate to drain. The shape of this cantilever is possibly created by the stress releasing in the beam during fabrication. The observed gate leakage I_g dominates over I_{ds} when the drain is only set to a very small bias 50mV. Therefore, in Figure 5.15b the drain current almost entirely comes from the gate

leakage. However, both stiction and gate leakage can be resolved with improved design and more careful fabrication with gray-EBL.

5.4 Doubly-clamped beam NEM-switches

The 3-terimal single-cantilever NEM-switches generally feature lower pull-in voltage and low power consumption during switching, but with a cost of reliability. In comparison, the doubly-clamped beam structure will provide better mechanical properties of the suspending beam to improve the reliability. We will discuss the fabrication and performance for multiple designs of doubly-clamped beam NEM-devices in this section.

5.4.1 Device Fabrication

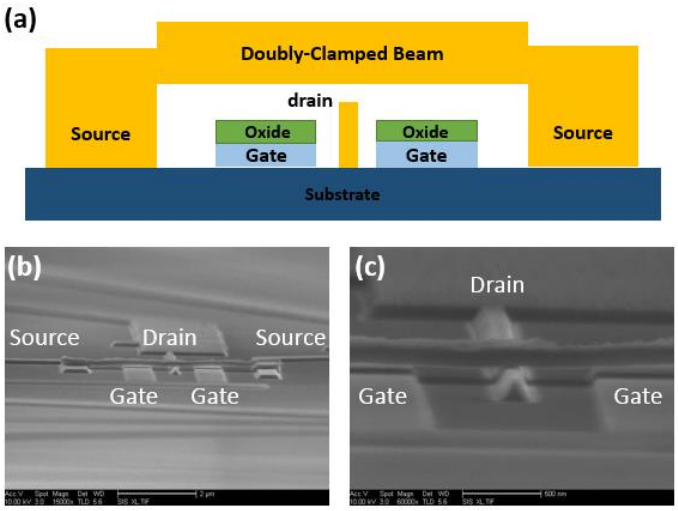

Figure 5.16: (a) Schematics of a NEM-switch with doubly-clamped beam. (b) Side-view SEM image showing a NEM-switch fabricated with gray-EBL. (c) Zoom-in SEM image near the center drain electrode. The air gap height above each electrode is: 16 nm (drain), 70 nm (left gate), 83 nm (right gate). The scale bars are 2 μm and 500 nm.

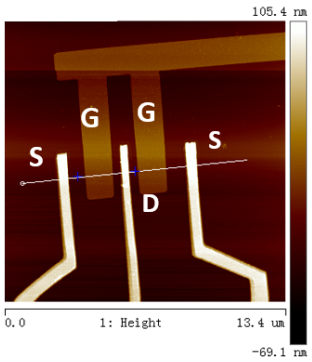

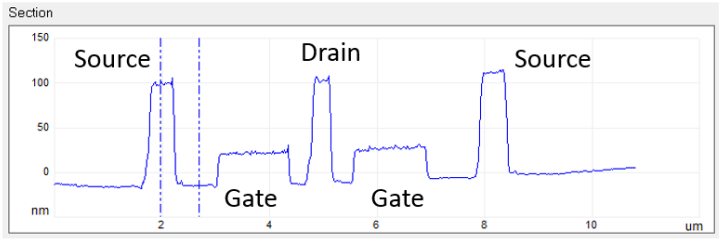

	Source	Drain	Gate
Thickness	112nm	113nm	34nm

Figure 5.17: AFM 2-D topography and thickness measurement of Source/Drain/Gate electrodes.

The fabrication process of a doubly-clamped beam NEM-switch is very similar to that of the single cantilever type, but with a few modifications. First, two gate electrodes on both side of the drain are patterned with conventional e-beam lithography, and 25 nm Cr + Au layer is deposited with an e-beam evaporator. Next, a thin layer of oxide (10nm thick HfO_2) is grown on top of the gate by atomic-layer-deposition (ALD) to prevent gate leakage. The source and drain electrodes are then fabricated by another conventional e-beam lithography step, and deposited with thicker metal (110nm Cr + Au). Finally, a 50nm-thick Ti suspending beam is created on top of the electrodes by grayscale e-beam lithography and e-beam evaporator.

There are several important changes in the doubly-clamped beam structure (Figure 5.16a) to improve the device performance and reliability. To begin with, there are two interconnecting gate electrodes (instead of one compared with single cantilever type) with greater gate width to strengthen the electrostatic attraction and reduce pull-in voltage. Second, the length of the suspending beam can be increased from 2-3 μm to 4-6 um thanks to the better mechanical stiffness. Third, the total thickness of gate

electrodes (including the oxide layers) are designed to be smaller than that of the source/drain electrodes. In this fashion, a smaller air gap can be made above the drain to ensure that the beam will not touch the gate first at pull-in. An AFM measurement on the contact electrodes (Figure 5.17) confirms that the gate indeed has much lower height than the drain. Moreover, the additional gate dielectric serves as another safeguard against the gate leakage, just in case that the suspending beam accidentally collapses on the gate by very large attraction forces. Lastly, to overcome the stiction at "ON" state, the width of the drain is minimized to reduce the contact area and hence the adhesion forces.

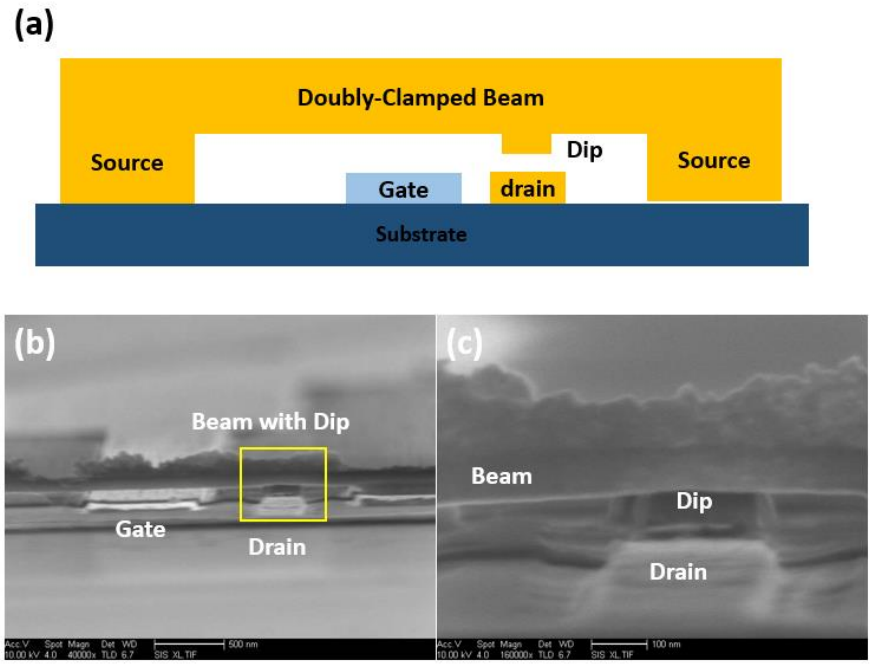

Figure 5.18: Another design of NEM-switch with doubly-clamped beam, with the gate in the middle and a "dip" on the beam near the drain electrode. (a) Schematics. (b) Side-view SEM image showing such a NEM-switch fabricated with gray-EBL. (c) Zoom-in on the drain electrode. A dip on the beam is clearly visible and is suspending above the drain. The air gap height above each electrodes is: 20 nm (drain), 100 nm (gate). The scale bars are 500 nm and 100 nm.

With the benefits of gray-EBL, there is a second strategy to fight gate leakage by preventing gate-beam contact. Figure 5.18 shows another type of NEM-switch with doubly-clamped beam. In this structure, there is only one gate electrode in the center to improve the effectiveness of attraction, and the suspending beam has a "dip" created by extra dose in gray-EBL to reduce the air gap above the drain. From the SEM images we can clearly spot a suspending "dip" formed below the suspending beam, while still maintaining an air gap of 20nm above the drain. In comparison, the air gap above the gate is 100nm. This technique requires very precise control on the e-beam doses but may reduce the fabrication from 3 lithography steps from our 1st type of doubly-clamped NEM-switches to only 2 lithography steps. In the next section, we will demonstrate the electrical properties from both single cantilever and doubly-clamped beam NEM-switches.

5.4.2 Electrical Characterization

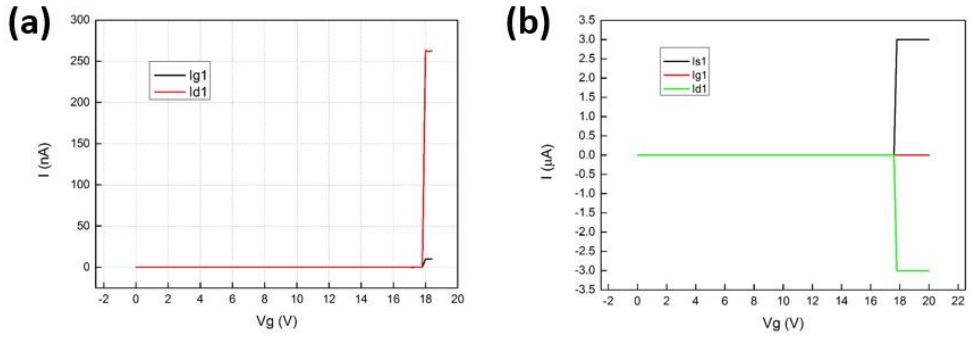

Figure 5.19: $I_{ds} - V_g$ plots for doubly-clamped beam NEM-switch for (a) the first type of device shown in Figure 5.15, $V_{pi} = 17.9\,V$ (b) the second type of NEM-switch, $V_{pi} = 17.8V$. The currents from gate, drain and source are indicated in each plot by different colors and there is no apparent gate leakage. The current compliance for each device is 270 nA and 3 μA respectively.

With the same setup of probe station and semiconductor analyzer HP4155 to the contact electrodes (Figure 5.11), the doubly-clamped beam NEM-switch shows a different $I_{ds} - V_g$ plots in the pull-in process. Although some pull-in voltage may increase dramatically to $V_{pi} = 17.8\,V$ for the double-clamped beam structure compared to the single cantilever type (which agrees with the simulation result in Figure 5.9), there is no significant gate leakage any more with the improvements in structural design and the additional HfO_2 layer on the gate electrode (Figure 5.19). The current of drain electrode solely comes from the source electrode, with a small $V_{ds} = 50\,mV$. It is also evident that for both types of doubly-clamped structure with similar air gaps above the gate, the pull-in voltages are similar and consistent.

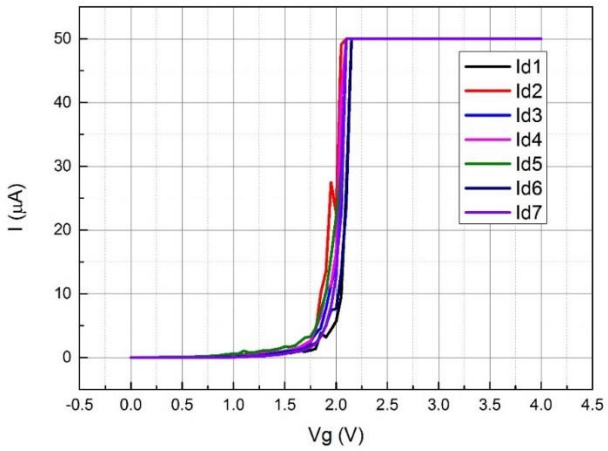

Figure 5.20: $I_{ds} - V_g$ plots for a doubly-clamped beam NEM-switch running through 7 consecutive sweeps. The pull-in voltage is consistently around 2.0 V without any stiction. Current compliance is set at 50 μA.

Furthermore, the stiction issue is also solved with higher mechanical stiffness in the doubly-clamped structure. Figure 5.20 shows the $I_{ds} - V_g$ for one of the best

devices fabricated with gray-EBL. This doubly-clamped beam NEM-switch turns "ON" around a consistent pull-in voltage $V_{pi} = 2\,V$ for 7 consecutive runs, and no stiction or operational failure was observed in the process. The lower pull-in voltage was achieved by minimizing the air gap on the gate. This improved repeatability renders the doubly-clamped beam a more reliable structure for NEM-switch applications.

5.5 Outlook: Nano-Electro-Mechanical Field Effect Transistor (NEMFET) with Semiconductor Nanowires

The grayscale electron-beam lithography (EBL) is proven to be very effective in constructing low-voltage 3-terminal NEM-switches. As demonstrated in Chapter 4, this technique has the potential of fabricating suspending nanostructures with various geometries and controlled air gaps, and it is more compatible with other semiconductor devices because it does not require aggressive fabrication processes such as the etching of dielectric sacrificial layers. Therefore, this method can be readily extended into the assembly of other advanced semiconductor devices, such as the Nano-Electro-Mechanical Field Effect Transistor (NEMFET). Here, with some preliminary fabrication results, we discuss the prospective application of gray-EBL in building a NEMFET with suspending metal gates above a local semiconductor nanowire. This type of device is also previously demonstrated by our group to have near-zero sub-threshold swing and a small switching window less than 2V [71].

5.5.1 Introduction

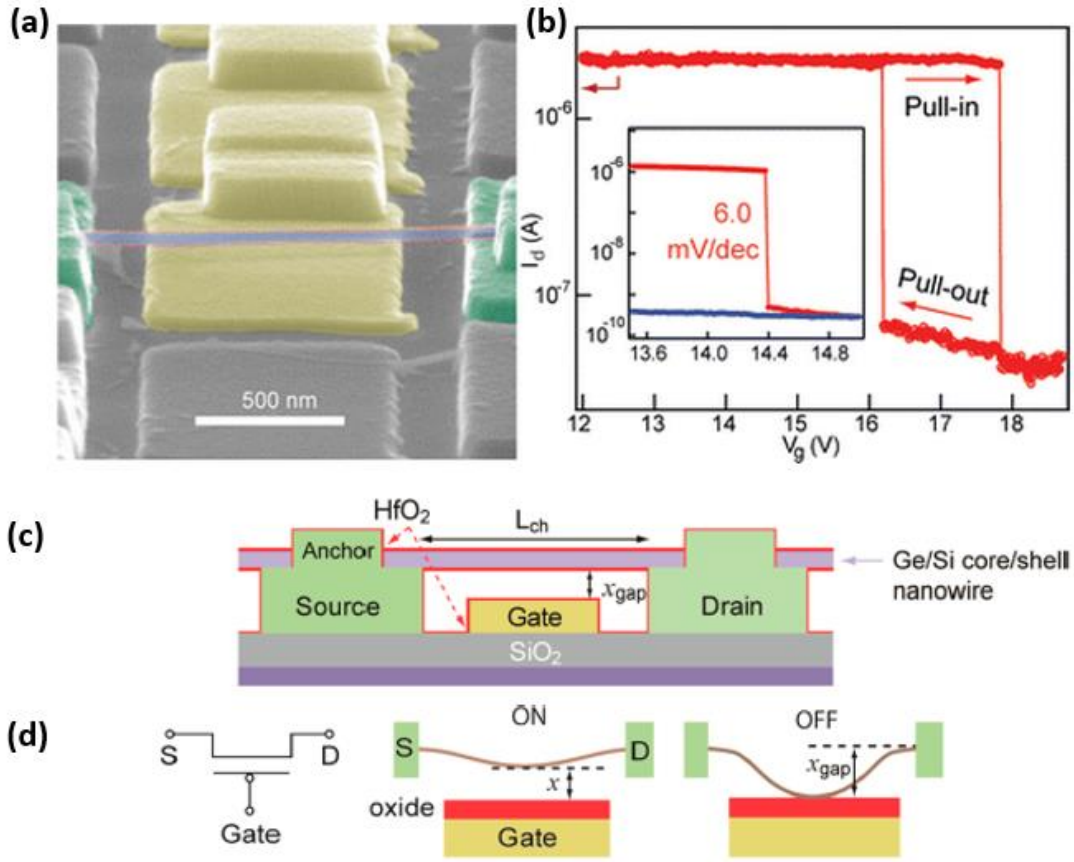

Figure 5.21: (a) Side-view SEM image of a Nano-Electro-Mechanical Field Effect Transistor (NEMFET) with a local metal gate (yellow) and a suspending nanowire channel (blue) connected to source/drain (green). The scale bar is 500 nm. (b) $I_d - V_g$ plot showing the pull-in an pull-out performance of this device. The intersect shows that during switching the sub-threshold swing can be as small as 6 mV/dec. (c) Side-view schematics of the NEMFET. (d) Schematics showing the working principle.

The Nano-Electro-Mechanical Field Effect Transistor (NEMFET) is a combination of field effect transistors (FET) and nano-electro-mechanical-systems (NEMS). Unlike the structure in a conventional MOSFET, the gate electrode in a NEMFET is separated from the FET channel with an air gap, and they only connect

through mechanical attachment when the gate is biased with sufficient "pull-in" voltage. Therefore, the gating effect on the channel only occurs at the sudden "pull-in", leading to a steep change for the current in the FET channel. On the other hand, when the gate bias is decreased, the gate will also have a rapid release from the channel, terminating the gate modulation at the same "pull-out" moment. As a result, the shifts between the "ON" or "OFF" states are both very fast and abrupt, leading to a near-zero sub-threshold swing that breaks the theoretical limit of 60 mV/dec in a MOSFET.

In previous research from our group [71], a NEMFET is built with local metal gate and a suspending Ge/Si core/shell nanowire channel (Figure 5.21). In this device, the nanowire serves as the FET channel with both ends anchored to the taller source/drain electrodes. A gate electrode with smaller thickness lies below the suspending nanowire, and a thin layer of HfO_2 is deposited with ALD to prevent gate leakage current. The p-type Ge/Si core/shell nanowire is very conductive and turns off with positive gate bias. Thus at the positive pull-in voltage V_{pi}, the nanowire is attracted by the electrostatic force onto the gate, and is immediately "turned OFF" by the gating effect, with a subthreshold swing as small as 6 mV/dec. As the gate bias sweeps down, a "pull-out" behavior occurs and the nanowire "turns ON" by returning to its suspending status. The switching window between "pull-in" and "pull-out" is remarkably small (less than 2V). Therefore low power device operation is possible by fixing the reference voltage level of the system slightly below the pull-out voltage.

Motivated by this research, we consider the possibility of applying the gray-EBL technique to construct a similar NEMFET device, with simplified fabrication processes

and greatly improved yield. We will next present the design with gray-EBL and preliminary fabrication results

5.5.2 Design of NEMFET with nanowires channel using Gray-EBL

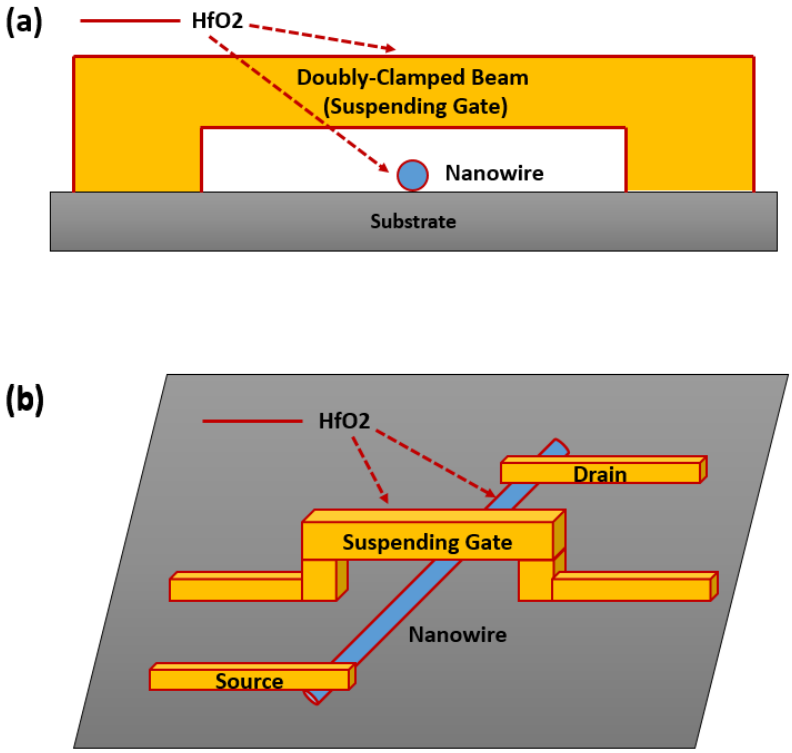

Figure 5.22: Schematics of gray-EBL fabricated Nano-Electro-Mechanical Field Effect Transistor (NEMFET) with suspending gate and a local nanowire channel. (a) Side-view showing the doubly-clamped beam as the suspending gate on top of the nanowire. (b) Titled-view showing the source and drain electrode of the nanowire FET, and gate above the nanowire channel.

A similar structure of our doubly-clamped beam NEM-switch is applied to the construction of NEMFET with nanowire channel (Figure 5.22). The detailed fabrication

processes are as following: first, Ge/Si core-shell nanowires (csNWs) are synthesized in low-pressure-chemical-vapor-deposition (LPCVD), and dispersed onto Si substrate with 100nm thermal SiO_2 layer. Next, source and drain electrodes are patterned at both ends of the nanowire with conventional EBL, and deposited with Cr + Au by an e-beam evaporator. Afterwards, a doubly-clamped suspending metal gate is fabricated with gray-EBL over a nanowire lying on the substrate. Finally, a thin-layer of HfO_2 is deposited by ALD on both surfaces of nanowire and gate electrode.

By applying external bias on the suspending gate, there will be capacitive attraction forces between the gate and the nanowires, resulting in the "pull-in" condition. Once the bias is removed, the metal gate will easily "pull-out" from the nanowire due to the stronger mechanical stiffness of doubly-clamped beam. The major difference between this design and the previously introduced NEM-FET structure is that the nanowires are now local on the substrate, with the metal gate electrode suspending instead. In comparison, the previous design has the bottom electrodes are first fabricated and nanowires are then dispersed onto them. However the position of nanowires are not guaranteed to be over the channels across the source/drain. The randomness in nanowire dispersion significantly reduces the yield of fabrication. Fortunately, with the new design we are able to locate any nanowire on the substrate with SEM and fabricate suspending gate over each one of them to improve the overall yield. In addition, the air gap over each nanowire can be readily customized by varying the e-beam doses, giving us more freedom to control the switching behavior.

5.5.3 Fabrication and Electrical Characterization for Ge/Si Nanowire FET

Before constructing the suspending metal gate using gray-EBL, the nanowire FET is fabricated with LPCVD, conventional EBL and e-beam evaporator. First, Ge/Si Core/Shell nanowires (csNWs) are synthesized by chemical vapor deposition process using gold nanoparticles with 15-40nm diameter as catalysts (gold colloids from Ted Pella). The Ge core is grown on Si substrates with 2% of GeH4 in hydrogen precursor gas at 290˚C and 300 torr for 2 hours. The Si shell is deposited immediately using 2% SiH_4 in hydrogen as precursor gas at 465˚C, 100 torr for 10 min. The as-made csNWs are then immersed in IPA solution and sonicated for further dispersion process. The csNWs-IPA mixture solution is drop-casted onto the target Si substrate with 100 nm thermal SiO_2 layer on top. After drying in air, each NW is located under SEM of the JOEL 6400 SEM/NPGS e-beam lithography system, and source/drain electrodes are patterned at both ends of the NW with conventional EBL. Finally, 50nm thick Ni is patterned and deposited to make the source/drain contact electrodes. The material of Ni is chosen to match the fermi level of Ge/Si csNWs to ensure Ohmic contact. By biasing the Si substrate as the back gate, the csNW FET is now ready for electrical measurements in a probe station with semiconductor analyzer HP4155.

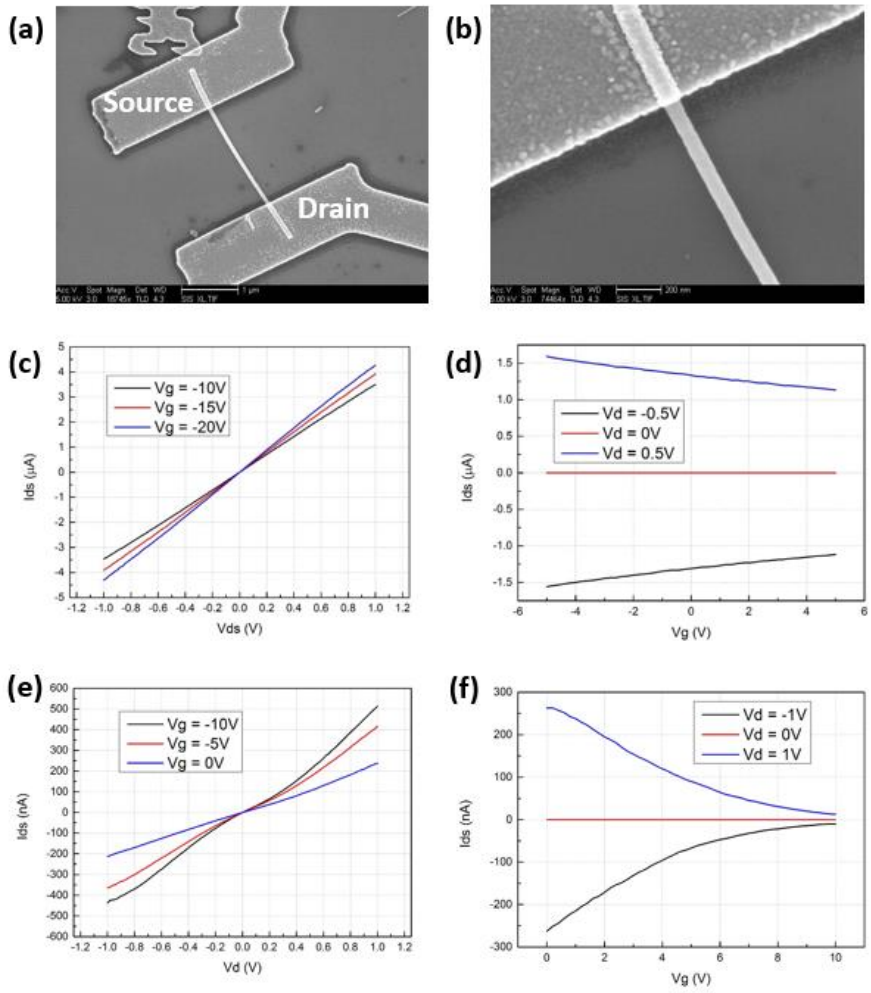

Figure 5.23: (a-b) Overview and zoom-in SEM images for an exemplary Ge/Si csNW FET. The scale bars are 1μm and 200nm. (c-d) $I_{ds} - V_{ds}$ plot and $I_{ds} - V_g$ plot for a more conductive csNW FET (70 nm diameter) at various gate or drain biases shown in the graphs. (e-f) $I_{ds} - V_{ds}$ plot and $I_{ds} - V_g$ plot for a less conductive csNW FET (25 nm diameter) at various gate or drain biases shown in the graphs.

The representative SEM images for a Ge/Si csNW FET are displayed in Figure 5.23(a-b). This particular nanowire in the figure has a diameter of 70 nm, and both of its ends are in good connection with the 50 nm-thick Ni source/drain contacts. These contacts are connected through metal wires to larger pads outside the SEM image for

electrical measurements in a probe station. The diameter of a NW is controlled by the size of gold catalysts used in CVD growth. Our experimental value of NW diameter varies from 20 nm to 80 nm. The FETs based on different sizes of NWs exhibits a wide range of conductivity in electrical measurements. Generally, assuming the same condition of csNW-Ni contact, larger NW diameter leads to lower channel resistance and higher output current. In the $I_{ds} - V_{ds}$ plot (Figure 5.23c) for a csNW FET with larger diameter (70 nm), the output current I_{ds} reaches 3.4 μA at $V_{ds} = 1$ V and back gate bias $V_{g-backgate} = -10$V. Compared with the csNW FET with smaller diameter (25 nm), at the same gate and drain biases its output current is much less at 500 nA (Figure 5.23e).

In addition, it can be seen from the $I_{ds} - V_g$ plots (Figure5.23 d,f) that these NWs exhibits p-type I-V characteristic and could be only turned off ($I_{ds} \rightarrow 0$) at positive gate bias. These devices are typically turned off at back gate bias around 10V, and for a top gate the turn-off voltage is expected to be smaller (<10V). Therefore, to transform these NW FETs into NEMFET, the pull-in voltage of the suspending top gate should be carefully designed to be larger than the "turn-off" voltage. This can be achieved with ease in gray-EBL by varying the doses on the suspending beam region.

5.5.4 Preliminary result of NEMFET with Suspending Metal Top Gate and Ge/Si csNW Channel

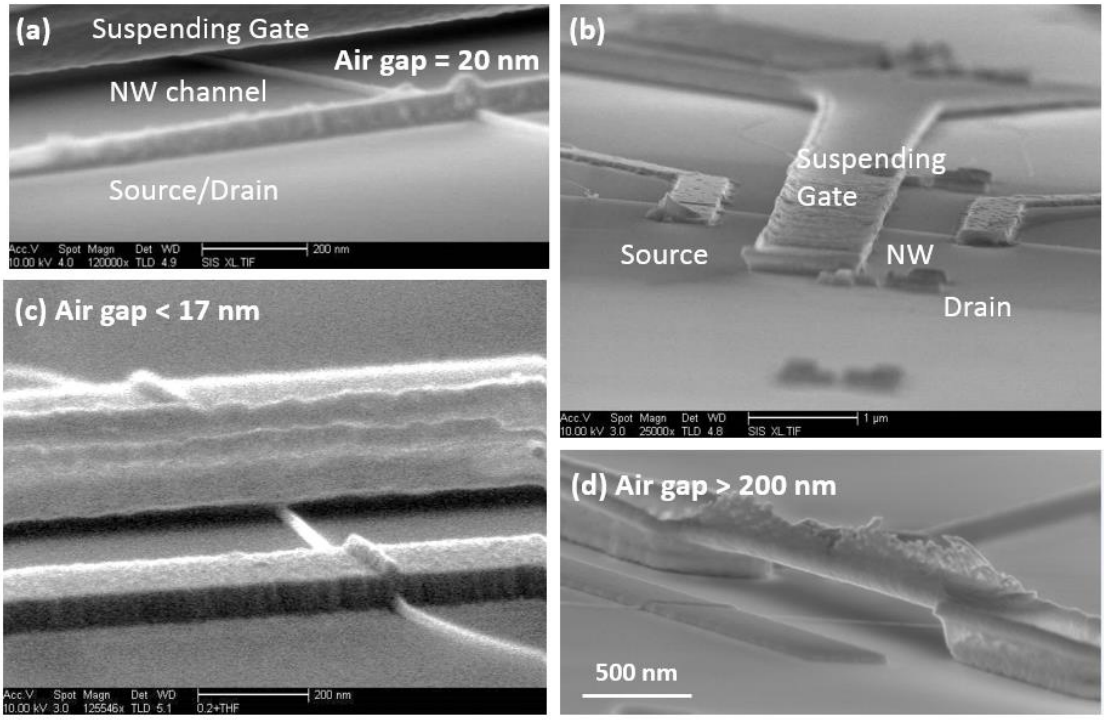

Figure 5.24: Side-view SEM images showing four different NEMFET devices with doubly-clamped suspending beams fabricated by gray- EBL. (a) NEMFET with 50 nm thick Ti beam as gate, 20 nm air gap. (b) 90˚-rotated SEM showing the source/drain and suspending gate in a device with 60 nm thick Cr + Au beam, 50 nm air gap (c) 60 nm thick Ti beam, very small air gap <17 nm. (d) 60 nm thick Ti beam, very large air gap > 200 nm.

Once a NW FET is produced, it takes only one more process of gray-EBL to put a suspending gate over the NW channel and convert it into a NEMFET. The fabrication procedure is identical to that of creating the suspending beam in a NEM-switch, which is discussed in detail in Section 5.3.1 and Section 5.4.1. The only modification is that

after the metal suspending gate is finished, an additional ALD process is commenced to deposit ~10 nm HfO_2 on both nanowire and the gate to prevent gate leakage at their contact during pull-in. A few representative results are shown in Figure 5.24. Here we see four NEMFET structures with different designs in the suspending beams and air gaps between the beam and the nanowire. From the side-view SEMs, impressively the nanowire channel clearly runs through the suspending gate (Figure 5.23b) with adjustable air gaps varying from less than 20 nm (Figure 5.23a, c) to over 200 nm (Figure 5.23d). The structure is proven to be very robust during most sample treatments and intensive electrical measurements.

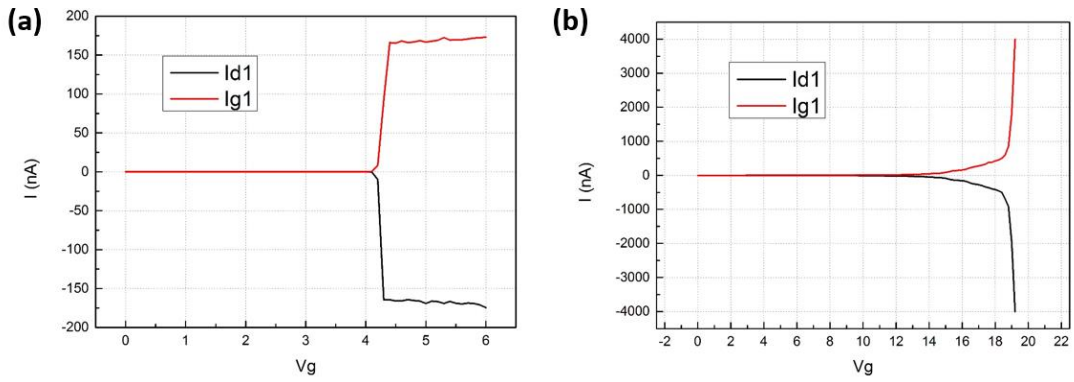

Figure 5.25: Preliminary $I_{ds} - V_g$ test for two NEMFET devices with gate leakage. (a) Pull-in voltage $V_{Pi} = 4.3\,V$, with $V_{ds} = 100\,mV$ and current compliance at 200 nA. (b) Pull-in voltage $V_{Pi} = 19.2\,V$, with $V_{ds} = 100\,mV$ and current compliance at 4 μA.

Switching behavior in these NEMFETs is successfully confirmed in our initial I-V tests. Figure 5.25 represents the performance of two NEMFETs with controllable pull-in voltages as low as $V_{Pi} = 4.3\,V$ and as high as 19.2 V. However, both devices are compromised with gate leakage currents, which is probably caused by insufficient

isolation from the 10nm ALD-grown HfO_2 layer. Further investigations and experiments to resolve this issue is still underway. The final performance without gate leakage is expected to be comparable to the previous type of NEMFET developed in our group.

5.6 Conclusion

In this chapter, we have reviewed the development in NEM-switches and fabricated both single cantilever type and doubly-clamped beam type NEM-switches with grayscale e-beam lithography (gray-EBL). The single cantilever device has lower pull-in voltage as small as 1.6V at the cost of reliability, while the doubly-clamped structure provides better consistency for switching and improved resistance to stiction or gate leakage. At the end, an outlook for perspective NEMFET device fabricated with gray-EBL is discussed. Prototypes of NEMFET with metal suspending gate and Ge/Si Core/Shell nanowire channel are demonstrated in experiments. The suspending gates are successfully made over the nanowires and initial test result confirms the pull-in behavior between them.

5.7 Acknowledgement

Chapter 5, in part, is a reprint of Z. Sun, S. Kwon, J. Xiang, “Low voltage three-terminal nanoelectromechanical switches using grayscale lithography”, to be submitted.

Chapter 6:

AFM characterization of synthetic DNA molecules with site-specific decoration of proteins

6.1 Site-Specifically Arraying Small Molecules or Proteins on DNA

DNA is receiving increasing attention for different in vitro applications ranging from aptamer and DNAzyme evolution[73] to nanomaterial development.[74] The utility of DNA for these applications follows from two unique properties, its template-directed amplification and its predictable structure that, together with site-specific modification, offers unprecedented nanometer scale spatial control that could be used to array small molecules or proteins in specific patterns or spatial relationships. However, current applications fail to take advantage of both of these properties because the product of template directed (i.e., PCR) amplification cannot be site-specifically modified, and site-specifically modified synthetic fragments cannot be PCR amplified. One approach toward circumventing this limitation is rooted in efforts to expand the genetic alphabet,[75] and thus provide unnatural nucleotides with unique functionality as potential sites for site-specific modification within an oligonucleo-ACHTUNGTRENUNGtide.[75e, 76] For example, Hirao and co-workers have used an

unnatural base pair and Click chemistry[77] to site-specifically attach a single small molecule biotin tag or fluorophore to PCR amplified DNA.[78c]

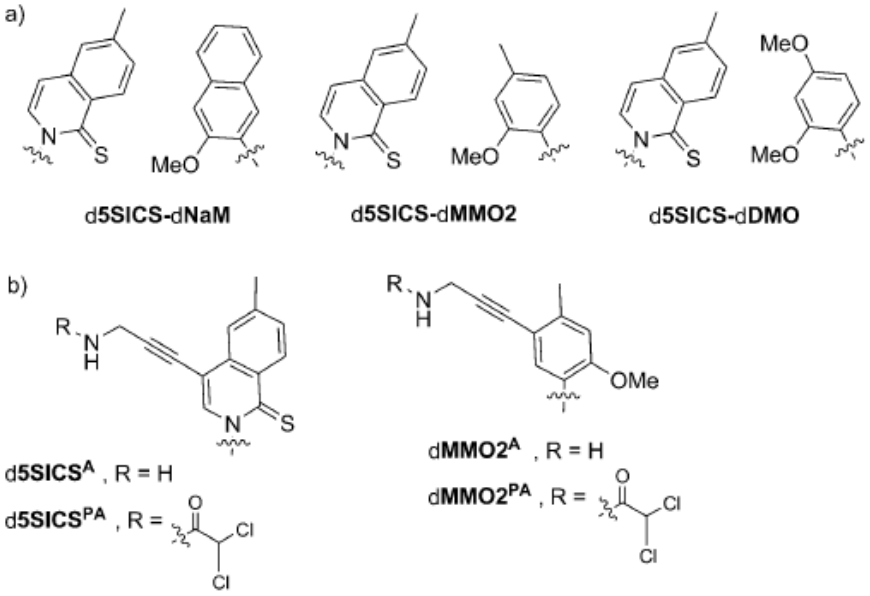

Figure 6.1: a) Parental unnatural base pairs, and b) previously reported linker modified analogues. Sugar and phosphate backbone are omitted for clarity.

As part of an effort to expand the genetic alphabet, the Romesberg group at The Scripps Institute have developed a class of unnatural base pairs formed between d5SICS and either dMMO2, dDMO, or dNaM (Figure 6.1a).[75g] Pairing of these unnatural nucleotides is mediated only by packing and hydrophobic forces; nonetheless, DNA containing them is efficiently PCR amplified[75a,b, 78]and transcribed,[79] and linkers may be attached that allow for further,site-specific modification.[76a] Although it is shown that d5SICS – dNaM is more efficiently replicated and transcribed than d5SICS – dMMO2,[75f,79] early efforts toward linker-derivatized nucleotides focused on d5SICS and dMMO2, in part because they both may be modified at positions

analogous to the C5 position used to attach linkers to the natural pyrimidine triphosphates.[80] A variety of d5SICS and dMMO2 analogues bearing propargyl amine-based linkers were examined and several were identified that allowed for PCR amplification and transcription, and shown to allow for the site-specific modification of the resulting oligonucleotide (Figure 6.1b).[76a] However, the dMMO2 analogues were generally replicated less efficiently than the d5SICS analogues. As part of a continued optimization effort we synthesized dEMO and dFEMO (Figure 6.2), which both possess an ethynyl group as part of their core structure that might also be used for derivatization by Click chemistry.[77] Interestingly, we found that DNA containing either d5SICS – dEMO or d5SICS – dFEMO is more efficiently PCR amplified than DNA containing d5SICS – dMMO2,[81] suggesting that they might provide routes for the efficient production of site-specifically modified DNA.

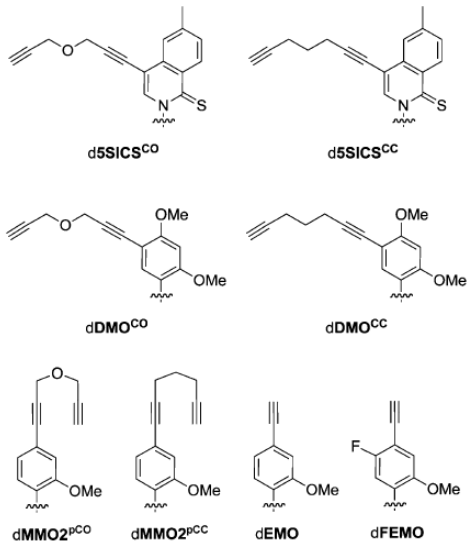

Figure 6.2. Linker modified analogues examined in this study (including previously reported dEMO and dFEMO[9]). Sugar and phosphate backbone are omitted for clarity.

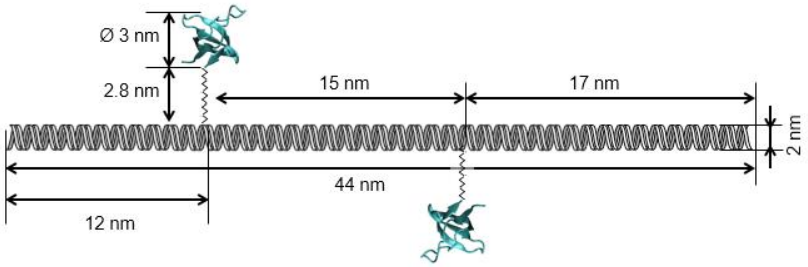

Figure 6.3. Schematic diagram showing the dimensions of synthetic DNA molecules with site-specific decoration of proteins. The width of the DNA backbone is approximately 2 nm and its length is 44 nm. The two site-specifically arraying proteins are designed to be located 15 nm apart from each other on the DNA backbone with a diameter of 3 nm.

The proposed structure of the site-specifically modified DNA is depicted In Figure 6.3. The 2 nm-wide, 44 nm-long DNA template serves as a backbone with two protein molecules with diameter 3 nm located at designate distances 2.8 nm on each side of the DNA. The separation between the proteins coupled by d5SICSCO – dNaM is approximately 15 nm. Finally, this double-labeled product is visualized by atomic force microscopy (AFM) to confirm that the resultant structure is consistent with our design.

6.2 AFM Characterization

To visualize the arrayed proteins, we employed atomic force microscopy (AFM). The double labeled product was first gel purified and then quantified by fluorescent dye binding. NiCl2 was added (10 mm final concentration) to a solution of this DNA (0.1 $ngmL^{-1}$), or to a control sample of unmodified DNA (1 $ngmL^{-1}$), and 10 mL was transferred onto freshly cleaved mica, incubated for 10 min, washed with 2 mL of NiCl2

solution (5 mm), and dried under a stream of compressed air.[82] AFM images were acquired in ambient air on a Veeco Nanoscope IV multimode AFM in tapping mode using silicon probes with force constant of 5 N/m and resonant frequency approximately 150 kHz (Ted Pella, Inc.).

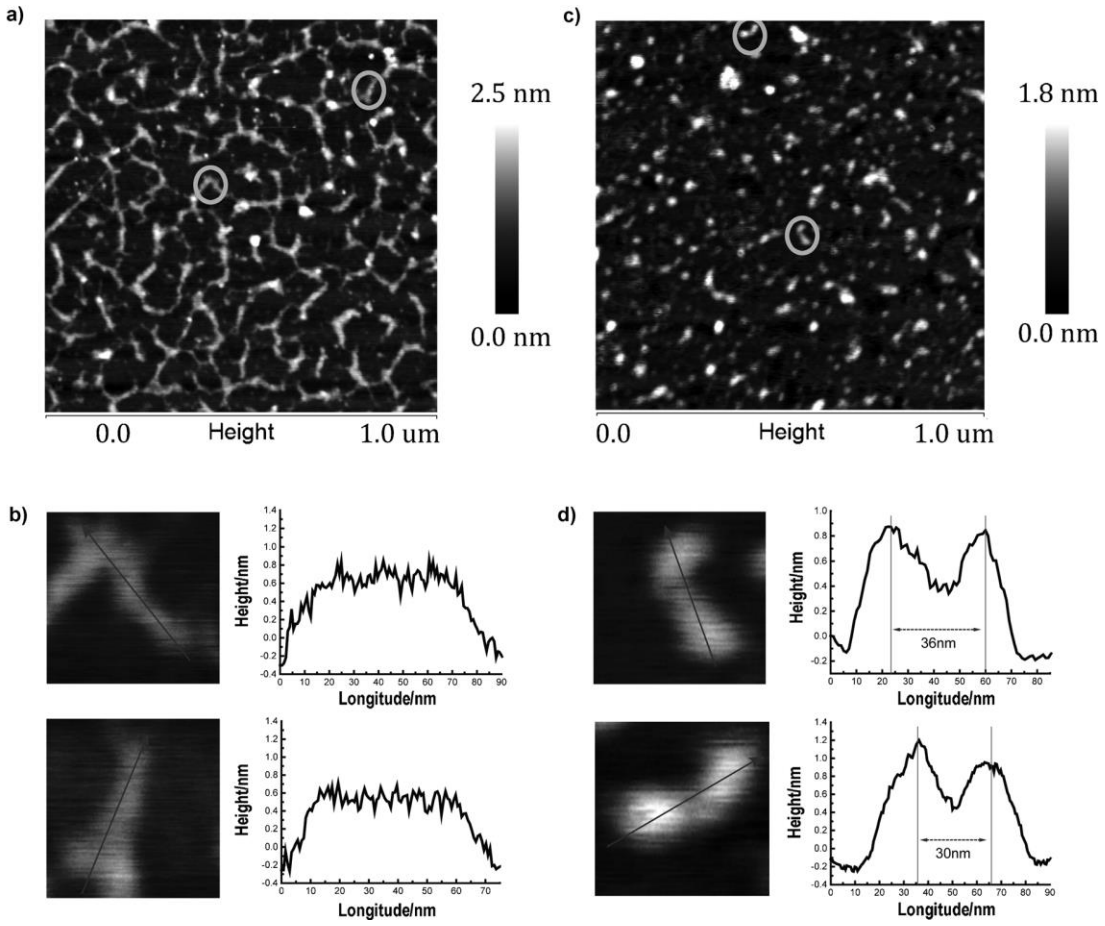

Figure 6.4: AFM images of: a), b) unmodified DNA, and c), d) double-nSH3 labeled DNA (tenfold lower concentration). The circled objects in panels A and C are magnified in panels B and D, respectively, and the corresponding height profiles are included.

AFM topographic images of DNA in the unlabeled sample (Figure 6.4 a and b) clearly show DNA spreading on the mica substrate, and the commonly observed end-

to-end contacts.[83] The average duplex length is 55 nm based on the full-width-half-maximum of the cross-section profiles, which is in good agreement with the expected length of 44 nm, and the average height is 0.51 nm, consistent with previous studies of duplex DNA.[84] Note that the apparent length and width of each DNA is convoluted by the imaging AFM tip radius of approximately 15 nm. Significantly, the nSH3 domains in the labeled sample were readily apparent and appeared as spherical objects with an average height of about 1 nm (Figure 6.4 c and d). Importantly, a significant number of the nSH3 domains appear as pairs separated by about 30 nm by a DNA linker of approximately 0.5 nm in height. Given the expected radius of nSH3, the distance between unnatural base pair sites of attachment, and the structure of the linkers, these observations confirm that the DNA is labeled with two nSH3 domains.

6.3 Correction to AFM-tip Induced Artifacts in the AFM Imaging of DNAs

Since the sizes of biological entities such as DNAs and proteins are usually comparable or even smaller than the radius of an AFM tip, the mechanical interaction between AFM tip and the sample often causes significant imaging artifacts such as topography convolution and tip indentation during the scanning process. The convolution generally leads to the broadening of width or diameters measured in AFM images, and the tip indentation into soft biological materials such as protein molecules usually results in inaccurate height measurement or modified surface profiles. Here we

discuss the artifacts observed in our AFM imaging for the site-specifically modified DNA and their correction to reflect the real dimensions of the sample.

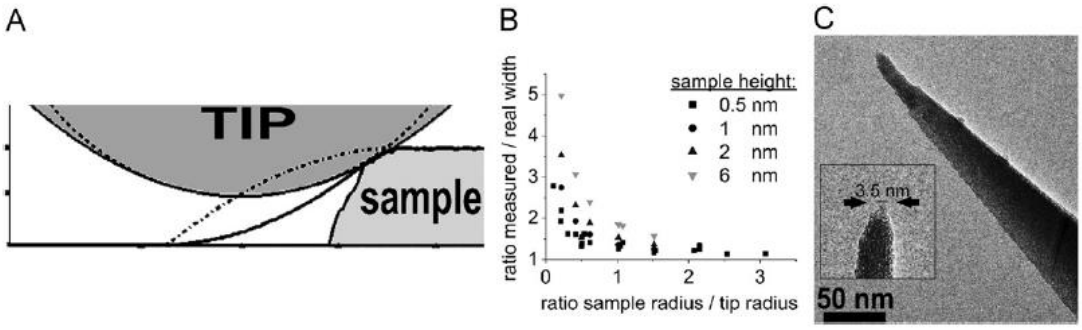

Figure 6.5: Modelling tip induced broadening in atomic force microscopy (AFM) images. (A) Tip induced broadening (black interrupted line) of real sample features (grey shaded area with black contour). (B) Increase in measured sample dimensions for different sample to tip size ratios. Simulations were carried out with Mathematica for a spherical tip shape with radii between 0.5 and 15 nm, particle diameters between 2 and 15 nm and particle heights between 0.5 and 6 nm. (C) Transmission electron micrograph (TEM) of an AFM tip. The zoom in the inset shows a tip apex with approximately 3.5 nm final diameter for this tip. The similar sizes for typical sample particles and tips place AFM experiments on protein–DNA systems in the range of ratios 0.5–2 in (B). [72]

A geometrical model for AFM tip induced topography convolution [72] is demonstrated in Figure 6.5a. By shaping the AFM tip with spherical profile, it is evident that as the tip moves over a sample with a comparable size, the sideway contour of the tip (instead of the center of the tip) will make contact with the sample first, and its height will rise before the tip center is directly above the actual sample edges. Because the AFM topography image is generated on the basis of tip position, this broadening will create an over-estimation by the AFM in the measurement of sample geometry, making the measured sample width/height larger than its real values. The simulations based on

this model and a TEM image for a typical AFM tip are also given in Figure 6.5(b,c). Therefore, in our experiment, although the expected duplex length of the DNA is 44 nm, the measured value exceeds that and reaches 55 nm. The real length can be roughly approximated by subtracting the known tip width (~15 nm) from the measured value (55 nm), which lands in the vicinity of 40 nm, which is very consistent with the theoretically predicted DNA length 44 nm. In addition, the average width of the DNA in Figure 6.5 is also much wider (16.5 nm) than the expected value (2 nm). However with the consideration in tip convolution, the corrected value (~1.5 nm) is a more realistic estimation.

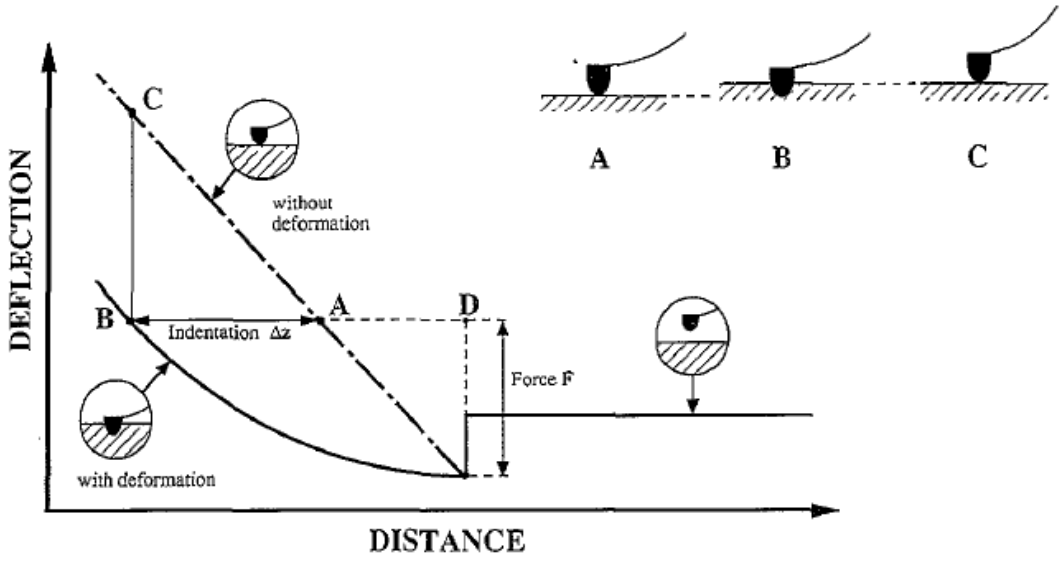

Figure 6.6: Diagram of sample deformation and height anomaly of soft surfaces studied with an AFM. [85]

Another common AFM-tip induced artifact is the indentation of rigid AFM tip into soft samples such as proteins or gel materials (Figure 6.6) [85]. The repulsive Van-der-Waals force from AFM tip at close distance may deform the sample surface and

modify its topography. Therefore, it crafts a “dent” in the surface and the observed sample height is normally lower than the actual value. This phenomenon is particularly serious in contact-mode AFM or tapping-mode AFM at small sample-tip working distance, and is also dependent on the scanning frequency (movement speed) of the tip. In other words, to reduce this artifact, aggressive scanning process should be avoided and a tapping-mode setup with larger working distance is favored.

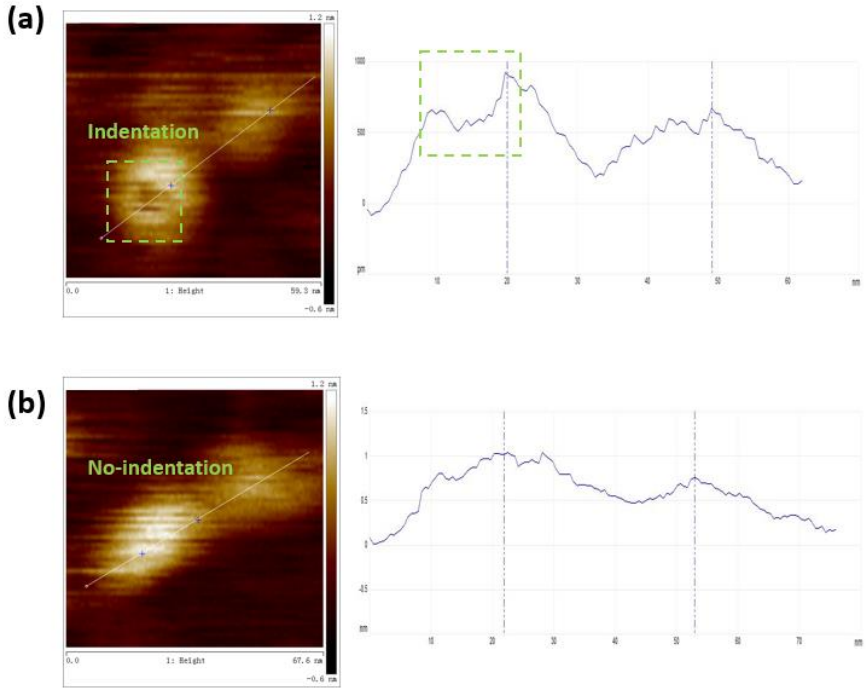

Figure 6.7: 2-D topography images and height profiles for the site-specifically modified DNA (a) with and (b) without AFM-tip induced indentation.

The tip indentation observed in our site-specifically modified DNA is shown in Figure 6.6a. Compared with a similar DNA sample without this effect (Figure 6.7b), we can see from both the 2-D topography image and the height profile that there is a “dent” (darker color in the AFM image) with lower height in the attached protein on the left.

This dent is most probably a defect caused by higher AFM-tip scanning speed and lower working distance during that AFM scan. By lowering the sweep frequency and adjust better feedback parameters, we corrected this artifact for all the other AFM experiments.

6.4 Conclusion

We have developed synthetic DNA molecules with site-specific decoration of proteins and visualized the product with atomic force microscopy (AFM). With proper corrections to AFM-tip induced artifacts such as topography convolution and surface indentation, we have measured and compared DNA molecules with and without the unnaturally placed pair of proteins. Their dimensions are consistent with our theoretically expected values, and these observations confirm that the DNA is successfully labeled with two designated molecules (nSH3 domains) at the defined locations.

6.5 Acknowledgement

Chapter 6, in part, is a reprint of Z. Li, T. Lavergne, D. A. Malyshev, J. Zimmermann, R. Adhikary, K. Dhami. P. Ordoukhanian, Z. Sun, J. Xiang, and F. E. Romesberg. “Site-Specifically Arraying Small Molecules or Proteins on DNA Using An Expanded Genetic Alphabet,” Chem. Eur. J. 2013, 19, 14205-14209.

Chapter 7:

Conclusion

Nanotechnology and nanofabrication has seen dramatic development in the past two decades. In particular, 3-D nanostructure fabrication has been intensively studied for the creation of novel devices, the scaling of existing systems, and the improvement in utilities and reliabilities. However, there are many new nanoscale phenomenon to be thoughtfully studied, such as the universal spontaneous attraction, in order to overcome the challenges in nano-device manufacturing and reliability.

First, we introduced the research on nanoscale spontaneous attraction, and proposed our simple capacitive force model to analyze this problem. Simulation results are given in chapter 2 which indicate that the attraction comes from the nanoscale capacitive electrostatic interaction caused by inevitable size variance among the nanostructures.

In chapter 3, the dependence on various physical parameters of the nanostructure, as well as the threshold conditions of attraction, is explored in a series of systematic experiments. With the decent consistency between abundant data and theoretical prediction, our model is experimentally verified. This result shall shine light on perspective nano-device design and fabrication. It also demonstrates that the precision and accuracy in nanofabrication can be the determining element to the success of scientific research or practical realization of functional devices or systems.

Next, we take advantage of the nanoscale electrostatic interaction and applied innovative grayscale electron beam lithography (gray-EBL) to fabricate low-voltage 3-terminal NEM switches. The detailed studies for controlling 3-D nanostructure geometries with gray-EBL is illustrated in chapter 4. A variety of suspending nanostructures with different shapes and accurately controlled air gaps are readily created with this fabrication method.

In chapter 5, we fabricate NEM-switches of both single cantilever type and doubly-clamped beam type with gray-EBL, and demonstrate that the single cantilever device has lower pull-in voltage as small as 1.6V at the cost of reliability, while the doubly-clamped structure provides better consistency for switching and improved resistance to stiction and gate leakage. An outlook for perspective NEMFET device created by gray-EBL is also discussed, with experimental data from the as-made prototypes of NEMFET with metal suspending gate and Ge/Si Core/Shell nanowire channel.

Finally, a practical application of nano-metrology in bio-medical engineering is illustrated in chapter 6. We apply ambient condition AFM to characterize the synthetic individual DNA molecules with site-specific decoration of proteins. The AFM-measured geometry for the artificially modified DNA matches well with our theoretically expected values, confirming that the DNA is successfully labeled with a pair of protein molecules (nSH3 domains) at the designated locations.

References

1. Loh, O. Y., Espinosa, H. D., Nanoelectromechanical contact switches. *Nature nanotechnology* 2012, 7, 283-95.

2. Lu, W., Lieber, C. M., Nanoelectronics from the bottom up. *Nat Mater* 2007, 6, 841-850.

3. Li, Y., Qian, F., Xiang, J., Lieber, C. M., Nanowire electronic and optoelectronic devices. *Materials Today* 2006, 9, 18-27.

4. Liu, J., Lee, S., Lee, K., Ahn, Y. H., Park, J. Y., Koh, K. H., Bending and bundling of metal-free vertically aligned ZnO nanowires due to electrostatic interaction. *Nanotechnology* 2008, 19, 185607.

5. Khorasaninejad, M., Abedzadeh, N., Singh Jawanda, A., O, N., Anantram, M. P., Singh Saini, S., Bunching characteristics of silicon nanowire arrays. *Journal of Applied Physics* 2012, 111, 044328.

6. Chen, B., Gao, Q., Chang, L., Wang, Y., Chen, Z., Liao, X., Tan, H. H., Zou, J., Ringer, S. P., Jagadish, C., Attraction of semiconductor nanowires: An in situ observation. *Acta Materialia* 2013, 61, 7166-7172.

7. Han, X., Wang, G., Zhou, L., Hou, J. G., Crystal orientation-ordered ZnO nanorod bundles on hexagonal heads of ZnO microcones: epitaxial growth and self-attraction. *Chemical communications* 2006, 212-4.

8. Wang, X., Summers, C. J., Wang, Z. L., Self-attraction among aligned Au/ZnO nanorods under electron beam. *Applied Physics Letters* 2005, 86, 013111.

9. De Volder, M. F. L., Vidaud, D. O., Meshot, E. R., Tawfick, S., John Hart, A., Self-similar organization of arrays of individual carbon nanotubes and carbon nanotube micropillars. *Microelectronic Engineering* 2010, 87, 1233-1238.

10. Li, G., Yilmaz, C., An, X., Somu, S., Kar, S., Joon Jung, Y., Busnaina, A., Wan, K.-T., Adhesion of graphene sheet on nano-patterned substrates with nano-pillar array. *Journal of Applied Physics* 2013, 113, 244303.

11. Ardito, R., Corigliano, A., Frangi, A., Modelling of spontaneous adhesion phenomena in micro-electro-mechanical systems. *European Journal of Mechanics - A/Solids* 2013, 39, 144-152.

12. Zaghloul, U., Bhushan, B., Pons, P., Papaioannou, G. J., Coccetti, F., Plana, R., Nanoscale characterization of different stiction mechanisms in electrostatically driven MEMS devices based on adhesion and friction measurements. *Journal of colloid and interface science* 2011, 358, 1-13.

13. Wagner, T. J., Vella, D., Switch on, switch off: stiction in nanoelectromechanical switches. *Nanotechnology* 2013, 24, 275501.

14. Zaghloul, U., Papaioannou, G., Bhushan, B., Coccetti, F., Pons, P., Plana, R., On the reliability of electrostatic NEMS/MEMS devices: Review of present knowledge on the dielectric charging and stiction failure mechanisms and novel characterization methodologies. *Microelectronics Reliability* 2011, 51, 1810-1818.

15. Lee, J. O., Song, Y. H., Kim, M. W., Kang, M. H., Oh, J. S., Yang, H. H., Yoon, J. B., A sub-1-volt nanoelectromechanical switching device. *Nature nanotechnology* 2013, 8, 36-40.

16. Patton, S. T., Zabinski, J. S., Failure Mechanisms of Capacitive MEMS RF Switch Contacts. *Tribology Letters* 2005, 19, 265-272.

17. Lu, X., Zheng, D., Zhai, T., Liu, Z., Huang, Y., Xie, S., Tong, Y., Facile synthesis of large-area manganese oxide nanorod arrays as a high-performance electrochemical supercapacitor. *Energy & Environmental Science* 2011, 4, 2915.

18. Chen, L. H. a. G., Analysis of Optical Absorption in Silicon Nanowire Arrays for Photovoltaic Applications. *Nano Lett* 2007, 7, 4.

19. Abadyan, M. R., Beni, Y. T., Noghrehabadi, A., Investigation of Elastic Boundary Condition on the Pull-in Instability of Beam-type NEMS under van der Waals Attraction. *Procedia Engineering* 2011, 10, 1724-1729.

20. Chen, C., Li, S., Dai, L., Qian, C., Buckling and stability analysis of a piezoelectric viscoelastic nanobeam subjected to van der Waals forces. *Communications in Nonlinear Science and Numerical Simulation* 2014, 19, 1626-1637.

21. Rodriguez, A. W., Capasso, F., Johnson, S. G., The Casimir effect in microstructured geometries. *Nature Photonics* 2011, 5, 211-221.

22. Agache, V., Quévy, E., Collard, D., Buchaillot, L., Stiction-controlled locking system for three-dimensional self-assembled microstructures: Theory and experimental validation. *Applied Physics Letters* 2001, 79, 3869.

23. Chandra, D., Yang, S., Capillary-force-induced clustering of micropillar arrays: is it caused by isolated capillary bridges or by the lateral capillary meniscus interaction force? *Langmuir : the ACS journal of surfaces and colloids* 2009, 25, 10430-4.

24. Duprat, C., Protiere, S., Beebe, A. Y., Stone, H. A., Wetting of flexible fibre arrays. *Nature* 2012, 482, 510-3.

25. Hill, J. J., Haller, K., Gelfand, B., Ziegler, K. J., Eliminating capillary coalescence of nanowire arrays with applied electric fields. *ACS applied materials & interfaces* 2010, 2, 1992-8.

26. Tang, Y., Zhao, D., Chen, J., Wanderka, N., Shen, D., Fang, F., Guo, Z., Zhang, J., Wang, X., Capillary-driven assembly of ZnO nanowire arrays into micropatterns. *Materials Chemistry and Physics* 2010, 121, 541-548.

27. Liu, J.-L., Xia, R., Zhou, Y.-T., Stiction of a Nano-Beam with Surface Effect. *Chinese Physics Letters* 2011, 28, 116201.

28. Boaz Pokroy, S. H. K., L. Mahadevan, Joanna Aizenberg, Self-Organization of a Mesoscale Bristle into Ordered, Hierarchical Helical Assemblies. *Science* 2009, 323, 4.

29. Sonin, L. M. B. a. A. A., Anisotropy and Effective Range of the van der Waals. *Langmuir : the ACS journal of surfaces and colloids* 1987, 3, 2.

30. Kong, X. Y., Ding, Y., Yang, R., Wang, Z. L., Single-crystal nanorings formed by epitaxial self-coiling of polar nanobelts. *Science* 2004, 303, 1348-51.

31. Albert K. Henninga, e., Two-dimensional surface dopant profiling In silicon using scanning Kelvin. *J. Appl. Phys.* 1995, 77, 9.

32. Breitenstein, O., Gupta, R., Schneider, J., Surface potential mapping on crystalline silicon on glass solar modules. *Journal of Applied Physics* 2007, 102, 024511.

33. Doukkali, A., Ledain, S., Guasch, C., Bonnet, J., Surface potential mapping of biased pn junction with kelvin probe force microscopy: application to cross-section devices. *Applied Surface Science* 2004, 235, 507-512.

34. Mizsei, J., Silicon surface passivation by static charge. *Applied Surface Science* 2006, 252, 7691-7699.

35. Lekner, J., Electrostatic force between two conducting spheres at constant potential difference. *Journal of Applied Physics* 2012, 111, 076102.

36. Jinhui Song, X. W., Elisa Riedo, and Zhong L. Wang, Elastic Property of Vertically Aligned Nanowires. *Nano Lett* 2005, 5.

37. Toshitake Takahashi, K. T., Ehsan Adabi, Zhiyong Fan, Ali M. Niknejad, and Ali Javey, Parallel Array InAs Nanowire Transistors for Mechanically Bendable, Ultrahigh Frequency Electronics. *ACS Nano* 2010 4 5855-5860.

38. Pacholski, C., Kornowski, A., Weller, H., Self-Assembly of ZnO: From Nanodots to Nanorods. *Angewandte Chemie International Edition* 2002, 41, 1188-1191.

39. Baughman, R. H., Zakhidov, A. A., de Heer, W. A., Carbon Nanotubes--the Route Toward Applications. *Science* 2002, 297, 787-792.

40. Li, J., Papadopoulos, C., Xu, J. M., Moskovits, M., Highly-ordered carbon nanotube arrays for electronics applications. *Applied Physics Letters* 1999, 75, 367-369.

41. Bunch, J. S., van der Zande, A. M., Verbridge, S. S., Frank, I. W., Tanenbaum, D. M., Parpia, J. M., Craighead, H. G., McEuen, P. L., Electromechanical Resonators from Graphene Sheets. *Science* 2007, 315, 490-493.

42. Surface and Interfacial Forces, Hans-Jurgen Butt, Michael Kappl, ISBN: 978-3-527-62942-8.

43. Capasso, F., Munday, J. N., Iannuzzi, D., Chan, H. B., Casimir Forces and Quantum Electrodynamical Torques: Physics and Nanomechanics. Selected Topics in Quantum Electronics, IEEE Journal of 2007, 13, 400-414.

44. A. P. Alivisatos, Semiconductor Clusters, Nanocrystals, and Quantum Dots. Science, New series, Vol. 271, No. 5251 (Feb. 16, 1996), 933-937

45. Datta, S. , Doczy, M. , Hareland, S. , Jin, B. , Kavalieros, J. , Linton, T. , Murthy, A. , Rios, R. , Chau, R. High performance fully-depleted tri-gate CMOS transistors, EDL, Vol 24 (4), 263-265

46. C. W. Schmidt, Nanotechnology-Related Environment, Health, and Safety Research: Examining the National Strategy. Environ Health Perspect. 2009 Apr, 117(4): A158–A161.

47. E. Rabani, D. R. Reichman, P. L. Geissler and L. E. Brus, Drying-mediated self-assembly of nanoparticles. Nature 426, 271-274.

48. X. Zhou, Y. Yi, L. Wan, Y. Guo. Self-Assembled Nanocomposite of Silicon Nanoparticles Encapsulated in Graphene through Electrostatic Attraction for Lithium-Ion Batteries. Advanced Energy Materials, Volume 2, Issue 9, Pages 1086–1090

49. W. Jang, J Lee, Jo Yoon, M Kim, J Lee,S Kim, K Cho, D Kim, DPark, and W Lee, Fabrication and characterization of a nanoelectromechanical switch with 15-nm-thick suspension air gap. APPLIED PHYSICS LETTERS 92, 103110 (2008)

50. S. Hudlet, M. Saint Jeana, C. Guthmann, and J. Berger, Evaluation of the capacitive force between an atomic force microscopy tip and a metallic surface, Eur. Phys. J. B 2, 5{10 (1998)}.

51. G, Zheng, F, Patolsky, Y, Cui, W. U Wang, and C. M Lieber, Multiplexed electrical detection of cancer markers with nanowire sensor arrays. Nature Biotechnology 23, 1294 - 1301 (2005)

52. K. Sun, N. Park, Z. Sun, J. Zhou, J. Wang, X. Pang, S. Shen, S.Y. Noh, Y. Jing, S. Jin,P. K. L. Yua and D. Wang. Nickel oxide functionalized silicon for efficient photo-oxidation of water. Energy Environ. Sci., 2012, 5, 7872

53. M Li, R B. Bhiladvala1, T J. Morrow, J A. Sioss, K-K Lew, J M. Redwing, C D. Keating and T S. Mayer, Bottom-up assembly of large-area nanowire resonator arrays. Nature Nanotechnology 3, 88 - 92 (2008)

54. A Fruehling, S Xiao, M Qi, K Roy, and D Peroulis, Nano-switch for Study of Gold Contact Behavior. Sensors, 2009 IEEE conference, 248 - 251

55. R Murali, D K. Brown, K P. Martin, and J D. Meindl, Process optimization and proximity effect correction for gray scale e-beam lithography. Journal of Vacuum Science & Technology B 24, 2936 (2006)

56. X.Q. Sun, T. Masuzawa, M. Fujino, Ultrasound micro-machining and its application to MEMS Sensor. Actuat. A: Phys. 57 (2) (1996) 159 – 164.

57. M. Mullenborn, H. Dirac, J.W. Peterson, S. Bouwstra. Fast three-dimentional laser micromachining of silicon for microsystems. Sensor. Actuat. A: Phys. 52 (1 – 3) (1996) 121 – 125.

58. J. Kim, D.C. Joy, S.-Y. Lee, Controlling resist thickness and etch depth for fabrication of 3D structures in electron-beam grayscale lithography. Microelectronic Engineering 84 (2007) 2859 – 2864.

59. M. Ekberg, F. Nikolajeff, M. Larsson, and S. Hard. Proximity-compensated blazed transmission grating manufacture with direct-writing, electron-beam lithography. Applied Optics, 1 January 1994 , Vol. 33, No. 1, 103-107

60. Y. Ishii, J. Taniguchi. Fabrication of three-dimensional nanoimprint mold using inorganic resist in low accelerating voltage electron beam lithography. Microelectronic Engineering 84 (2007) 912 – 915

61. Zhou, Y., Thekkel, S. & Bhunia, S. Low power FPGA design using hybrid CMOS-NEMS approach in Proc. 2007 ACM/IEEE Int. Symp. on Low Power Electron. Des. 14–19 (IEEE, 2007).

62. Dadgour, H. F. & Banerjee, K. Hybrid NEMS–CMOS integrated circuits: A novel strategy for energy-efficient designs. Comp. Digital Techn. 3, 593–608 (2009).

63. N. Abele, R. Fritschi, K. Boucart, F. Casset . in IEEE Int. Elec. Dev. Meeting 2005; http://dx.doi.org/10.1109/IEDM.2005.1609384

64. Lee, T-H., Bhunia, S. & Mehregany, M. Electromechanical computing at 500 ° C with silicon carbide. Science 329, 1316–1318 (2010).

65. Lovellette, M. N., A. B. Campbell, H. L. Hughes, R. K. Lawerence, J. W. Ward, M. Meinhold, T. R. Bengtson, G. F. Carleton, B. M. Segal, and T. Rueckes, "Nanotube memories for space applications", Aerospace Conference, 2004. Proceedings. 2004 IEEE, vol. 4, pp. 2300 - 2305 Vol.4, mar., 2004.

66. Jonsson, L., Axelsson, S., Nord, T., Viefers, S. & Kinaret, J. High frequency properties of a CNT-based nanorelay. Nanotechnology 15, 1497–1502 (2004).

67. J. E. Jang, S. N. Cha, Y. Choi, Gehan A. J. Amaratunga, D. J. Kang, D. G. Hasko, J. E. Jung and J. M. Kim . "Nanoelectromechanical switches with vertically aligned carbon nanotubes," Applied Physics Letters, vol. 87, pp. 163114-3, 2005.

68. Weon Wi Janga , Jun-Bo Yoona, Min-Sang Kimb, Ji-Myoung Lee, Sung-Min Kim, Eun-Jung Yoon, Keun Hwi Cho, Sung-Young Lee, In-Hyuk Choi, Dong-Won Kim, Donggun Park. NEMS switch with 30 nm-thick beam and 20 nm-thick air-gap for high density non-volatile memory applications. Solid-State Electronics 52 (2008) 1578 – 1583

69. A. M. Ionescu, V. Pott, R. Fritschi, K. Banerjee, M. J. Declercq, P. Renaud, C. Hibert, P. Fluckiger, G. A. Racine. "Modeling and design of a low-voltage SOI suspended-gate MOSFET (SG-MOSFET) with a metal-over-gate architecture," in Quality Electronic Design, 2002. Proceedings. International Symposium on, 2002, pp. 496-501.

70. J. I. Seeger and S. B. Crary, "Stabilization of electrostatically actuated mechanical devices," in Solid State Sensors and Actuators, 1997. TRANSDUCERS '97 Chicago., 1997 International Conference on, 1997, pp. 1133-1136 vol.2.

71. J. H. Kim, Z. C.Y. Chen,S. Kwon, and J. Xiang. Three-Terminal Nanoelectromechanical Field Effect Transistor with Abrupt Subthreshold Slope. Nano Lett. 2014, 14, 1687−1691.

72. A.T. Winzer, C.Kraft, S.Bhushan, V.Stepanenko, I.Tessmer, Correcting for AFM tip induced topography convolutions in protein–DNA samples. Ultramicroscopy 121 (2012) 8–15.

73. a) M. Hollenstein, C. J. Hipolito, C. H. Lam, D. M. Perrin, Nuclei Acids Res. 2009, 37, 1638 – 1649; b) A. D. Keefe, S. T. Cload, Curr. Opin. Chem. Biol. 2008, 12, 448 – 456.

74. a) N. C. Seeman, Annu. Rev. Biochem. 2010, 79, 65 – 87; b) H. Wang, R. Yang, L. Yang, W. Tan, ACS Nano 2009, 3, 2451 – 2460; c) T. Chen, M. I. Shukoor, Y. Chen, Q. Yuan, Z. Zhu, Z. Zhao, B. Gulbakan, W. Tan, Nanoscale 2011, 3, 546 – 556.

75. a) D. A. Malyshev, K. Dhami, H. T. Quach, T. Lavergne, P. Ordoukhanian, A. Torkamani, F. E. Romesberg, Proc. Natl. Acad. Sci. USA 2012, 109, 12005 – 12010; b) T. Lavergne, D. A. Malyshev, F. E. Romesberg, Chem. Eur. J. 2012, 18, 1231 – 1239; c) Z. Yang, F. Chen, J. B. Alvarado, S. A. Benner, J. Am. Chem. Soc. 2011, 133, 15105 – 15112; d) C. Kaul, M. Muller, M. Wagner, S. Schneider, T. Carell, Nat. Chem. 2011, 3, 794 – 800; e) M. Kimoto, R. Kawai, T. Mitsui, S. Yokoyama, I. Hirao, Nucleic Acids Res. 2009, 37, e14;f) D. A. Malyshev, Y. J. Seo, P. Ordoukhanian, F. E. Romesberg, J. Am. Chem. Soc. 2009, 131, 14260 – 14621; g) A. M. Leconte, G. T. Hwang, S. Matsuda, P. Capek, Y. Hari, F. E. Romesberg, J. Am. Chem. Soc. 2008, 130, 2336 – 2343;

76. a) Y. J. Seo, D. A. Malyshev, T. Lavergne, P. Ordoukhanian, F. E. Romesberg, J. Am. Chem. Soc. 2011, 133, 19878 – 19888; b) R. Yamashige, M. Kimoto, Y. Takezawa, A. Sato, T. Mitsui, S. Yokoyama, I. Hirao, Nucleic Acids Res. 2012, 40, 2793 – 2806; c) T. Ishizuka, M. Kimoto, A. Sato, I. Hirao, Chem. Commun. 2012, 48, 10835 – 10837

77. a) V. Hong, S. I. Presolski, C. Ma, M. G. Finn, Angew. Chem. 2009, 121, 10063 – 10067; Angew. Chem. Int. Ed. 2009, 48, 9879 – 9883; b) J. Gierlich, G. A. Burley, P. M. Gramlich, D. M. Hammond, T. Carell, Org. Lett. 2006, 8, 3639 – 3642

78. D. A. Malyshev, D. A. Pfaff, S. I. Ippoliti, G. T. Hwang, T. J. Dwyer, F. E. Romesberg, Chem. Eur. J. 2010, 16, 12650 – 12659

79. Y. J. Seo, S. Matsuda, F. E. Romesberg, J. Am. Chem. Soc. 2009, 131, 5046 – 5047.

80. a) T. Gourlain, A. Sidorov, N. Mignet, S. J. Thorpe, S. E. Lee, J. A. Grasby, D. M. Williams, Nucleic Acids Res. 2001, 29, 1898 – 1905; b) M. Kuwahara, J. Nagashima, M. Hasegawa, T. Tamura, R. Kitagata, K. Hanawa, S. Hososhima, T. Kasamatsu, H. Ozaki, H. Sawai, Nucleic Acids Res. 2006, 34, 5383 – 5394; c) H. A. Held, S. A. Benner, Nucleic Acids Res. 2002, 30, 3857 – 3869; d) S. E. Lee, A. Sidorov, T. Gourlain, N. Mignet, S. J. Thorpe, J. A. Brazier, M. J. Dickman, D. P. Hornby, J. A. Grasby, D. M. Williams, Nucleic Acids Res. 2001, 29, 1565 – 1573; e) K. Sakthivel, C. F. Barbas III, Angew. Chem. 1998, 110, 2998 – 3002; Angew. Chem. Int. Ed. 1998, 37, 2872 – 2875.

81. T. Lavergne, M. Degardin, D. A. Malyshev, H. T. Quach, K. Dhami, P. Ordoukhanian, F. E. Romesberg, J. Am. Chem. Soc. 2013, 135, 5408 – 5419.

82. Y. L. Lyubchenko, L. S. Shlyakhtenko, T. Ando, Methods 2011, 54, 274 – 283.

83. C. Maffeo, B. Luan, A. Aksimentiev, Nucleic Acids Res. 2012, 40, 3812 – 3821

84. A. Schaper, L. I. Pietrasanta, T. M. Jovin, Nucleic Acids Res. 1993, 21, 6004 – 6009.

85. A. L Weisenhornt, M. Khorsandit, S. Kasast, V. Gotzost and H-J Butt, Deformation and height anomaly of soft surfaces studied with an AFM, Nanotechnology 4 (1993) 106113.